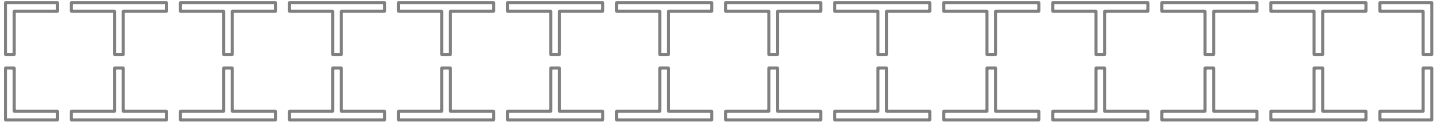
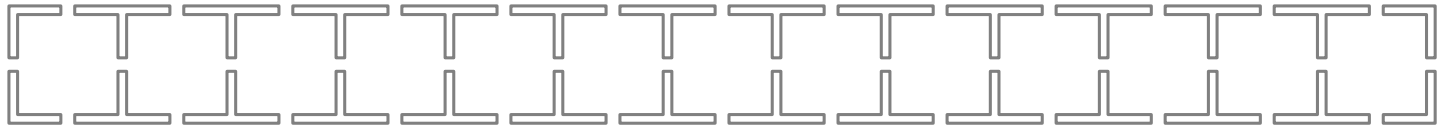


TECHNICAL UNIVERSITY OF DENMARK
PHD THESIS



STRONG INTERACTION BETWEEN THE LIGHT FIELD AND AN
ULTRA-COHERENT MECHANICAL OSCILLATOR



By
Daniel Allepuz Requena

Supervised by
Professor Ulrik Lund Andersen
Associate Professor Alexander Huck
Dr. Ulrich Busk Hoff

August 2024

A thesis submitted in partial fulfilment of the requirements for the degree of
Doctor of Philosophy at the Technical University of Denmark.

Author:

Daniel Allepuz Requena

Supervisors:

Professor Ulrik Lund Andersen
Associate Professor Alexander Huck
Dr. Ulrich Busk Hoff

Period:

September 2021 – August 2024

Work done in the Center for Macroscopic Quantum States (bigQ) in the
Department of Physics of the Technical University of Denmark.

Version 9

Updates and errata are available at: www.dallepuz.xyz/thesis

ABSTRACT

The search for quantum phenomena in macroscopic objects has accelerated in the past decade. Precise experiments that strongly measure large objects can shed light into the measurement problem and help study the dynamics of open quantum systems. Engineered ultra-coherent mechanical resonators with low-masses but micrometer dimensions are at the forefront of this endeavor. Due to the plethora of systems that can couple to mechanical motion, low dissipation resonators can also be used as transducers of quantum information or as long-lived quantum memories.

The advances in ultra-low dissipation rate mechanical resonators have allowed the observation of true quantum effects at room-temperature. Experiments that were previously only possible at cryogenic temperatures have started to translate to room temperature. Light, with its persistent quantum nature, is the tool that allows measurement and control at the needed precision.

In this work, we have designed and implemented a $126\mu\text{m}$ -long optical micro-cavity to enhance the interaction of light with a mechanical resonator placed in its center. We have fabricated mirrors that are shielded from vibrations. Using phononic crystal patterns, we have suppressed the motion of the mirrors' surface in a frequency span between 1MHz and 1.5MHz. The motion of the mirror at these frequencies is measured to be at least three orders of magnitude smaller than outside the region. The cavity is specifically designed to house our mechanical resonator, a silicon-nitride membrane. Our system is passively aligned and it allows the cavity to exceed 60000 finesse when loaded with the membrane, all while keeping the resonator's quality factor intact, which is close to 10^8 .

Our room-temperature system is capable of reaching quantum cooperativities around 0.32, where values above 1 indicate that the system is dominated by quantum fluctuations. In theory, this interaction strength cools our oscillator to an occupation of 32 phonons, equivalent to a temperature of 1.4mK.

We identify laser phase noise as the limiting factor of our setup. Without it, we predict that our platform will be able to prepare the resonator in its ground state through feedback cooling. Furthermore, we expect a reduction of the fluctuations of light below vacuum fluctuations through optomechanical squeezing.

DANSK RESUMÉ

Søgningen efter kvantefænomener i makroskopiske objekter er accelereret i det seneste årti. Præcise eksperimenter, der kraftigt måler store objekter, kan kaste lys over måleproblemet og hjælpe med at studere dynamikken i åbne kvantesystemer. Konstruerede ultrakohærente mekaniske resonatorer med lav masse, men mikrometer-dimensioner, står i spidsen for denne bestræbelse. På grund af de mange systemer, der kan kobles til mekanisk bevægelse, kan resonatorer med lav dissipation bruges som transducere af kvanteinformation eller som langtidsholdbare kvantehukommelser.

Fremskridtene inden for mekaniske resonatorer med ultra-lav dissipation har gjort det muligt at observere ægte kvanteeffekter ved stuetemperatur. I det seneste år er forberedelsen af kvantetilstande ved kryogene temperaturer overgået til eksperimenter ved stuetemperatur. Lys er med sin kvantekarakter det værktøj, der gør det muligt at måle og kontrollere med den nødvendige præcision.

I dette arbejde har vi designet og implementeret en optisk mikrokavitet for at forbedre lysets interaktion med en mekanisk resonator placeret i midten af den. Vi har fremstillet spejle, der er afskærmet fra vibrationer. Ved hjælp af fononiske krystalmønstre har vi undertrykt bevægelsen af spejlenes overflade i et frekvensområde mellem 1 MHz og 1.5 MHz. Spejlets bevægelse ved disse frekvenser er målt til at være mindst tre størrelsesordener mindre end uden for området. Kaviteten er specielt designet til at rumme vores mekaniske resonator, en membran af siliciumnitrid. Vores system er passivt flugtet, hvilket gør det muligt for systemet at overskride 60000 finesser, når det belastes med membranen, samtidig med at resonatorens kvalitetsfaktor tæt på 10^8 er intakt.

Vores system ved stuetemperatur er i stand til at nå kvantekooperativiteter omkring 0.32, hvor værdier over 1 indikerer, at systemet er domineret af kvantefluktuationer. I teorien kan denne interaktionsstyrke nedkøle vores oscillator til 32 fononer, hvilket svarer til en temperatur på 1.4 mK.

Uden laserfasestøj forudsiger vi, at vores platform vil være i stand til at forberede resonatoren i dens grundtilstand gennem feedback-køling, samt reducere lysfluktuationerne under vakuumfluktuationer gennem optomekanisk klemning.

ACKNOWLEDGEMENTS

I want to thank my main supervisors Ulrik and Alex for giving me the opportunity to do my PhD in their group. I immensely appreciate the trust you have put in me during these years. Thanks Alex for always having your door open. I'm also grateful to the other professors in our group, Jonas, Jonatan and Tobias who have helped me along the way; Adaleta and Mia who keep our group and department working, as well as Søren and the rest of handy people in the mechanical workshop.

I'm thankful for the rest of the optomech crowd. Thanks Luiz for your optimism and help, I'm happy for the times we got to work together. To my clean-room dwelling office buddies Dennis and Yincheng, thank you for answering my dumb Comsol questions and listening to my crazy fabrication ideas. Thanks Frederik, always quick on his feet with a calculation, and Yingxuan, always ready to help. Thanks Zohran for putting in the effort during my last mile.

I've had the pleasure of working three years with wonderful people in our group. Thanks to everyone that makes the group a better place by organizing activities or using their time to teach us new things. I've enjoyed the camaraderie with my fellow PhD students, thanks Abhi, Benjamin, Huy and Tummas for listening to me complain and making me laugh. Thanks Jens for being my guide to the ancient lore stored in the group's drive. Thanks neighbors in the theory office, specially Anders, for taking the time to listen. *Gracias* Santiago and thanks Dhiren for sharing your experience. Thanks Maxime for welcoming me to the group and Angelo for getting me a laser.

I also want to thank Professor Dalziel Wilson at the University of Arizona and all the members of his group for welcoming me during my stay there in April 2023. Everyone went out of their way to make me feel part of the group, even when I was back in the US for a conference.

Finally, I would not be writing this thesis if it wasn't for Carolina, my partner in crime. It is your love and relentless support that has carried me to this point. Thanks for always trying to make me see the vacuum chamber half empty.

Gràcies Guillem per ser el meu company d'experiments des de que estàvem al garatge de casa. Gràcies papa i mama per creure que ho podia fer.

Contents

1	Introduction	9
1.1	Structure of the thesis	11
2	The theory of optomechanical interaction	13
2.1	Introduction	13
2.2	The harmonic oscillator	14
2.2.1	The open harmonic oscillator	15
2.2.2	Quantum dynamics of the open harmonic oscillator	16
2.2.3	Cavity-free optomechanical interaction	18
2.3	Optical cavities	18
2.3.1	The resonant modes and spectrum of an optical cavity	19
2.3.2	Quantum dynamics of optical cavities	22
2.4	The dispersive optomechanical hamiltonian	26
2.5	Membrane-in-the-middle cavity optomechanics	27
2.6	The linearized cavity quantum optomechanics equations	30
2.6.1	The steady state	32
2.6.2	The fluctuation dynamics	34
2.6.3	Dynamical backaction	35
2.6.4	Optical fluctuations	36
2.6.5	Optomechanical squeezing	39
2.7	Detection schemes	40
2.7.1	Direct detection	42
2.7.2	Balanced Homodyne Detection	42
3	A low-noise micro-cavity for quantum optomechanics	49
3.1	Introduction	49
3.1.1	The length of the cavity	50
3.1.2	The mirror reflectivity	50
3.1.3	Tunability	51
3.2	Overall description of the experiment	53
3.2.1	Assembly procedure	54
3.3	The mechanical resonator: Density modulated phononic membranes	56
3.4	Tuning the optomechanical coupling	58
3.5	Low-noise mirrors	59
3.5.1	Thermomechanical motion of regular mirrors	59
3.5.2	Design of patterned mirror substrates	61
3.5.3	Cavity noise reduction	61

3.6	The optical set-up	63
3.6.1	Aligning to the microcavity	66
3.6.2	Alignment to the bottom mirror for transmission measurements	68
4	Micromirror fabrication through laser ablation	69
4.1	Setup	69
4.1.1	Laser ablation subsystem	71
4.1.2	Characterization subsystem	72
4.1.3	Fabrication procedure	73
4.2	Fabrication results	74
4.2.1	Repeatability and yield	75
4.2.2	Range of geometries	75
5	Characterization of the cavity optomechanics experiment	79
5.1	Optical characteristics	79
5.1.1	Free spectral range, length and mirror curvature	79
5.1.2	Optical linewidth and birefringence	80
5.2	Mechanical quality factor	82
5.3	Strength of the optomechanical interaction	84
5.3.1	Measurement of cooperativity through the optical spring effect	86
5.4	Laser noise	88
5.4.1	Laser amplitude noise	88
5.4.2	Laser phase noise	89
6	Experimental challenges in the high-cooperativity regime	93
6.1	Membrane rupture	93
6.2	Laser locking at high intracavity-power	94
6.3	Phase noise in optomechanical experiments	96
6.3.1	Heating by phase noise	96
6.3.2	Phase noise in detection	97
6.4	Thermal intermodulation noise	100
7	Conclusions and outlook	103
7.1	Next steps	103
A	The Markovian quantum Langevin equation	107
B	Separation of fields into average and fluctuation terms	109
C	Power Spectral Density	111
C.1	Definition and conventions	111
C.2	Useful results	112
D	Single Detector Homodyne	113
E	The vacuum set-up	117
E.1	Overall description and operation	117
E.2	The cavity holder	119
F	Modulation depth calibration	121

Chapter 1

Introduction

Quantum mechanics is *not* a theory of small things. Although the theory of quantum mechanics is usually introduced as our best model for atoms, sub-atomic particles and light, none of its principles talks about the extent or mass of the system. Quantum mechanics is a theory about experiment outcomes, at least through the lens of the Copenhagen interpretation. It tells us which measurements are possible and which are not, what are the possible outcomes of those measurements, what probability we should assign to each outcome and how these probabilities evolve over time. It does *not* tell us which experiments are governed by quantum mechanics and which are not.

As good scientists, we should push a theory to its limits. Indeed, we struggle to make quantum mechanics compatible with the high energy regime, when relativistic effects manifest. Great feats have been accomplished along this research line, some of them are the merging of quantum mechanics and special relativity [1], postulating the existence of quarks and the strong force [2] and the unification of the weak interaction with electromagnetism [3, 4]. These and other theoretical developments, forming the Standard Model, have been vindicated in large scale experiments such as the Large Hadron Collider [5]. However, there are much simpler experiments that can push quantum theory.

The majority of experiments that we hold as evidence for the laws of quantum mechanics, such as the Stern-Gerlach experiment [6, 7], measure observables of single atoms or sub-atomic particles. With the exception, of course, of key quantum optics experiments, such as tests of the Bell inequality [8], which deal with more “classical” degrees of freedom such as polarization [9]. But how far can we push the idea of quantum mechanics describing every experiment? Will the small angle of a pendulum be subject to quantum laws? What about the amplitude of the collective motion of a tuning fork? In principle, these observables can be treated quantum mechanically in the same manner as more traditionally “quantum” degrees of freedom, such as spin.

Experiments point to a resounding *yes*. With enough precision, we ultimately need quantum mechanics to model our observations, regardless of the system’s mass or size. The quantization of mechanical motion was first observed in a micro drum at a temperature of 25mK [10]. What makes this observation extraordinary is the necessity to apply quantum theory to a single degree of freedom that corresponds to the motion of thousands of atoms, even more strangely, the same atoms participate in motion of other mechanical modes that do not manifest quantum behavior. This experiment necessitated a qubit, which in turn requires superconductivity. Nevertheless, similar results followed using optical-mechanical resonators, this time at much

higher temperatures of 20K [11].

Observing such effects at room temperature is a bigger challenge. Due their low frequency and consequent high thermal occupation, mechanical resonators are constantly moved by random thermal forces. However, two systems at the same frequency and temperature can have thermal forces of vastly different magnitude. This is due to thermal forces being proportional to the resonator's damping rate [12]. The fact that reducing the damping rate has a similar effect to lowering the temperatures has launched a race to find resonators with ultra-low dissipation. Two platforms show the most promise, optically-levitated nano-particles and engineered membrane resonators. For example, a levitated nano-particle has been laser cooled to its ground state starting from room-temperature [13], enabled in part by the high isolation from the thermal bath in ultra high vacuum and by the low mass of the particle. In contrast, membranes are larger, with areas as big as hundreds of micrometers and thicknesses of nanometers. More than a decade of developments [14–17] have culminated in ultra-coherent membrane resonators with thermal dissipation rates significantly below their oscillation frequencies [18–21]. In other words, we can study resonators than can undergo multiple oscillations without absorbing a single phonon from their environment.

Light is the only tool available to measure the motion of mechanical resonators at room temperature. Any sort of electric coupling, such as the capacitive coupling in superconductive circuits, will require cryogenic temperatures in order to remove thermal noise. In contrast, coherent light, emitted from a laser for example, does not carry thermal fluctuations at room-temperature thanks to its high frequency. It is an *almost* noiseless probe that we can use to interact with and measure our mechanical resonators. Interferometers, the devices that exploit the wave-like nature of light to measure distances, have a stellar experimental record, from Michelson and Morley disproving the existence of the luminiferous ether [22] to the first detection of gravitational waves by LIGO [23]. As all quantum measurements, measuring with light is not free of consequence. Light contains fundamental quantum fluctuations, the shot noise, which not only limit the signal-to-noise ratio of our measurement, but also couple to the object that we are measuring through radiation pressure. The best measurement that we can do will strike a balance between signal-to-noise ratio and back action on the object, in this situation, we say that the measurement is at the Standard Quantum Limit [24].

Optical cavities, which recycle light in-between two highly reflective mirrors, are also interferometers. They are extremely sensitive to changes of the effective distance between their mirrors¹. Cavities are not only measurement instruments, a cavity with a mechanically compliant mirror (or with a thin, partially reflective membrane inside) exhibits a plethora of interesting phenomena. Some examples are: laser cooling of the mechanical motion, mechanical frequency shifts through the optical potential and reduction of the light's quantum fluctuations (squeezing) [25]. The field of *cavity optomechanics* has flourished in the past decade, examples of its achievements are: ground-state cooling of a 1MHz resonator from 10K [26], the very recent optomechanical squeezing at room temperature [27] and even more recent measurement of mechanical asymmetry (a tell-tale of quantum behavior) at room temperature [28].

The main focus of this work has been to design a state of the art cavity optomechanical system that addresses the main technical problems that impede reaching the quantum regime at room-temperature. Motivated by our group's development of ultra coherent membrane resonators [20], we have fabricated a low-noise micro-cavity that tightly integrates the membrane substrate in its design. This is possible thanks to a reliable and tunable micromirror template fabrication process.

¹LIGO is in fact an interferometer where each arm is an optical cavity.

1.1 Structure of the thesis

Following is a list describing how the chapters of this thesis are organized.

- In Chapter 2, the theory of cavity optomechanics is introduced. We start by describing the open quantum harmonic oscillator using the Langevin equation. We use the same formalism to describe the optical cavity. We derive the source of optomechanical interaction in a cavity, in particular, the configuration of a semi-reflective membrane placed in-between its mirrors. We then proceed with a dynamical model of the joint mechanical and optical mode. Finalizing with the derivation of models for different detection schemes while including classical phase noise.
- In Chapter 3, we describe the experiment that we have designed. We motivate the decisions made and go into great detail about the geometry of the cavity, as well as how it is actually implemented on the optical table. We also demonstrate the performance of our low-noise mirrors. Details about the vacuum set-up for Appendix E.
- In Chapter 4 we describe the fabrication of concave micromirror templates through feedback controlled laser ablation.
- In Chapter 5, we measure the relevant figures of merit for optomechanical interaction. We detail the issues we encountered when characterizing an optomechanical system with large interaction. We also include a characterization of our lasers phase noise, and shown that it is quantum limited in amplitude.
- In Chapter 6, we illustrate some of the challenges present in our set-up that prevents us from reaching the quantum dominated regime. This includes problems of a technical nature, such as the membrane rupturing, or laser phase noise, as well as thermal intermodulation noise, an effect not considered in our linear theory developed in Chapter 2.
- In Chapter 7, we summarize our findings and discuss the next steps of our experiment.

Chapter 2

The theory of optomechanical interaction

2.1 Introduction

Optomechanics is the study of systems where light and compliant mechanical objects interact. Optomechanical interaction is a consequence of Maxwell's equations, appearing in the form of *radiation pressure*. Electromagnetic waves carry momentum and exert forces at interfaces between media, as well as while propagating in them¹. Note that this interaction does not arise from the quantization of the electromagnetic field. Nevertheless, the classical prediction of radiation pressure is identical to the quantum picture of single photons carrying momentum equal to $\frac{h\nu}{c}$.

We aim to use optomechanical interaction to reveal the quantum nature of mechanical motion, either by observation of quantized degrees of freedom, or by interacting with light with quantum coherence. Optomechanics is well suited for this task because light easily exhibits quantum behavior, even at room-temperature. Due to its high frequency, its thermal occupation is virtually zero. We can consider light to be "cold": all its observed randomness is due to quantum fluctuations. The same cannot be said for macroscopic objects oscillating at frequencies around a megahertz.

In this chapter, we first summarize the quantum model of the mechanical harmonic oscillator. It will become apparent that the quantum effects of optomechanical interaction are weak compared to classical thermal effects. We will then summarize the theory of optical cavities, they allow us to strengthen the interaction through the build-up of power and repeated reflections. Finally, I will introduce a fully quantum model of cavity optomechanical interaction, including key non-idealities present in room-temperature experiments.

¹Surprisingly, there is still some controversy in the nature of radiation pressure inside a medium, see the work by [29] and [30]

²The force in Newton exerted by light on a perfectly reflecting object from a Maxwell's perspective is $F = \frac{2 \cdot (\text{Power})}{c}$. From a semi-classical perspective: $F = 2 \cdot (\text{Photon rate}) \cdot \frac{h\nu}{c}$, once we make the connection that $(\text{Photon rate}) = \frac{(\text{Power})}{h\nu}$, both expressions are identical.

2.2 The harmonic oscillator

A harmonic oscillator is a physical system equivalent to a particle with mass m subject to a potential quadratic in position:

$$V(q) = \frac{1}{2}kq^2, \quad (2.1)$$

with q being the position of the particle and k being the spring constant, which is the proportionality constant between displacement from equilibrium and restoring force. The dynamics of the harmonic oscillator are determined by its total energy:

$$H = \frac{1}{2m}p^2 + \frac{1}{2}kq^2, \quad (2.2)$$

where $p = m\dot{q}$ is the momentum of the particle. Solving the system using Hamilton's equations, it is found to oscillate at a characteristic angular frequency:

$$\Omega_m = \sqrt{\frac{k}{m}}. \quad (2.3)$$

The standard first quantization procedure can be used to obtain the Hamiltonian in the context of quantum mechanics. This procedure can be found in any quantum mechanics textbook [31]. Variables q and p are taken to be Hermitian operators \hat{q} and \hat{p} representing position and momentum observables. Being conjugate coordinates, they must fulfill the following commutation rule:

$$\hat{q}\hat{p} - \hat{p}\hat{q} = [\hat{q}, \hat{p}] = i\hbar. \quad (2.4)$$

The total energy becomes the Hamiltonian operator:

$$\hat{H} = \frac{1}{2m}\hat{p}^2 + \frac{1}{2}m\Omega_m^2\hat{q}^2, \quad (2.5)$$

where $k = m\Omega_m^2$ has been used. The eigen-states and eigen-values in the q basis are found using $\hat{p} = -i\hbar\frac{\partial}{\partial q}$ and solving the resulting differential equation. The spectrum of eigen-energies is:

$$E_n = \hbar\Omega_m\left(n + \frac{1}{2}\right) \quad n = 0, 1, 2, \dots \quad (2.6)$$

The excitation number n is the *phonon number*. The behavior of the spectrum motivates the definition of a phonon-number basis:

$$|n\rangle \quad n = 0, 1, 2, \dots \quad (2.7)$$

which are usually called Fock or number states. They are eigen-states of the number operator:

$$\hat{n} = \frac{1}{\hbar\Omega_m}\hat{H} - \frac{1}{2} = \hat{b}^\dagger\hat{b}, \quad (2.8)$$

where \hat{b} is the annihilation operator and \hat{b}^\dagger is the creation operator, these are non-Hermitian operators that act on Fock states in the following way:

$$\hat{b}|n\rangle = \sqrt{n}|n-1\rangle \quad (2.9)$$

$$\hat{b}^\dagger|n\rangle = \sqrt{n+1}|n+1\rangle. \quad (2.10)$$

These are related to the \hat{q} and \hat{p} operators by the following identities:

$$\hat{b} = \sqrt{\frac{m\Omega_m}{2\hbar}} \left(\hat{q} + \frac{i}{m\Omega_m} \hat{p} \right) \quad (2.11)$$

$$\hat{b}^\dagger = \sqrt{\frac{m\Omega_m}{2\hbar}} \left(\hat{q} - \frac{i}{m\Omega_m} \hat{p} \right). \quad (2.12)$$

A key phenomena arising from quantization is the presence of intrinsic fluctuation in position measurements, even when the system is found at its lowest-energy state—the ground-state:

$$x_{z.p.}^2 = \langle 0 | \hat{q}^2 | 0 \rangle - \langle 0 | \hat{q} | 0 \rangle^2 = \frac{\hbar}{2m\Omega_m}. \quad (2.13)$$

These are known as zero-point fluctuations. Momentum measurements will also exhibit zero-point fluctuations:

$$p_{z.p.}^2 = \langle 0 | \hat{p}^2 | 0 \rangle - \langle 0 | \hat{p} | 0 \rangle^2 = \frac{\hbar m \Omega_m}{2}. \quad (2.14)$$

These characteristic quantities can be used to define dimensionless position and momentum operators \hat{Q} and \hat{P} :

$$\hat{Q} = \frac{1}{\sqrt{2}} \frac{\hat{q}}{x_{z.p.}} = \frac{1}{\sqrt{2}} (\hat{b}^\dagger + \hat{b}), \quad (2.15)$$

$$\hat{P} = \frac{1}{\sqrt{2}} \frac{\hat{p}}{p_{z.p.}} = \frac{i}{\sqrt{2}} (\hat{b}^\dagger - \hat{b}). \quad (2.16)$$

2.2.1 The open harmonic oscillator

The majority of harmonic oscillators that we can study experimentally are coupled to their environment, specially mechanical oscillators. A constant exchange of energy between the system of interest and its surroundings manifests itself as both heating and dissipation. The classical statistical physics approach will satisfactorily describe the oscillator at high temperatures but will fail at lower temperatures. At high temperatures, the thermal fluctuation of the coordinate q according to the equipartition theorem is [32]:

$$\langle q^2 \rangle = \frac{k_B T}{m\Omega_m^2}, \quad (2.17)$$

where k_B is the Boltzmann constant and T is the temperature of the surrounding environment, which is taken as a thermal bath. The classical approach clearly breaks down at low temperatures as it does not predict the fundamental zero-point fluctuations. We can find at which temperature T_q quantum fluctuations start to be relevant by comparing to Equation 2.13:

$$\langle q^2 \rangle = q_{z.p.}^2 = \frac{k_B T_q}{m\Omega_m^2} \implies T_q = \frac{\hbar \Omega_m}{2k_B}. \quad (2.18)$$

Now it becomes clear why light manifests clear quantum phenomena at room temperature wether mechanical resonators do not. The temperature requirement for near-infrared light is around 10^4 K, well above room-temperature. In the other hand, mechanical resonators with frequencies in the range from Hz up to GHz require temperatures down to 10pK and up to 10mK.

The rationale followed above is of course related to the thermal occupation of the harmonic oscillator. Taking the approach of quantum statistical mechanics, the canonical partition function is:

$$Z = \sum_{n=0}^{\infty} \exp\left\{-\frac{\hbar\Omega_m}{k_B T}(n+1/2)\right\}. \quad (2.19)$$

We can obtain the mean thermal phonon number, which follows Bose-Einstein statistics:

$$n_{\text{th}} = \langle \hat{n} \rangle = \bar{n}(\Omega_m) = \frac{1}{Z} \sum_{n=0}^{\infty} \exp\left\{-\frac{\hbar\Omega_m}{k_B T}(n+1/2)\right\} n = \frac{1}{\exp\left\{\frac{\hbar\Omega_m}{k_B T}\right\} - 1}, \quad (2.20)$$

and the position fluctuations in thermal equilibrium:

$$\langle \hat{q}^2 \rangle = \frac{1}{Z} \sum_{n=0}^{\infty} \exp\{-\beta\hbar\Omega_m(n+1/2)\} \langle n | \hat{q}^2 | n \rangle = q_{\text{z.p.}}^2 + 2q_{\text{z.p.}}^2 n_{\text{th}}. \quad (2.21)$$

It is evident that for quantum fluctuations to dominate, we must prepare our system in a low phonon occupation state.

2.2.2 Quantum dynamics of the open harmonic oscillator

Finding the time evolution of the oscillator's quantum state would, in principle, require us to keep track of evolution of its environment while it interacts with it. Doing so starts with a Hamiltonian of the form:

$$\hat{H} = \underbrace{\hat{H}_{\text{sys}}}_{\text{System of interest}} + \underbrace{\hat{H}_{\text{env}}}_{\text{Environment}} + \underbrace{H_{\text{sys-env}}}_{\text{Interaction}}. \quad (2.22)$$

In practice, we do not have experimental access to observables in the environment's Hilbert space. Furthermore, even if one had access to the observables, the environment usually has a much larger dimensionality than our system, for example, think of a mechanical oscillator connected to all the other mechanical modes of its surrounding medium.

Langevin equation approach

A possible approach to model the evolution of the harmonic oscillator open to its environment is to model the oscillator connected to an infinite number of mechanical oscillators through spring constants k_j . Working in the Heisenberg picture, this model can be reduced to the *Markovian quantum Langevin equation*, which describes the time evolution of operators. A detailed derivation can be found in [33] and a summary in Appendix A.

The Markovian quantum Langevin equation describing the evolution of an operator $\hat{O}(t)$ in the Heisenberg picture is:

$$\dot{\hat{O}}(t) = \frac{1}{i\hbar} [\hat{O}(t), \hat{H}_{\text{sys}}(t)] + i\sqrt{2\Gamma_m} [\hat{O}(t), \hat{Q}(t)] \hat{P}_{\text{in}}(t) + \frac{\Gamma_m}{2i\Omega_m} \{[\hat{O}(t), \hat{Q}(t)], \dot{\hat{Q}}(t)\}. \quad (2.23)$$

$\hat{P}_{\text{in}}(t)$ is an input momentum operator. It does not have the same units as \hat{P} because it is the rate of incoming momentum due to a stochastic force arising in the bath. In a thermalized bath,

the nature of $\hat{P}_{\text{in}}(t)$ is related to the quantum fluctuation-dissipation theorem [33], it has mean zero and the following power spectral density (PSD):

$$S_{\hat{P}_{\text{in}}\hat{P}_{\text{in}}}(\omega) = \frac{\omega}{\Omega_m}(\bar{n}(\omega) + 1) \quad (2.24a)$$

$$S_{\hat{P}_{\text{in}}\hat{P}_{\text{in}}}(-\omega) = \frac{\omega}{\Omega_m}\bar{n}(\omega) \quad (2.24b)$$

with $\omega \geq 0$ and $\bar{n}(\omega)$ is the occupation of a mode at ω introduced in Equation 2.20. The reader can refer to Appendix C for details about the conventions related to power spectral densities used in this work.

Making use of Equation 2.23, we find differential equations for $\hat{Q}(t)$ and $\hat{P}(t)$:

$$\dot{\hat{Q}} = \Omega_m \hat{P} \quad (2.25)$$

$$\dot{\hat{P}} = -\Omega_m \hat{Q} - \Gamma \hat{P} + \sqrt{2\Gamma_m} \hat{P}_{\text{in}}, \quad (2.26)$$

which we can cast into a single second-order differential equation by differentiating the first expression:

$$\ddot{\hat{Q}} + \Gamma_m \dot{\hat{Q}} + \Omega_m^2 \hat{Q} = \Omega_m \sqrt{2\Gamma_m} \hat{P}_{\text{in}}. \quad (2.27)$$

The equation is better solved in frequency space. The Fourier transform definition used across this work is:

$$\hat{A}(\omega) = \mathcal{F}\{\hat{A}(t)\}(\omega) = \int_{-\infty}^{\infty} e^{i\omega t} \hat{A}(t) dt, \quad (2.28)$$

so that $\mathcal{F}\left\{\frac{d^n \hat{A}(t)}{dt^n}\right\}(\omega) = (-i\omega)^n \mathcal{F}\{\hat{A}(t)\}(\omega)$. Making use of this identity we find:

$$\hat{Q}(\omega) = \frac{\Omega_m}{\underbrace{\Omega_m^2 - \omega^2 - i\omega\Gamma_m}_{\chi_m(\omega)}} \sqrt{2\Gamma_m} \hat{P}_{\text{in}}(\omega), \quad (2.29)$$

where the mechanical susceptibility $\chi_m(\omega)$ has been introduced. Different conventions for the mechanical susceptibility exist across the literature depending if it is defined in terms of dimensional or dimension-less operators. The PSD of \hat{Q} can be found making use of Equation C.13:

$$S_{\hat{Q}\hat{Q}}(\omega) = |\chi_m(\omega)|^2 S_{\hat{P}_{\text{in}}\hat{P}_{\text{in}}}(\omega). \quad (2.30)$$

$S_{\hat{Q}\hat{Q}}(\omega)$ thus inherits the asymmetry arising from the quantum fluctuation-dissipation theorem seen in Equation 2.24. The asymmetry is exclusive to the quantum treatment, in the classical limit of $\bar{n} \gg 1$ the asymmetry is negligible $\bar{n}(\Omega_m) + 1 \simeq \bar{n}(\Omega_m)$. If one has experimental access to $S_{\hat{Q}\hat{Q}}(\omega)$, the occupation of the oscillator can be measured without calibration using the size of the asymmetry:

$$\frac{S_{\hat{Q}\hat{Q}}(\Omega_m)}{S_{\hat{Q}\hat{Q}}(-\Omega_m)} = \frac{\bar{n}(\Omega_m) + 1}{\bar{n}(\Omega_m)}, \quad (2.31)$$

where we have used the fact that $|\chi_m(\omega)|^2 = |\chi_m(-\omega)|^2$. With proper calibration, the phonon occupation can be found from the area under $S_{\hat{Q}\hat{Q}}$ (using the relation between position fluctuations and occupation found in Equation 2.21 together with Equation C.11):

$$\langle \hat{n} \rangle + \frac{1}{2} = \langle \hat{Q}^2 \rangle = \frac{1}{2\pi} \int_{-\infty}^{\infty} S_{\hat{Q}\hat{Q}}(\omega) d\omega = \frac{1}{\pi} \int_0^{\infty} \bar{S}_{\hat{Q}\hat{Q}}(\omega) d\omega, \quad (2.32)$$

where I have introduced the symmetrized PSD of an operator: $\bar{S}_{\hat{\phi}\hat{\phi}}(\omega) = \frac{1}{2}[S_{\hat{\phi}\hat{\phi}}(\omega) + S_{\hat{\phi}\hat{\phi}}(-\omega)]$. The symmetrized PSD is important because a real-valued variable must have symmetric PSD. Various experimental detection techniques provide a measurement of the symmetrized $\bar{S}(\omega)$ but not of the possibly asymmetric $S(\omega)$.

2.2.3 Cavity-free optomechanical interaction

To finish our discussion about the harmonic oscillator, let us imagine the simplest optomechanical configuration, a light beam impinging on a mechanical oscillator. A continuous laser beam has a certain mean photon rate $\langle \dot{N} \rangle = \frac{P}{\hbar\omega_l}$, with P its power (measured in Watts) and ω_l its angular frequency (measured in radians per second). If the beam is in a coherent state with no classical noise sources, the variance in the amount of photons received in a time interval Δt is [24]:

$$\langle N^2 \rangle - \langle N \rangle^2 = \langle \dot{N} \rangle \Delta t, \quad (2.33)$$

due to the Poissonian statistics of the coherent state. It follows that the radiation pressure that the beam exerts upon reflection has mean value:

$$\langle F_{\text{opt}} \rangle = \frac{2\hbar\omega_l}{c} \mathcal{R} \langle \dot{N} \rangle, \quad (2.34)$$

and a power spectral density:

$$S_{F_{\text{opt}}F_{\text{opt}}} = \frac{4\hbar^2\omega_l^2}{c^2} \mathcal{R}^2 \langle \dot{N} \rangle, \quad (2.35)$$

these expressions have been obtained by considering that each photon carries a momentum equal to $\hbar\omega_l/c$ and a fraction $0 \leq \mathcal{R} \leq 1$ is actually reflected off of the object due to limited reflectivity. We can think about radiation pressure as the combination of a static force that shifts the rest position of the oscillator plus a stochastic force of quantum origin.

With the goal of comparing it with the thermal force, let's consider a $\lambda = 1550\text{nm}$ laser beam with power $P = 10\text{mW}$ illuminating a Silicon-Nitride membrane nanomechanical resonator of frequency $\Omega_m = 2\pi \cdot 1\text{MHz}$, mass of $m = 2\text{ng}$, dissipation rate of $\Gamma_m = 2\pi \cdot 10\text{MHz}$ and reflectivity of $\mathcal{R} = 1.5\%$. The average radiation pressure is $\langle F_{\text{opt}} \rangle \simeq 1\text{pN}$, causing a static displacement of around 12fm . The magnitude of the stochastic force is $S_{F_{\text{opt}}F_{\text{opt}}}^{1/2} \simeq 3.6 \times 10^{-21} \text{N}/\sqrt{\text{Hz}}$, which is orders of magnitude smaller compared to that of the thermal force, given by the classical fluctuation dissipation theorem, $S_{F_{\text{th}}F_{\text{th}}}^{1/2} = \sqrt{2m\Gamma_mk_B T} = 3.2 \times 10^{-17} \text{N}/\sqrt{\text{Hz}}$.

The disparity between the quantum and the thermal fluctuations can be addressed without the need of lowering the temperature by using oscillators with smaller mass and higher quality factor (levitated nano-particles for example), or by using higher optical power. In the next section, we will take a look at optical cavities, which allow us to build up optical power and reach a regime dominated by quantum phenomena.

2.3 Optical cavities

An *optical cavity* or *optical resonator* is a system where one or more optical modes propagate cyclically in a closed space. The simplest optical cavity consists in trapping light within two highly reflective mirrors, like shown in Figure 2.1. Let us label the mirrors as mirror 1 and 2. If we illuminate mirror 1 with coherent light, a small fraction of light will transmit through it

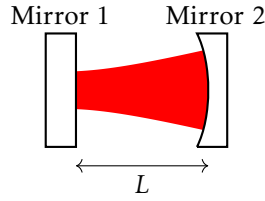


Figure 2.1: An optical cavity can be set up using two highly reflective mirrors, one of them must be curved in order to refocus the beam after each round trip.

and bounce back and forth between the two mirrors. Light with specific wavelengths will constructively interfere, creating a standing wave between the mirrors. Of course, one of the two mirrors must be curved, as to compensate for the diffraction of the beam as it travels between the two mirrors. Input light of the right wavelength and shape will build-up the field inside the cavity, which will then exit through both mirrors.

In this work, we exploit the field enhancement by a cavity in order to get closer to the quantum optomechanical regime at room temperature. Before showing how a mechanical resonator can interact with a cavity, we give a brief description of the linear Fabry-Perot cavity. First, we find the resonant wavelengths and spatial modes according to classical optics. Then we proceed with the quantum mechanical picture of the optical cavity.

2.3.1 The resonant modes and spectrum of an optical cavity

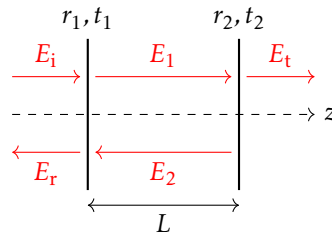


Figure 2.2: One-dimensional model of a linear Fabry-Perot cavity. Two mirrors are modeled as thin interfaces for convenience.

If we scan the frequency of a light source going into a cavity, we will see peaks of light transmission at the resonant frequencies, which are accompanied by drops in the amount of reflected light. We can model this behavior, forgoing any modeling of the spatial mode of the light, with a one-dimensional picture as illustrated in figure 2.2. Two mirrors are separated by a distance L , which we will consider as infinitesimally thin interfaces with field transmissivity and reflectivity $\mathcal{T}_1, \mathcal{T}_2, \mathcal{R}_1$ and \mathcal{R}_2 . We consider three external optical modes, the incoming E_i , the reflected E_r and the transmitted E_t , and one internal mode split into a z -positive propagating part E_1 and

a z-negative propagating part E_2 . The fields must fulfill the following boundary conditions:

$$E_1 = it_1 E_i + r_1 E_2 e^{-ikL} \quad (2.36)$$

$$E_2 = r_2 E_1 e^{-ikL} \quad (2.37)$$

$$E_r = r_1 E_i + ir_1 E_2 e^{-ikL} \quad (2.38)$$

$$E_t = ir_2 E_1 e^{-ikL}, \quad (2.39)$$

where $k = \frac{2\pi}{\lambda}$ is the wave number of the light. We can easily find the fields as a function of the incoming field E_i :

$$E_1 = \frac{ir_1}{1 - r_1 r_2 e^{-i2kL}} E_i \quad (2.40)$$

$$E_2 = \frac{it_1 r_2 e^{-ikL}}{1 - r_1 r_2 e^{-i2kL}} E_i \quad (2.41)$$

$$E_r = \left(r_1 - \frac{t_1^2 r_2}{e^{i2kL} - r_1 r_2} \right) E_i \quad (2.42)$$

$$E_t = \frac{it_1 t_2 e^{-ikL}}{1 - r_1 r_2 e^{-i2kL}} E_i, \quad (2.43)$$

the ratio reflected and transmitted power to input power can be obtained by taking the absolute value squared of these expressions. These are periodic functions of k with a period $\frac{\pi}{L}$ and thus also of ω , the angular frequency, with period $\frac{\pi c}{L}$. This quantity is known as the *free spectral range* (FSR) of the cavity. The peaks in transmission and dips in reflection will be spaced one FSR from each other. The absolute resonant frequencies will depend on the cavity length L and the phases induced in reflection $\phi_{\mathcal{R}_1}$ and $\phi_{\mathcal{R}_2}$ ($r_j = |r_j| e^{i\phi_{r_j}}$). We can find the resonant frequencies from the transmitted power ratio:

$$\mathcal{T}_{\text{cav}} = \left| \frac{E_t}{E_i} \right|^2 = \frac{\mathcal{T}_1 \mathcal{T}_2}{1 + \mathcal{R}_1 \mathcal{R}_2 - 2\sqrt{\mathcal{R}_1 \mathcal{R}_2} \cos(2kL - \phi_{\mathcal{R}_1} - \phi_{\mathcal{R}_2})}, \quad (2.44)$$

where $\mathcal{T}_j = |r_j|^2$ and $\mathcal{R}_j = |r_j|^2$. \mathcal{T}_{cav} will be maximized at wave numbers k_n :

$$k_m = k_{\text{FSR}} \cdot m + \frac{1}{2L} (\phi_{\mathcal{R}_1} + \phi_{\mathcal{R}_2}) \quad (m \in \mathbb{Z}^+), \quad (2.45)$$

similarly:

$$\omega_m = \omega_{\text{FSR}} \cdot m + \frac{c}{2L} (\phi_{\mathcal{R}_1} + \phi_{\mathcal{R}_2}) \quad (m \in \mathbb{Z}^+). \quad (2.46)$$

With the goal of finding the linewidth of the resonant peaks, we will proceed with the approximation of small detunings compared to FSR: $\Delta = \omega_l - \omega_c \ll \omega_{\text{FSR}}$, with ω_l being the frequency of the light pumping the cavity and ω_c being a certain resonance frequency of the cavity. In this case.

$$\mathcal{T}_{\text{cav}}(\Delta) \simeq \frac{\mathcal{T}_1 \mathcal{T}_2}{(1 - \sqrt{\mathcal{R}_1 \mathcal{R}_2})^2} \frac{\kappa^2/4}{\kappa^2/4 + \Delta^2}, \quad (2.47)$$

where:

$$\kappa = \frac{\omega_{\text{FSR}}}{\mathcal{F}} \quad (2.48)$$

is the full-width half-maximum (FWHM) linewidth of the resonance and \mathcal{F} is the finesse:

$$\mathcal{F} = \frac{\pi(\mathcal{R}_1\mathcal{R}_2)^{\frac{1}{4}}}{1 - \sqrt{\mathcal{R}_1\mathcal{R}_2}}. \quad (2.49)$$

In order to model losses, we have been careful in considering $\mathcal{R}_j + \mathcal{T}_j \neq 1$. Losses play a big role in the transmission and reflection spectra of the cavity, which will be discussed in a later section.

The obvious flaw in the one-dimensional model is that it fails to consider the diffraction of the beam. Two planar mirrors cannot form a stable cavity, at least one of the mirrors must be curved in order to refocus the beam after each round-trip. For a given cavity geometry, with mirror radius of curvature R_1 , R_2 and length L , there is only one combination of waist position z_0 and waist size w_0 that remain equal after one round-trip. This fact still allows for an infinite number of possible transverse spatial modes: the Hermite-Gaussian beams (if the cavity is made with spherical mirrors and is well described by the paraxial approximation).

The reader can refer to the work of Kogelnik and Li [34] for a detailed derivation of the cavity mode's waist size and position. Following is a summary of their method and results. Using the ray transfer matrix method, we find how the *complex beam parameter* changes after one round-trip. The complex beam parameter q at a point of the optical axis is defined by the curvature R and radius w of the beam:

$$\frac{1}{q} = \frac{1}{R} - i\frac{\lambda}{\pi w^2}. \quad (2.50)$$

Starting with the complex beam parameter of the cavity mode at mirror 1 q_1 , the ABCD matrix associated with one round-trip is:

$$\begin{pmatrix} A & B \\ C & D \end{pmatrix} = \underbrace{\begin{pmatrix} 1 & 0 \\ -\frac{2}{R_1} & 1 \end{pmatrix}}_{\text{Mirror 1 reflection}} \cdot \underbrace{\begin{pmatrix} 1 & L \\ 0 & 1 \end{pmatrix}}_{\text{Propagation } 2 \rightarrow 1} \cdot \underbrace{\begin{pmatrix} 1 & 0 \\ -\frac{2}{R_2} & 1 \end{pmatrix}}_{\text{Mirror 2 reflection}} \cdot \underbrace{\begin{pmatrix} 1 & L \\ 0 & 1 \end{pmatrix}}_{\text{Propagation } 1 \rightarrow 2}. \quad (2.51)$$

The beam is then transformed according to:

$$q'_1 = \frac{Aq_1 + B}{Cq_1 + D}. \quad (2.52)$$

Now we impose the condition $q_1 = q'_1$ and solve to find the cavity mode's waist and position (measured from mirror 1):

$$w_{0,c}^2 = \frac{\lambda L}{\pi} \sqrt{\frac{G_1 G_2 (1 - G_1 G_2)}{(G_1 + G_2 - 2G_1 G_2)^2}}, \quad (2.53)$$

$$z_{0,c} = \frac{L(R_2 - L)}{R_1 + R_2 - 2L} \quad (2.54)$$

where $G_i = 1 - \frac{L}{R_i}$. From equation (2.53) we can extract the stability criterion of the cavity by ensuring a real $w_{0,c}$:

$$0 \leq G_1 G_2 \leq 1. \quad (2.55)$$

Finally, we must consider that the phase of a Hermite-Gaussian beam evolves differently than that of a plane-wave, it acquires an additional phase called the Gouy phase. The Gouy phase of

a beam of orders m, n along the optical axis is:

$$\Phi_{m,n}(z) = (m + n + 1) \arctan\left(\frac{\lambda}{\pi w_0^2} z\right). \quad (2.56)$$

This fact modifies our resonance condition to:

$$\omega_{l,m+n} = \omega_{\text{FSR}} \cdot l + \frac{c}{2L} (\phi_{\mathcal{R}_1} + \phi_{\mathcal{R}_2}) + \omega_{\text{FSR}} \frac{1}{\pi} (m + n + 1) \arccos \sqrt{G_1 G_2} \quad (l \in \mathbb{Z}^+). \quad (2.57)$$

The spectrum of higher-order transverse modes is frequency shifted respect to the HG_{00} mode, but it retains the same free spectral range. This effect proves to be very useful for characterizing the geometry of a cavity.

2.3.2 Quantum dynamics of optical cavities

The quantization of the electromagnetic fields of a cavity is at the core of quantum optics. The procedure can be found in any quantum optics textbook, for example, *Introductory Quantum Optics* by Gerry and Knight [35]. I will skip a detailed derivation and start from the Hamiltonian of one of the resonant modes of the cavity, which is that of a harmonic oscillator:

$$\hat{H} = \hbar \omega_c \left(\hat{a}^\dagger \hat{a} + \frac{1}{2} \right), \quad (2.58)$$

where \hat{a}^\dagger and \hat{a} are the creation and annihilation operators, adding and removing one photon to the cavity. $\hat{a}^\dagger \hat{a} = \hat{n}$ is the number operator, which is hermitian and represents the number of photons in the cavity. \hat{a}^\dagger and \hat{a} are non-commuting:

$$[\hat{a}, \hat{a}^\dagger] = \mathbb{I}. \quad (2.59)$$

In the Heisenberg picture, the time-evolution of operators can easily be found using the Heisenberg equation $\dot{\hat{O}} = \frac{1}{i\hbar} [\hat{O}, \hat{H}]$. To model a real cavity and not just an ideal cavity with perfectly reflecting mirrors, we must include the connection of the cavity mode with external modes through both mirrors and through possible loss channels.

We will use a quantum Langevin equation, particularly the one presented in Chapter 1.4 in the book *Quantum Optomechanics* by Bowen and Milburn [33]:

$$\dot{\hat{O}} = \frac{1}{i\hbar} [\hat{O}, \hat{H}] + \sum_{i=1,2,\ell} \left\{ -[\hat{O}, \hat{a}^\dagger] \left(\frac{\kappa_i}{2} \hat{a} - \sqrt{\kappa_i} \hat{a}_{\text{in},i} \right) + \left(\frac{\kappa_i}{2} \hat{a}^\dagger - \sqrt{\kappa_i} \hat{a}_{\text{in},i}^\dagger \right) [\hat{O}, \hat{a}] \right\}, \quad (2.60)$$

here we consider three channels, mirror 1 and 2, with associated rates κ_1 and κ_2 , and a loss channel with rate κ_ℓ , which encompasses all connections to optical modes that we are incapable of measuring. Some important approximations have been done in order to arrive at the expression (2.60):

- The Rotating Wave Approximation (RWA) assumes that all coupling rates connecting to external modes (κ_i) are much smaller than the characteristic frequencies of the system (in this case ω_c). This is a very sensible approximation for quantum optics, as the optical frequency is beyond THz.
- The Markovian approximation, stochastic processes in the bath are assumed to be delta correlated.

- Thermal effects have not been considered due to $\hbar\omega_c \gg k \cdot 300\text{K}$.

We use equation (2.60) to find the time evolution of \hat{a} and \hat{a}^\dagger in the Heisenberg picture:

$$\dot{\hat{a}}(t) = -\left(\frac{\kappa}{2} + i\hat{\Delta}(t)\right)\hat{a}(t) + \sum_{i=1,2,\ell} \sqrt{\kappa_i} \hat{a}_{\text{in},i}(t), \quad (2.61)$$

$$\dot{\hat{a}}^\dagger(t) = -\left(\frac{\kappa}{2} - i\hat{\Delta}(t)\right)\hat{a}^\dagger(t) + \sum_{i=1,2,\ell} \sqrt{\kappa_i} \hat{a}_{\text{in},i}^\dagger(t), \quad (2.62)$$

where we have moved to a rotating frame of the input laser frequency ω_l , and we have allowed the cavity's resonant frequency to evolve over time, including a dependency on quantum observables (hence the hat). We have also defined $\kappa = \kappa_1 + \kappa_2 + \kappa_\ell$. In the next paragraphs, it will become apparent that this is the same linewidth obtained in the classical treatment of the optical cavity. It is important to state that operators $\hat{a}_{\text{in},i}$ are photon rate operators, normalized so that $\hat{a}_{\text{in},i}^\dagger \hat{a}_{\text{in},i}$ has units of (photons/s) instead of (photons).

In experiments with high finesse cavities, the average number of photons in the cavity is much larger than the quantum fluctuations of the field. It becomes convenient to split the operators into a steady-state classical contribution and a fluctuation term including both classical stochastic processes and quantum behavior:

$$\hat{a}(t) = \alpha + \delta\hat{a}(t), \quad (2.63)$$

$$\hat{a}_{\text{in},i}(t) = \alpha_{\text{in},i} + \delta\hat{a}_{\text{in},i}(t). \quad (2.64)$$

$$\hat{\Delta}(t) = \bar{\Delta} + \delta\hat{\Delta}(t). \quad (2.65)$$

We will consider the cavity being pumped exclusively from port 1, so that $\alpha_{\text{in},1} \neq 0$ and $\alpha_{\text{in},2} = \alpha_{\text{in},\ell} = 0$. Vacuum fluctuations will enter the cavity from each port and thus $\delta\hat{a}_{\text{in},i}(t) \neq 0$ despite a non-existing mean field.

The steady-state fields

By setting the time derivatives in equation (2.61) to zero, we find the steady-state intra-cavity field:

$$\alpha = \frac{\sqrt{\kappa_1}}{\frac{\kappa}{2} + i\bar{\Delta}} \alpha_{\text{in},1}, \quad (2.66)$$

and intra-cavity photon number:

$$n_c = |\alpha|^2 = \frac{\kappa_1}{\frac{\kappa^2}{4} + \bar{\Delta}^2} |\alpha_{\text{in},1}|^2. \quad (2.67)$$

The output fields can be found using the input-output relations [36]:

$$\hat{a}_{\text{out},i}(t) = \hat{a}_{\text{in},i}(t) - \sqrt{\kappa_i} \hat{a}, \quad (2.68)$$

where $\hat{a}_{\text{out},i}$ are also photon-rate operators. The steady-state reflected and transmitted field are:

$$\alpha_{\text{out},1} = \underbrace{\frac{\frac{\kappa-2\kappa_1}{2} + i\bar{\Delta}}{\frac{\kappa}{2} + i\bar{\Delta}}}_{r_{\text{cav}}(\bar{\Delta})} \alpha_{\text{in},1} \quad (2.69)$$

$$\alpha_{\text{out},2} = -\underbrace{\frac{\sqrt{\kappa_1 \kappa_2}}{\frac{\kappa}{2} + i\bar{\Delta}}}_{t_{\text{cav}}(\bar{\Delta})} \alpha_{\text{in},1}, \quad (2.70)$$

Finally the steady reflected and transmitted photon rates are:

$$|\alpha_{\text{out},1}|^2 = \underbrace{\frac{\frac{(\kappa-2\kappa_1)^2}{4} + \bar{\Delta}^2}{\frac{\kappa^2}{4} + \bar{\Delta}^2}}_{\mathcal{R}_{\text{cav}}(\bar{\Delta})} |\alpha_{\text{in},1}|^2, \quad (2.71)$$

$$|\alpha_{\text{out},2}|^2 = \underbrace{\frac{\kappa_1 \kappa_2}{\frac{\kappa^2}{4} + \bar{\Delta}^2}}_{\mathcal{T}_{\text{cav}}(\bar{\Delta})} |\alpha_{\text{in},1}|^2. \quad (2.72)$$

These expressions are consistent with the classical approach. In particular, comparing equation (2.72) to equation (2.47), we see how κ is the same FWHM linewidth of the Lorentzian shaped resonance. We will now use equations (2.69), (2.70), (2.71) and (2.72) to identify three interesting regimes depending on the relation between the different decay rates, which illustrated in figure 2.3:

- $\kappa_1 \simeq \kappa$: If the coupling rate of the input mirror dominates over the other rates, the reflected power will be flat as light that enters the cavity exits through the same port ($\mathcal{R}_{\text{cav}} \simeq 1$ and $\mathcal{T}_{\text{cav}} \simeq 0$). Despite the flatness of the cavity spectrum in terms power, the cavity still has a strong effect on the phase of the reflected beam $r_{\text{cav}}(\Delta = 0) \simeq -1$. This regime is often referred to as the *overcoupled* regime.
- $\kappa_1 = \kappa/2$: Lowering the weight of κ_1 respect to the other rates, the dip in reflectivity becomes deeper. The behavior is maximized when the condition $\kappa_1 = \kappa/2$ is fulfilled. In this regime, all input light that enters the cavity exits through the end mirror and the loss channel. This causes the reflection to dip to zero at zero detuning: $\mathcal{R}_{\text{cav}}(\Delta = 0) = 0$. The amount of light transmitted will depend on the ratio κ_1/κ .
- $\kappa \simeq \kappa_\ell \gg \kappa_1, \kappa_2$. If the loss rate dominates, light that enters the cavity exits mainly through the loss channel, this reduces the dip in the reflection field $\mathcal{R}_{\text{cav}}(\Delta = 0) \simeq 1$ and the amount of transmission $\mathcal{T}_{\text{cav}}(\Delta = 0) \simeq 0$. Even if the spectrum in terms of power looks similar to the overcoupled regime, the reflected beam does not acquire much phase $r_{\text{cav}} \simeq 1$. This regime is often called the *undercoupled* regime and is rarely of use as the cavity acts as a simple mirror of reflectivity \mathcal{R}_1 .

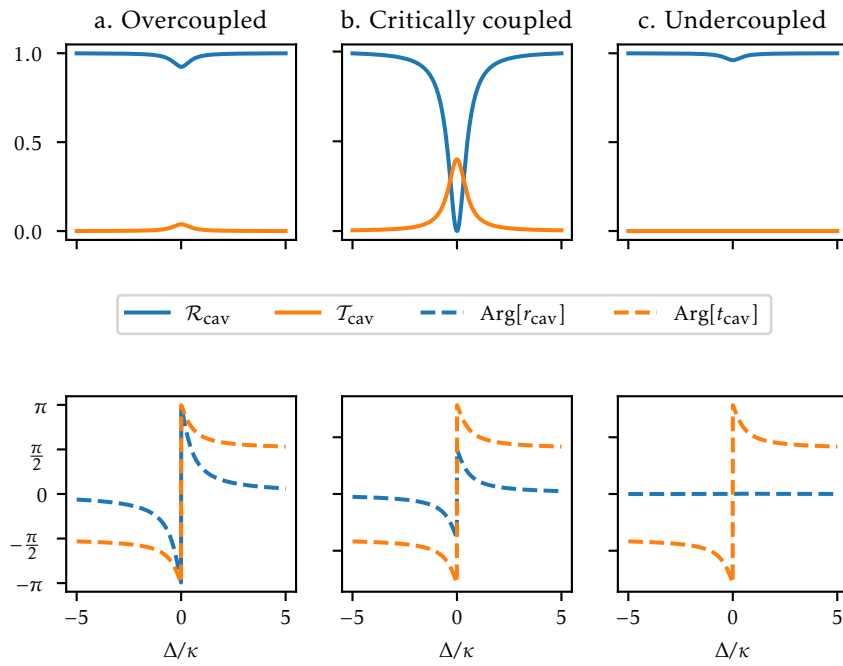


Figure 2.3: Cavity response in reflection and transmission, upper row is the optical power reflected and transmitted normalized to input power and lower row is the phase. In subfigure a., $\kappa_1 = 100\kappa_2 = 100\kappa_\ell$, b. $\kappa_1 = \kappa/2$, $\kappa_2 = \kappa/5$, $\kappa_\ell = 3\kappa/10$, c. $\kappa_\ell = 100\kappa_1 = 100\kappa_2$

2.4 The dispersive optomechanical hamiltonian

Dispersive cavity optomechanics describes systems where the displacement of a mechanical oscillator causes changes in the resonant frequency of an optical cavity. The interaction could also be *dissipative* if the mechanical oscillator changes the coupling of the cavity to external modes. Dissipative cavity optomechanics has been explored considerably less than its dispersive counterpart. In this work, we will follow such tradition.

The canonical dispersive cavity optomechanics system is a cavity with a mirror attached to a spring, such as the one depicted in figure 2.4. A displacement of the compliant mirror q changes the length of the cavity, which changes the resonant condition. A certain resonant mode with mode number m will change according to:

$$\omega_{c,m} = m \frac{\pi c}{L+q} = \omega_{c,m,0} - \underbrace{\frac{\omega_{c,m,0}}{L}}_G \cdot q + \mathcal{O}(q^2), \quad (2.73)$$

if $q \ll L$, which is a common occurrence in most experiments, we obtain a linear dependence between displacement and cavity frequency. The parameter connecting both is referred to as G and has units of Hz/m. The strength of the transduction is proportional to the resonant frequency and inversely proportional to the length of the cavity. An intuitive way of understanding the first dependence is that the phase added to the intracavity light by displacement q inversely scales with wavelength (in other words, the smaller the wavelength, the better the interferometer). The fact that $G \propto L^{-1}$ is less intuitive.

A Hamiltonian for the optomechanical interaction in a cavity can be found thanks to this relation. The Hamiltonian that follows will be valid for the dispersive interaction of any system dominated by $\frac{\partial \omega_c}{\partial q} = G$. Starting from the Hamiltonian of an optical cavity of frequency $\omega_c - Gq$, with q being the displacement of a mechanical oscillator of frequency Ω_m :

$$\hat{H} = \hbar(\omega_c - G\hat{q})\hat{a}^\dagger \hat{a} + \hbar\Omega_m \hat{b}^\dagger \hat{b}, \quad (2.74)$$

which we can split into a bare Hamiltonian \hat{H}_0 and an interaction Hamiltonian \hat{H}_1 :

$$\hat{H} = \underbrace{\hbar\omega_c \hat{a}^\dagger \hat{a} + \hbar\Omega_m \hat{b}^\dagger \hat{b}}_{\hat{H}_0} + \underbrace{\hbar g_0 (\hat{b} + \hat{b}^\dagger) \hat{a}^\dagger \hat{a}}_{\hat{H}_1}, \quad (2.75)$$

where, making use of the relation $\hat{q} = x_{z,p}(\hat{b} + \hat{b}^\dagger)$, we have introduced the *single-photon coupling strength* $g_0 = Gx_{z,p}$ with units of rad · Hz. g_0 is an interesting figure of merit because it deter-

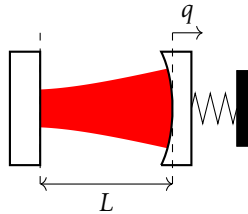


Figure 2.4: The canonical dispersive optomechanical system. A Fabry-Perot cavity with a mirror attached to a spring.

mines the strength of processes involving the creation and annihilation of single phonons and photons.

2.5 Membrane-in-the-middle cavity optomechanics

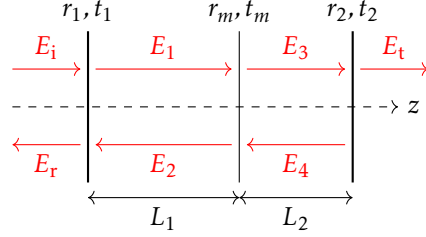


Figure 2.5: One-dimensional model of a membrane-in-the-middle experiment. Both mirrors and membrane are modeled as thin interfaces.

Building a cavity optomechanics experiment in the moving end-mirror configuration is challenging because we need a mirror with high-reflectivity, large zero-point fluctuations and low dissipation rate. In the past years, great steps have been managed towards this goal through adding photonic crystal reflectors on thin silicon-nitride membranes. Starting with the first proof of concept by Norte et al[17], high-finesse systems have been achieved in the work by Zhou et al[37] and Enzian et al[38]. Going even further, the photonic crystal mirror can also act as a curved mirror by engineering the phase that is reflected as done in the recent work by Agrawal et al[39].

In this work, we have opted to build a *membrane-in-the-middle* of a cavity system (MIM). In this configuration pioneered by Thompson et al[40], a partially reflecting membrane sits in the space between the two mirrors of a high-finesse optical cavity. Suspended silicon-nitride resonators are ideal for the MIM configuration due to their partial reflectivity and their low optical absorption. Furthermore, by eliminating the need of high-reflectivity, the focus has been on increasing their quality factor. Optimal design of trampolines and phononic crystal structured membranes have pushed the quality factor of SiN membranes more than two order of magnitude compared to a simple square window design. We will leave the discussion of the mechanical resonator used in this work for Chapter 3.

In the rest of this section, we will summarize the analysis of the optomechanical interaction in MIM systems following the approach found in [41]. We set up a one-dimensional model as we did in Section 2.3, but we now add an extra thin interface to represent the membrane, as illustrated in Figure 2.5. The membrane has field reflectivity and transmissivity r_m and t_m , given by the following expressions[41]:

$$r_m = \frac{(n^2 - 1) \sin knL_m}{2in \cos knL_m + (n^2 + 1) \sin knL_m} \quad (2.76)$$

$$t_m = \frac{2n}{2in \cos knL_m + (n^2 + 1) \sin knL_m}, \quad (2.77)$$

where n is the possibly complex refractive index and L_m is the thickness of the membrane. The reflectivity for a 20nm thin SiN membrane ($n \simeq 2$) is around 1.4% in the wavelengths where the experiment can be operated. Figure 2.6 shows its dependency on wavelength.

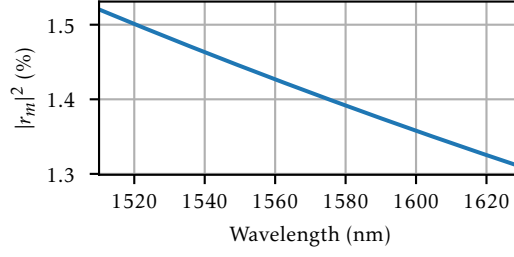


Figure 2.6: Theoretical reflectivity of a 20nm thin SiN membrane ($n \simeq 2$) at different wavelengths

The set of equations given by the boundary conditions of the fields inside a MIM are the following:

$$E_1 = it_1 E_i + r_1 E_2 e^{-ikL_1} \quad (2.78a)$$

$$E_2 = r_m E_1 e^{-ikL_1} + it_m E_4 e^{-ikL_2} \quad (2.78b)$$

$$E_3 = it_m E_1 e^{-ikL_1} + r_m E_4 e^{-ikL_2} \quad (2.78c)$$

$$E_4 = r_2 E_3 e^{-ikL_2} \quad (2.78d)$$

$$E_r = r_1 E_1 + it_1 E_2 e^{-ikL_1} \quad (2.78e)$$

$$E_t = it_2 E_3 e^{-ikL_2}, \quad (2.78f)$$

this is an easily solvable linear system of equations, albeit the solutions are quite cumbersome to write down. In the other hand, the cavity resonant condition, which can be found by imposing that the phase of the transmitted field be a multiple of π , results in a transcendental equation [41, 42]:

$$|r_m| \cos[k_c^{\text{MIM}}(L_1 - L_2)] = \cos[k_c^{\text{MIM}}(L_1 + L_2) - \arg(t_m)], \quad (2.79)$$

with k_c^{MIM} being a resonant wave number. We can find an approximate solution by considering that the membrane is located near the center of the cavity, so that $L_1 - L_2$ is small compared to L . Furthermore, if we also assume that the change in resonant wave number is small compared to the empty cavity resonant wave number k_c , we can approximate the argument of the left-hand side cosine as $k_c^{\text{MIM}}(L_1 - L_2) \approx k_c(L_1 - L_2)$. Now it is straight-forward to find:

$$\omega_c^{\text{MIM}} \simeq \frac{\omega_{\text{FSR}}}{\pi} \left[\arg(t_m) + \arccos \left\{ |r_m| \cos \left[\frac{\omega_c}{c} (L - 2q) \right] \right\} \right], \quad (2.80)$$

where we have included the position of the membrane q with origin at the first mirror, so that $q = L_1 = L - L_2$. In order to find the optomechanical transduction factor G , we must evaluate the derivative $G = \frac{d\omega_c^{\text{MIM}}}{dq}$:

$$G^{\text{MIM}} = \frac{d\omega_c^{\text{MIM}}}{dq} = -2|r_m| \frac{\omega_c}{L} \frac{\sin[k_c(L - 2q)]}{\sqrt{1 - |r_m|^2 \cos^2[k_c(L - 2q)]}}. \quad (2.81)$$

Contrary to the canonical case, G^{MIM} depends on q , vanishing when q fulfills:

$$q = \frac{L}{2} - \frac{\lambda_c}{4} n \quad n = 0, \pm 1, \pm 2, \dots \quad (2.82)$$

At $L/2$ there is always a field node (for odd mode numbers) or an anti-node (for even mode numbers). Moving by an amount $\lambda_c/4$, the next node or anti-node is reached. Thus, we can conclude that the optomechanical coupling is zero when the membrane sits at a field node or anti-node. At the mid-point between a node and an anti-node, the maximum coupling is reached, which for a given length is:

$$|G^{\text{MIM}}| = 2|r_m|\frac{\omega_c}{L} = 2|r_m|G. \quad (2.83)$$

Usually, the factor $2|r_m|$ is below one and we achieve less coupling than if we were in a moving end-mirror configuration. Looking at Figure 2.6, at $\lambda = 1550\text{nm}$, a MIM system with a 20nm thick Silicon-Nitride membrane will have roughly a fourth of the optomechanical coupling of that of a moving-end mirror configuration ($2|r_m| \simeq 0.24$). It seems quite remarkable that MIM can achieve similar performance in terms of coupling. However, in the next chapters we will find that the cooperativity, which is the important figure of merit, depends quadratically on the coupling rate. If a sufficiently reflective resonator is used, such as the 85nm thick trampoline used in the work by Pluchar et al [43], $2|r_m| > 1$ and the MIM system should theoretically perform better than an equivalent moving end-mirror configuration. In practice, the approximations that we have done might not hold for membranes of high-reflectivity.

It is worth to numerically obtain the spectrum of a MIM system to both check that our approximation is valid as well as understand how the presence of the membrane alters the linewidth of the cavity. We will do so by using the *Python* library *SymPy* [44] to symbolically solve Equation 2.78 and obtain an expression for the transmitted field. We identify the resonances with a peak finding algorithm. By finding the resonant frequencies a second time after moving the membrane by 100pm, we can use the difference in frequency to estimate G through $G = \Delta\omega_c/100\text{pm}$. The linewidth at each resonant mode is measured by fitting a Lorentzian peak function. For the following calculations, we will use the parameters of the actual experiment, which are described in Chapter 3. The MIM system implemented is completely rigid, the length is fixed to $L = 126\mu\text{m}$ with the 20nm thick Silicon-Nitride membrane sitting $L_1 = 58\mu\text{m}$ away from the first mirror. We will also use the mirror properties of our experiment, with transmissions $\mathcal{T}_1 = 100\text{ppm}$ and $\mathcal{T}_2 = 10\text{ppm}$.

We first look at the transmission spectrum of the MIM system, show in Figure 2.7. We notice that the presence of the membrane significantly changes the spectrum of the optical cavity. Comparing with the empty cavity, we first see an overall shift in the resonant location and, more interestingly, the fraction of light transmitted changes from mode to mode. It seems that the relative position of the membrane respect to the field changes the effective coupling condition of the cavity. The optomechanical coupling at each resonant mode is shown in Figure 2.8, we see very good agreement between the numerical simulation of G and the approximated analytical expression in Equation 2.81. More interestingly, we see a strong anti-correlation between optomechanical coupling and cavity linewidth. However, because a negative G still means strong interaction, some modes present strong coupling $|G|$ while presenting a narrow linewidth.

Perhaps surprisingly, the finesse of the cavity can be enhanced in the presence of a thin slab. Intuitively, the cavity round-trip might be effectively longer or shorter depending on the probability of reflecting off the membrane, changing the decay rate of intracavity light. By calculating the spatial distribution of the cavity field (shown in the bottom plots of Figure 2.8), we see that in cases where the linewidth of the MIM cavity is narrower than the empty cavity, the strength of the field is concentrated in the long side of the cavity (in the case we have simulated: $L_2 > L_1$). The opposite case is also true. The MIM linewidth is similar to the empty cavity linewidth when G is close to zero and the field concentration at both sides of the membrane is

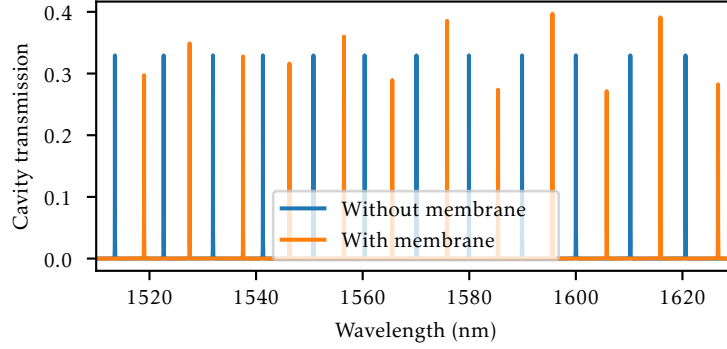


Figure 2.7: Comparison of the power transmission spectrum of a MIM system with (orange) and without a membrane (blue). The $L = 126\ \mu\text{m}$ cavity is pumped through a a mirror of 99% reflectivity and the transmission measured through a 99.9% reflectivity end-mirror. The mirrors have the same reflectivity ratio as our experiment mirrors, but we have lowered the reflectivity for illustration purposes.

similar. This finesse enhancing effect is not due to the asymmetry of the reflectivity coatings, as it is observed for a symmetrically coated cavity too. If the membrane sits perfectly at the center of the cavity, the linewidth is equal to the empty cavity linewidth and G is zero at all resonant wavelengths.

Although the strength of the interaction in a MIM system has a more complex behavior than the canonical moving-end mirror, its nature is the same. We can treat MIM systems in analogous way to the canonical configuration and use the same optomechanical Hamiltonian in Equation 2.75. Generally, the theory that we develop in the following sections applies to all cavity-optomechanics systems dominated by a linear coupling between the cavity frequency and the resonator position.

2.6 The linearized cavity quantum optomechanics equations

The time-evolution of the optical mode can be found using the quantum Langevin equation (Equation 2.60) together with the optomechanical Hamiltonian found above (Equation 2.75). The evolution of the mechanical mode is found using the quantum Langevin equation for the mechanical oscillator (Equation 2.23) and the optomechanical Hamiltonian. The resulting system of coupled differential equations is:

$$\dot{\hat{a}}(t) = -\left(\frac{\kappa}{2} + i\omega_c + i\sqrt{2}g_0\hat{Q}\right)\hat{a}(t) + \sum_{i=1,2,\ell} \sqrt{\kappa_i}\hat{a}_{\text{in},i}(t) \quad (2.84)$$

$$\ddot{\hat{Q}}(t) + \Gamma_m\dot{\hat{Q}}(t) + \Omega_m^2\hat{Q}(t) = \sqrt{2\Gamma_m}\Omega_m\hat{P}_{\text{in}}(t) - \sqrt{2}g_0\Omega_m\hat{a}^\dagger(t)\hat{a}(t). \quad (2.85)$$

We will start by considering that we use a laser of mean frequency ω_l to feed the cavity through mirror 1 (port $i = 1$). Vacuum leaks in through the other mirror (port $i = 2$) and through the loss channels ($i = \ell$). Output port 1 represents the cavity reflection and output port 2 the cavity transmission.

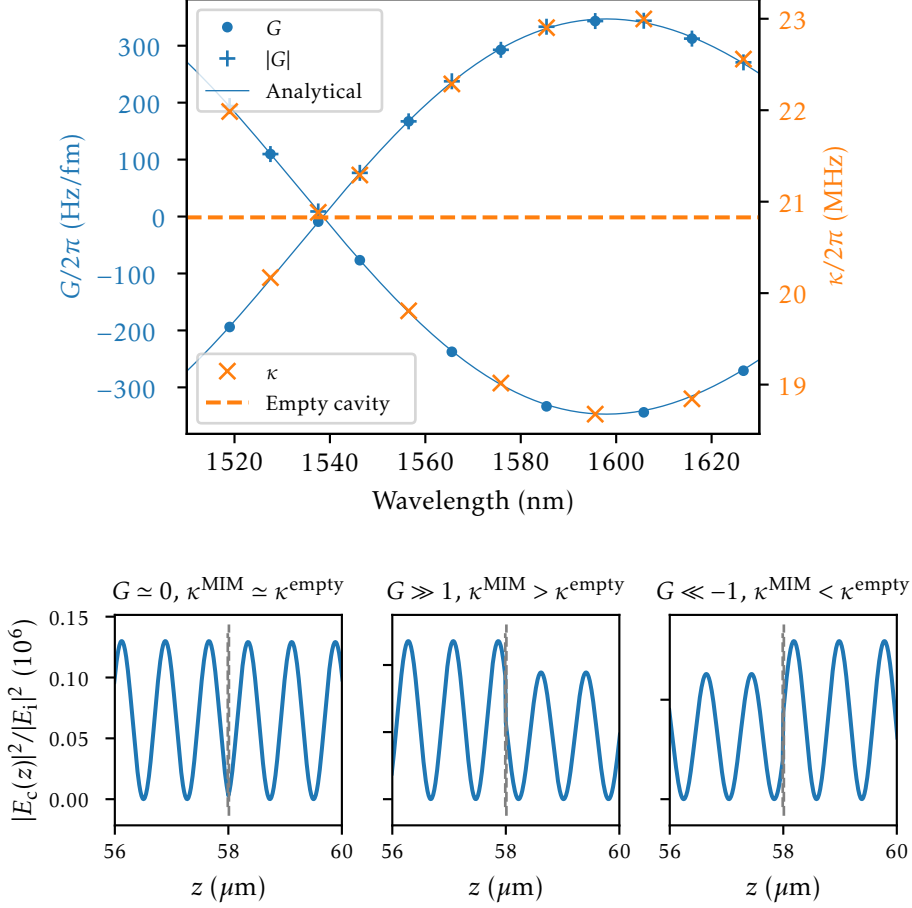


Figure 2.8: Optomechanical coupling and linewidth in a membrane-in-the-middle optomechanical system. **Top plot:** The optomechanical factor G and the cavity linewidth κ are numerically calculated for a MIM system of cavity length $L = L_1 + L_2 = 126 \mu\text{m}$, with a mirror to membrane distance $L_1 = 58 \mu\text{m}$. We observe an anti-correlation between G and κ at the different resonant wavelengths. The solid blue line is the analytical expression for G found in Equation 2.81, the dashed orange line is the empty cavity linewidth calculated from the finesse given by the mirror transmissivities ($\mathcal{T}_1 = 100\text{ppm}$ and $\mathcal{T}_2 = 10\text{ppm}$). **Bottom plots:** Strength of the intracavity field around the membrane at three different resonant wavelengths, illustrating how G and κ depend on the relative position and field concentration asymmetry respectively.

Usually, both the optical and mechanical field have large expectation values compared to the magnitude of their fluctuations. Thus, it is a good approximation to work in a linearized regime where fluctuations are only considered up to linear order. We start the process of linearization by separating all the time-dependent terms into a steady-state constant value and some possibly quantum fluctuations around that value:

$$\hat{a}(t) = \alpha + \delta\hat{a}(t) \quad (2.86a)$$

$$\omega_c(t) = \bar{\omega}_c + \delta\omega_c(t) \quad (2.86b)$$

$$\hat{a}_{\text{in},1}(t) = [\alpha_{\text{in},1} + \delta\hat{a}_{\text{in},1}(t)]e^{-i\omega_l t} \quad (2.86c)$$

$$\hat{a}_{\text{in},2}(t) = \delta\hat{a}_{\text{in},2}(t)e^{-i\omega_l t} \quad (2.86d)$$

$$\hat{a}_{\text{in},\ell}(t) = \delta\hat{a}_{\text{in},\ell}(t)e^{-i\omega_l t} \quad (2.86e)$$

$$\hat{Q}(t) = \bar{Q} + \delta\hat{Q}(t), \quad (2.86f)$$

where we have included time-dependent changes on the cavity resonance ($\delta\omega_c$) due to motion of the mirror and/or low-quality factor mechanical modes. The rotating phase in $\hat{a}_{\text{in},2}$ and $\hat{a}_{\text{in},\ell}$ has been included for convenience, it does not alter the dynamics as both ports are connected to vacuum. We will work in the rotating frame of the laser, so that $\hat{a} \rightarrow \hat{a}e^{-i\omega_l t}$ transforming the Langevin equation to:

$$\dot{\hat{a}}(t) = -\left(\frac{\kappa}{2} - i\bar{\Delta} - i\delta\Delta(t) + i\sqrt{2}g_0\hat{Q}\right)\hat{a}(t) + \sqrt{\kappa_j}\alpha_{\text{in},j} + \sum_{i=1,2,\ell} \sqrt{\kappa_i}\delta\hat{a}_{\text{in},i}(t) \quad (2.87)$$

where we have introduced the average detuning:

$$\bar{\Delta} := \omega_l - \bar{\omega}_c, \quad (2.88)$$

so that $\bar{\Delta} < 0 \Leftrightarrow \omega_l < \omega_c$ is referred to the laser being red-detuned and $\bar{\Delta} > 0 \Leftrightarrow \omega_l > \omega_c$ as blue-detuned. The detuning fluctuations are then:

$$\delta\Delta(t) = -\delta\omega_c(t). \quad (2.89)$$

An important note before proceeding: the expected value of a fluctuation term is not necessarily zero: $\langle \delta\hat{O}(t) \rangle \neq 0$. The separation is done between steady-state and time-dependent fluctuations so that in general $\frac{d\langle \delta\hat{O}(t) \rangle}{dt} \neq 0$.

2.6.1 The steady state

The presence of a mechanically compliant element will modify the steady-state spectrum of the cavity. We define the steady-state values of the cavity field and mechanical position α and \bar{Q} by imposing $\dot{\alpha} = 0$ and $\ddot{Q} = \dot{Q} = 0$ in the absence of fluctuations. We use Equation 2.87 to find:

$$\alpha = \frac{\sqrt{\kappa_1}\alpha_{\text{in},1}}{\frac{\kappa}{2} - i\bar{\Delta} + i\sqrt{2}g_0\bar{Q}} \rightarrow \frac{\sqrt{\kappa_1}\alpha_{\text{in},1}}{\frac{\kappa}{2} - i\bar{\Delta}} \quad (2.90)$$

$$\bar{Q} = -\frac{\sqrt{2}g_0}{\Omega_m}|\alpha|^2, \quad (2.91)$$

where the detuning can be redefined to take into account the steady change of the cavity resonance due to the new equilibrium position of the resonator. If we don't perform the redefinition,

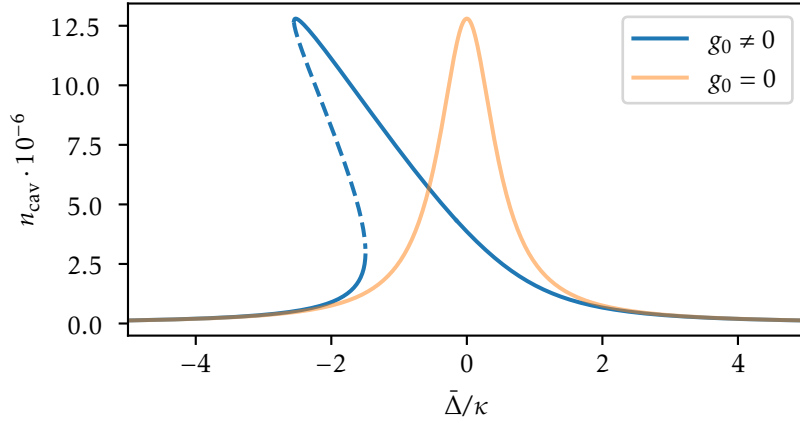


Figure 2.9: Optomechanical bistability: optomechanical interaction changes the expected number of cavity photons from a Lorentzian shape to a shark-fin like shape. When scanning a laser from negative to positive detuning, we will observe the transmitted power jump from the bottom solid line to the top solid line, skipping the dashed solutions. n_c has been solved numerically with parameters: $\Omega_m = 2\pi \cdot 1.14\text{MHz}$, $\kappa = 2\pi \cdot 20\text{MHz}$, $\kappa_1 = 10\kappa/11$, $P_{\text{in},1} = 567\text{nW}$, $\lambda = 1550\text{nm}$, $g_0 = 2\pi \cdot 1.5\text{kHz}$. For comparison, the intracavity photon number of an empty cavity has been plotted in faint orange, notice that, in the ideal case that the membrane does not induce losses, the maximum intracavity power is the same.

the above equations form a third-degree equation for α , thus, three possible solutions for α exist at a given $\bar{\Delta}$. This is the origin of the *optomechanical bistability*.

We can write the equation for the intracavity photon number $n_c = |\alpha|^2$ and solve as a function of detuning Δ :

$$n_c \left(\frac{\kappa^2}{4} + \left(\bar{\Delta} + \frac{2g_0^2}{\Omega_m} n_c \right)^2 \right) = \kappa_1 \dot{n}_{in,1}, \quad (2.92)$$

this equation has either one or three solutions depending on parameters. For small detunings, three solutions exist for high enough interaction, resulting in a resonance shape distinct from a Lorentzian, as it can be seen in Figure 2.9.

2.6.2 The fluctuation dynamics

In our linearized picture, the fluctuation terms contain the dynamics of the system. To obtain the differential equations for the fluctuations, we insert the definitions in Equation 2.86 in the Langevin equations for the cavity mode (Equation 2.87) and for the mechanical mode (Equation 2.85):

$$\delta \dot{\hat{a}}(t) = -\left(\frac{\kappa}{2} - i\bar{\Delta}\right) \delta \hat{a}(t) + i\alpha \delta \Delta(t) - i\sqrt{2}g \delta \hat{Q}(t) + \sum_{i=1,2,\ell} \sqrt{\kappa_i} \delta \hat{a}_{in,i}(t) \quad (2.93)$$

$$\delta \ddot{\hat{Q}}(t) + \Gamma_m \delta \dot{\hat{Q}}(t) + \Omega_m^2 \delta \hat{Q}(t) = \sqrt{2\Gamma_m} \Omega_m \hat{P}_{in}(t) - \sqrt{2}g \Omega_m (\delta \hat{a}(t) + \delta \hat{a}^\dagger(t)), \quad (2.94)$$

where we have used that the steady-state intracavity field α is real, we have defined the *light-enhanced optomechanical coupling rate* $g = g_0 \alpha = g_0 \sqrt{n_c}$ and we have approximated away second order fluctuation terms ($\delta \dots \cdot \delta \dots$). Thanks to the linearization, we now have a linear system of ordinary differential equations that can be solved straightforwardly in frequency space by taking the Fourier transform³:

$$\delta \hat{a}(\omega) = \chi_c(\omega) \left[i\alpha \delta \Delta(\omega) - i\sqrt{2}g \delta \hat{Q}(\omega) + \sum_{i=1,2,\ell} \sqrt{\kappa_i} \delta \hat{a}_{in,i}(\omega) \right], \quad (2.95)$$

$$\delta \hat{a}^\dagger(\omega) = \chi_c^*(-\omega) \left[-i\alpha \delta \Delta(\omega) + i\sqrt{2}g \delta \hat{Q}(\omega) + \sum_{i=1,2,\ell} \sqrt{\kappa_i} \delta \hat{a}_{in,i}^\dagger(\omega) \right], \quad (2.96)$$

$$\delta \hat{Q}(\omega) = \chi_m(\omega) \left[\sqrt{2\Gamma_m} \hat{P}_{in}(\omega) - \sqrt{2}g (\delta \hat{a}(\omega) + \delta \hat{a}^\dagger(\omega)) \right] \quad (2.97)$$

With optical susceptibility:

$$\chi_c(\omega) := \frac{1}{\kappa/2 - i\bar{\Delta} - i\omega}, \quad (2.98)$$

and mechanical susceptibility:

$$\chi_m(\omega) := \frac{\Omega_m}{\Omega_m^2 - \omega^2 - i\omega\Gamma_m}. \quad (2.99)$$

These are the same susceptibilities for a bare cavity and a bare mechanical oscillator. The expression for $\delta \hat{a}^\dagger(\omega)$ has been found applying the Hermitian conjugate prior to the Fourier transform. As expected from the non-linearized model, the position of the mechanical oscillator is sensitive to the intra-cavity field amplitude (through $\delta \hat{X} \propto \delta \hat{a}(\omega) + \delta \hat{a}^\dagger(\omega)$) but not its phase.

³Defined as $\hat{A}(\omega) = \mathcal{F}\{\hat{A}(t)\}(\omega) = \int_{-\infty}^{\infty} e^{i\omega t} \hat{A}(t) dt$ and using the notation $\hat{A}^\dagger(\omega) = \mathcal{F}\left\{\left[\hat{A}(t)\right]^\dagger\right\}(\omega)$. More details on the conventions used can be found in Appendix C

2.6.3 Dynamical backaction

It is obvious that the mechanical oscillator will behave differently when it is part of a populated optical cavity. Consider the effect of a small displacement of the oscillator. If $\bar{\Delta} \neq 0$, the displacement changes the cavity's resonant frequency, which in turn causes an increase or decrease of the cavity field as the pumping laser becomes less or more detuned. This results in a radiation pressure force that depends on position, effectively changing the spring constant of the resonator. The subsequent change in observed frequency is known as the *optical spring effect*. Furthermore, a small resonator displacement also affects the phase of the cavity field. The phase of the field does not directly couple to the resonator, but, as the intracavity field rotates at $\bar{\Delta}$, a change in phase will eventually convert into an amplitude change. The result is a time-delayed position-dependent force that can damp the oscillator when $\bar{\Delta} < 0$, or excite the oscillator when $\bar{\Delta} > 0$, having no effect when $\bar{\Delta} = 0$.

The optical spring effect and the modified damping rate are often referred to as *dynamical backaction* and are modeled by the previously found Langevin equations. In order to do so, we will first obtain an expression for $\delta\hat{Q}(\omega)$ as a function of the input fluctuation operators $\delta\hat{P}_{\text{in}}$, $\delta\hat{a}_{\text{in},i}(\omega)$ and $\delta\hat{a}_{\text{in},i}^\dagger(\omega)$. This is done by directly inserting the field fluctuations found in Equation 2.95 and Equation 2.96 into Equation 2.97:

$$\begin{aligned} \delta\hat{Q}(\omega) = \chi_{m,\text{opt}}(\omega) & \left\{ \sqrt{2\Gamma_m} \hat{P}_{\text{in}}(\omega) \right. \\ & + \sqrt{2}g\alpha[\chi_c^*(-\omega) - \chi_c(\omega)]\delta\Delta(\omega) \\ & \left. - \sqrt{2}g \sum_{i=1,2,\ell} \sqrt{\kappa_i} [\chi_c^*(-\omega)\delta\hat{a}_{\text{in},i}^\dagger(\omega) + \chi_c(\omega)\delta\hat{a}_{\text{in},i}(\omega)] \right\}, \end{aligned} \quad (2.100)$$

where we have introduced the modified mechanical susceptibility $\chi_{m,\text{opt}}(\omega)$:

$$\chi_{m,\text{opt}}^{-1}(\omega) = \chi_m^{-1}(\omega) + \frac{4g^2\bar{\Delta}}{\left(\frac{\kappa}{2} - i\omega\right)^2 + \bar{\Delta}^2}. \quad (2.101)$$

In the picture of the modified mechanical susceptibility, we have removed dependency on the intracavity field values. The effective forces acting on the mechanical oscillator are: the fluctuations of its thermal bath \hat{P}_{in} , fluctuations in the cavity detuning $\delta\Delta$ and fluctuations in the input fields $\delta\hat{a}_{\text{in},i}$. As expected from our previous discussion, in the resonant case $\bar{\Delta} = 0$, dynamical backaction disappears and the modified susceptibility becomes the regular mechanical susceptibility.

The modified susceptibility $\chi_{m,\text{opt}}(\omega)$ is generally not Lorentzian-shaped. It will even become doubled-peaked in the strong-coupling regime $g \gg \kappa, \Omega_m$ [25]. Outside the strong-coupling regime, we can consider that the modified optical susceptibility maintains its Lorentzian shape but with a frequency change $\delta\Omega_m$ due to the spring effect and additional damping/anti-damping $\delta\Gamma_m$. Inserting these increments into the definition of the mechanical susceptibility (Equation 2.99) and comparison to the formula for the modified susceptibility (Equation 2.101), we obtain the following relations:

$$\delta\Omega_m(\omega) = \frac{1}{2} \text{Re} \left\{ \frac{4g^2\bar{\Delta}}{\left(\frac{\kappa}{2} - i\omega\right)^2 + \bar{\Delta}^2} \right\} \quad (2.102)$$

$$\delta\Gamma_m(\omega) = -\frac{\Omega_m}{\omega} \text{Im} \left\{ \frac{4g^2\bar{\Delta}}{\left(\frac{\kappa}{2} - i\omega\right)^2 + \bar{\Delta}^2} \right\}, \quad (2.103)$$

where we have considered $\delta\Omega_m \ll \Omega_m$. Around the mechanical frequency ($\omega \simeq \Omega_m$) and in the side-band unresolved regime $\Omega_m \ll \kappa$, the expressions take the form:

$$\delta\Omega_m \simeq g^2 \frac{2\Delta}{\frac{\kappa^2}{4} + \Delta^2}. \quad (2.104)$$

$$\delta\Gamma_m := \Gamma_m^{\text{opt}} \simeq -g^2 \Omega_m \frac{4\Delta\kappa}{\left(\frac{\kappa^2}{4} + \Delta^2\right)^2}. \quad (2.105)$$

More general expressions can be found in [25].

The total effective damping rate of the resonator is thus:

$$\Gamma_{\text{eff}} = \Gamma_m + \Gamma_m^{\text{opt}} \quad (2.106)$$

which might become negative when $\bar{\Delta} > 0$. The antidamping manifests as exponentially growing mechanical oscillations when the laser is blue-detuned. The phenomenon, often referred to as *self-induced oscillations* or *phonon lasing*, cannot be fully understood in our linearized approach as the small fluctuation approximation quickly breaks down.

2.6.4 Optical fluctuations

The mechanical compliance of our optical cavity strongly alters its behavior. Not only will the mechanical fluctuations be imprinted in the optical field, correlations between the amplitude and phase of the light can arise mediated by the mechanical resonator. We will first look at the intracavity field and then derive the output fields, the ones that we can measure.

We will solve the Fourier-space equations of operators $\delta\hat{a}, \delta\hat{a}^\dagger$ and $\delta\hat{Q}$ (Equation 2.95, Equation 2.96 and Equation 2.97) using matrices. First, we define a forcing vector that includes all the fluctuation sources:

$$\hat{f}(\omega) := \begin{pmatrix} \delta\hat{a}_{\text{in},1}(\omega) \\ \delta\hat{a}_{\text{in},1}^\dagger(\omega) \\ \delta\hat{a}_{\text{in},2}(\omega) \\ \delta\hat{a}_{\text{in},2}^\dagger(\omega) \\ \delta\hat{a}_{\text{in},\ell}(\omega) \\ \delta\hat{a}_{\text{in},\ell}^\dagger(\omega) \\ \delta\Delta(\omega) \\ \hat{P}_{\text{in}}(\omega) \end{pmatrix} \quad (2.107)$$

We can write the positon fluctutations (Equation 2.97) in vector dot-product form:

$$\delta\hat{Q} = [\chi_Q(\omega)]^\top \cdot \hat{f}, \quad (2.108)$$

where $(\dots)^\top$ indicates the tranpose matrix and:

$$\chi_Q(\omega) := \sqrt{2}g\chi_{m,\text{opt}}(\omega) \begin{pmatrix} -\sqrt{\kappa_1}\chi_c(\omega) \\ -\sqrt{\kappa_1}\chi_c^*(-\omega) \\ -\sqrt{\kappa_2}\chi_c(\omega) \\ -\sqrt{\kappa_2}\chi_c^*(-\omega) \\ -\sqrt{\kappa_\ell}\chi_c(\omega) \\ -\sqrt{\kappa_\ell}\chi_c^*(-\omega) \\ i\alpha[\chi_c^*(-\omega) - \chi_c(\omega)] \\ \sqrt{\Gamma_m} \end{pmatrix}. \quad (2.109)$$

Similarly, we can rewrite the cavity field fluctuations in matrix form:

$$\begin{pmatrix} \delta \hat{a}(\omega) \\ \delta \hat{a}^\dagger(\omega) \end{pmatrix} = \mathbf{\Lambda}_a(\omega) \cdot \hat{\mathbf{f}}(\omega) \quad (2.110)$$

where $\mathbf{\Lambda}_a(\omega)$ is a 2×8 matrix defined as:

$$\mathbf{\Lambda}_a(\omega) := \mathbf{\Lambda}'_a(\omega) - i\sqrt{2}g \begin{pmatrix} \chi_c(\omega) [\chi_Q(\omega)]^\top \\ -\chi_c^*(-\omega) [\chi_Q(\omega)]^\top \end{pmatrix} \quad (2.111)$$

$$\mathbf{\Lambda}'_a := \begin{pmatrix} \sqrt{\kappa_1} \chi_c(\omega) & 0 & \sqrt{\kappa_2} \chi_c(\omega) & 0 & \sqrt{\kappa_\ell} \chi_c(\omega) & 0 & i\chi_c(\omega)\alpha & 0 \\ 0 & \sqrt{\kappa_1} \chi_c^*(-\omega) & 0 & \sqrt{\kappa_2} \chi_c^*(-\omega) & 0 & \sqrt{\kappa_\ell} \chi_c^*(-\omega) & -i\chi_c^*(-\omega)\alpha & 0 \end{pmatrix} \quad (2.112)$$

Now that we have solved for the intracavity fields, we can find the output fields. The input-output relations in matrix form are:

$$\delta \hat{\mathbf{a}}_{\text{out}}(\omega) := \begin{pmatrix} \delta \hat{a}_{\text{out},1}(\omega) \\ \delta \hat{a}_{\text{out},1}^\dagger(\omega) \\ \delta \hat{a}_{\text{out},2}(\omega) \\ \delta \hat{a}_{\text{out},2}^\dagger(\omega) \\ \delta \hat{a}_{\text{out},\ell}(\omega) \\ \delta \hat{a}_{\text{out},\ell}^\dagger(\omega) \\ 0 \\ 0 \end{pmatrix} = \begin{pmatrix} \mathbb{I}_{6 \times 6} & & \\ & 0 & 0 \\ & 0 & 0 \end{pmatrix} \cdot \hat{\mathbf{f}}(\omega) - \underbrace{\begin{pmatrix} \sqrt{\kappa_1} & 0 \\ 0 & \sqrt{\kappa_1} \\ \sqrt{\kappa_2} & 0 \\ 0 & \sqrt{\kappa_2} \\ \sqrt{\kappa_\ell} & 0 \\ 0 & \sqrt{\kappa_\ell} \\ 0 & 0 \\ 0 & 0 \end{pmatrix}}_{:=\mathcal{K}} \cdot \begin{pmatrix} \delta \hat{a}(\omega) \\ \delta \hat{a}^\dagger(\omega) \end{pmatrix}, \quad (2.113)$$

where the vector $\hat{\mathbf{a}}_{\text{out}}$ has been padded with zeros so that it matches the dimensions of $\hat{\mathbf{f}}$. Finally, we can write the outputs as a linear transform of the inputs by inserting Equation 2.110:

$$\delta \hat{\mathbf{a}}_{\text{out}}(\omega) = \mathbf{\Lambda}(\omega) \cdot \hat{\mathbf{f}}(\omega), \quad (2.114)$$

where:

$$\mathbf{\Lambda}(\omega) := \begin{pmatrix} \mathbb{I}_{6 \times 6} & & \\ & 0 & 0 \\ & 0 & 0 \end{pmatrix} - \mathcal{K} \cdot \mathbf{\Lambda}_a(\omega). \quad (2.115)$$

It will be convenient for the next sections to find the fluctuations of the output quadratures. Using the definitions of quadratures fluctuations found in Equation B.2, we write in matrix form:

$$\delta \hat{\mathbf{X}}_{\text{out}}(\omega) := \begin{pmatrix} \delta \hat{X}_{\text{out},1}(\omega) \\ \delta \hat{Y}_{\text{out},1}(\omega) \\ \delta \hat{X}_{\text{out},2}(\omega) \\ \delta \hat{Y}_{\text{out},2}(\omega) \\ \delta \hat{X}_{\text{out},\ell}(\omega) \\ \delta \hat{Y}_{\text{out},\ell}(\omega) \\ 0 \\ 0 \end{pmatrix} = \mathbf{C}(\Delta) \cdot \delta \hat{\mathbf{a}}_{\text{out}}(\omega) = \underbrace{\mathbf{C}(\Delta) \mathbf{\Lambda}(\omega)}_{\mathbf{\Lambda}_X(\omega)} \cdot \hat{\mathbf{f}}(\omega) \quad (2.116)$$

where we have considered the sideband unresolved regime $\Omega_m \ll \kappa$.⁶ The symmetrized thermal force expressed in a similar manner is [33]:

$$\bar{S}_{F_{\text{th}}F_{\text{th}}}(\Omega_m) = \frac{\hbar^2}{x_{\text{z.p.}}^2} \Gamma_m n_{\text{th}}. \quad (2.127)$$

The ratio of the forces is then:

$$\frac{\bar{S}_{\hat{F}_{\text{opt}}\hat{F}_{\text{opt}}}(\Omega_m)}{\bar{S}_{F_{\text{th}}F_{\text{th}}}(\Omega_m)} = C_q \cdot \frac{1}{1 + \frac{4\Delta^2}{\kappa^2}}, \quad (2.128)$$

where we have introduced the commonly used *quantum cooperativity*:

$$C_q = \frac{4g^2}{\kappa\Gamma_m n_{\text{th}}} = \frac{C}{n_{\text{th}}}, \quad (2.129)$$

where C is the cooperativity introduced previously. Thus, our criterion for quantum dominated optomechanical interaction is:

$$C_q \geq 1 + \frac{4\Delta^2}{\kappa^2} \quad (2.130)$$

when the laser is close to resonance:

$$C_q \gtrsim 1. \quad (2.131)$$

In order to briefly and qualitatively discuss optomechanical squeezing, we calculate the PSDs of the output quadratures numerically. We do this by inserting Equation 2.116 in Equation 2.120:

$$\mathcal{S}_{\hat{X}_{\text{out}}}(\omega) = [\mathbf{\Lambda}_X(\omega)]^* \cdot \mathcal{S}_f(\omega) \cdot [\mathbf{\Lambda}_X(\omega)]^T \quad (2.132)$$

In Figure 2.10, we see the PSD of different quadratures of the reflected and transmitted beam normalized to shot-noise⁷. We see how, in a high quantum cooperativity situation, optomechanical squeezing appears in the left or right side of the mechanical signal peak, depending on the quadrature measured. From the simulations, we see that the quadrature that presents maximum squeezing depends on the detuning $\bar{\Delta}$ as well as if we are considering the reflected or the transmitted beam.

2.7 Detection schemes

In this section, we describe two different light detection schemes in the context of cavity optomechanics. We will start with the simplest: direct detection, then move to phase referenced detection: the balanced homodyne detector. A description of unbalanced (single-detector) homodyne can be found in Appendix D. We will not describe heterodyne detection, which is a very important measuring scheme as it allows for the measurement of the negative frequency region of the PSD, which is solid evidence of quantum behavior. We refer the reader to [33] for a treatment of heterodyne detection in the context of cavity optomechanics.

⁶To obtain Equation 2.126, expand the intracavity field into steady state and fluctuations $\hat{a}^\dagger \hat{a} \simeq \alpha^2 + \alpha(\delta\hat{a}^\dagger + \delta\hat{a})$, use the Fourier space equations for $\delta\hat{a}, \delta\hat{a}^\dagger$ (Equation 2.95 and Equation 2.96) neglecting the effect of the mechanics to obtain the PSD of $\hat{a}^\dagger \hat{a}$

⁷The PSD of an arbitrary quadrature can be found using Equation C.13: $S_{\hat{X}\hat{X}}\psi = S_{\hat{X}\hat{X}}\cos^2\psi + S_{\hat{Y}\hat{Y}}\sin^2\psi + 2\cos\psi\sin\psi\text{Re}\{S_{\hat{X}\hat{Y}}\}$

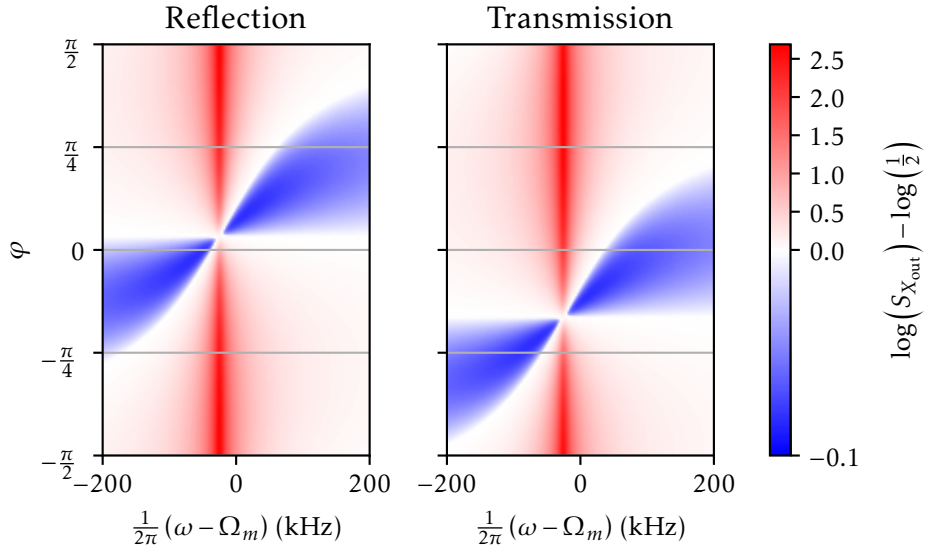


Figure 2.10: Power spectral density of an arbitrary quadrature \hat{X}^φ of the reflected and transmitted field. Note the asymmetric color bar. Blue regions present squeezing, white represents fluctuations associated with a coherent beam and red above that (they contain mechanical signal). The plots have been obtained using Equation 2.149, with $\Omega_m = 2\pi \cdot 1.14\text{MHz}$, $Q = 10^8$, $\kappa = 2\pi \cdot 20\text{MHz}$ and an input power resulting in $C_q = 1.75$ at a detuning of $\bar{\Delta} = \frac{\kappa}{2\sqrt{3}}$. The simulation is done at room-temperature with no additional detuning or classical laser noise ($S_{\Delta\Delta} = 0$, and $S_{\hat{X}_{\text{in}}\hat{X}_{\text{in}}} = S_{\hat{Y}_{\text{in}}\hat{Y}_{\text{in}}} = \frac{1}{2}$, $S_{\hat{X}_{\text{in}}\hat{Y}_{\text{in}}} = \frac{i}{2}$)

2.7.1 Direct detection

In *direct detection*, our beam of interest is directly sent to a photodiode. In our fluctuation picture, the photocurrent \hat{i} is given by the amplitude quadrature:

$$\hat{i} = |\hat{a}|^2 \simeq |\alpha|^2 + \sqrt{2}|\alpha|\delta\hat{X}, \quad (2.133)$$

the signal fluctuates around a large DC component. What we record in an oscilloscope or spectrum analyzer is a classical stochastic variable i , the result of the non-reversible measurement of \hat{i} in the photodetection process [33]. A result of Glauber's theory of photodetection is that the PSD of i is actually related to the symmetrized PSD of \hat{i} , fulfilling that the PSD of a real stochastic variable must be symmetric. In the linearized approximation:

$$S_{ii}(\omega) \simeq \bar{S}_{\hat{i}\hat{i}}(\omega) := \frac{S_{\hat{i}\hat{i}}(\omega) + S_{\hat{i}\hat{i}}(-\omega)}{2}. \quad (2.134)$$

It is thus straight-forward to find the spectrum of direct detection of the output fields of the cavity. Equation 2.149 can be used to find an expression for $\bar{S}_{\hat{X}\hat{X}}$ to obtain:

$$S_{ii}(\omega) = 2|\alpha_{\text{det}}|^2 \bar{S}_{\hat{X}_{\text{det}}\hat{X}_{\text{det}}}(\omega). \quad (2.135)$$

To model inefficiencies in the detection scheme, we model the losses as a beamsplitter of transmission η , where we have lumped together both the collection of light from the system and the quantum efficiency of the detector.

$$S_{ii}(\omega) = 2\eta|\alpha_{\text{out}}|^2 \left[\frac{1-\eta}{2} + \eta \bar{S}_{\hat{X}_{\text{out}}\hat{X}_{\text{out}}}(\omega) \right]. \quad (2.136)$$

Due to direct detection being sensitive only to amplitude, it can only perform linear measurement of the mechanical motion when the cavity is driven at a $\Delta \neq 0$ detuning. Despite this limitation, direct detection can allow for measurement of optomechanical squeezing as it usually is optimal close to the amplitude quadrature. This is demonstrated in Figure 2.11. The equation above shows how losses in the measurement can easily remove any trace of squeezing, pulling the fluctuations back towards the shot-noise level of $\frac{1}{2}$.

2.7.2 Balanced Homodyne Detection

The Balanced Homodyne Detector (BHD) is the most commonly used interferometric detection scheme in quantum optics. A BHD consists in mixing a signal with a strong local oscillator (LO) in a 50:50 beamsplitter. The two outputs are measured in two photodiodes in subtractive mode. The signal of the BHD is proportional to the quadrature of the signal given by the relative phase between the signal and the LO. Due to the subtraction of the two photocurrents, the BHD is immune to classical amplitude noise of the LO. The mathematical description of the BHD that one finds in the literature usually assumes a quantum-limited laser source, but as mentioned earlier, the phase noise of most real lasers is well above quantum fluctuations. In this section, we will consider the effects of a noisy laser.

Before proceeding to deal with a noisy laser, let us look at the standard approach to the BHD. The signal beam \hat{a}_s and the LO beam \hat{a}_{LO} enter at different ports of a 50:50 beamsplitter. The output fields \hat{a}_+ and \hat{a}_- are given by:

$$\hat{a}_{\pm} = \frac{1}{\sqrt{2}}(\hat{a}_{\text{LO}} \pm \hat{a}_s), \quad (2.137)$$

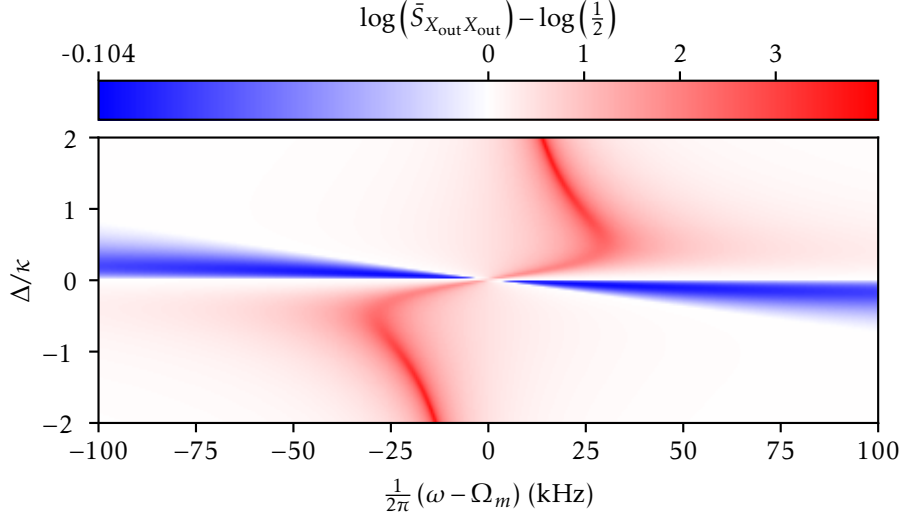


Figure 2.11: Symmetrized power spectral density of the amplitude quadrature \hat{X} of the transmitted field at different detunings, which is directly proportional to the one detected in direct detection. Note the asymmetric color bar. Blue regions present squeezing, white regions have coherent beam fluctuations and red contain mechanical signal. The plots have been obtained using Equation 2.149, with $\Omega_m = 2\pi \cdot 1.14\text{MHz}$, $Q = 10^8$, $\kappa = 2\pi \cdot 20\text{MHz}$ and an input power resulting in $C_q = 1.75$ at a detuning of $\bar{\Delta} = \frac{\kappa}{2\sqrt{3}}$. The simulation is done at room-temperature with no additional detuning noise or classical laser noise ($S_{\Delta\Delta} = 0$, and $S_{\hat{X}_{\text{in}}\hat{X}_{\text{in}}} = S_{\hat{Y}_{\text{in}}\hat{Y}_{\text{in}}} = \frac{1}{2}$, $S_{\hat{X}_{\text{in}}\hat{Y}_{\text{in}}} = \frac{i}{2}$)

creating the photocurrents:

$$\hat{i}_{\pm} = |\hat{a}_{\pm}|^2 = \frac{1}{2} \left(|\hat{a}_{\text{LO}}|^2 + |\hat{a}_s|^2 \pm \hat{a}_{\text{LO}}^{\dagger} \hat{a}_s \pm \hat{a}_{\text{LO}} \hat{a}_s^{\dagger} \right). \quad (2.138)$$

We linearize the expression by splitting both beams into field and fluctuations $\hat{a}_{\text{LO}} = \alpha_{\text{LO}} + \delta\hat{a}_{\text{LO}}$, $\hat{a}_s = \alpha_s + \delta\hat{a}_s$, and writing in terms of quadratures:

$$\begin{aligned} \hat{i}_{\pm} = & \underbrace{\frac{|\alpha_{\text{LO}}|^2}{2} \pm \frac{|\alpha_s|^2}{2} \pm |\alpha_{\text{LO}}|\alpha_s \cos(\theta_{\text{LO}} - \theta_s)}_{i_{\pm\text{DC}}} + \underbrace{\frac{1}{\sqrt{2}}|\alpha_s|\delta\hat{X}_s + \frac{1}{\sqrt{2}}|\alpha_{\text{LO}}|\delta\hat{X}_{\text{LO}}}_{\text{Direct detection of amplitude fluctuations}} + \\ & \pm \underbrace{\frac{1}{\sqrt{2}}|\alpha_{\text{LO}}|\delta\hat{X}_s^{\theta_{\text{LO}} - \theta_s}}_{\text{LO projects signal quadratures}} \pm \underbrace{\frac{1}{\sqrt{2}}|\alpha_s|\delta\hat{X}_{\text{LO}}^{\theta_s - \theta_s}}_{\text{Signal projects LO quadratures}} + \\ & \underbrace{\frac{|\delta\hat{a}_{\text{LO}}|^2}{2} + \frac{|\delta\hat{a}_s|^2}{2} \pm \frac{1}{2}(\delta\hat{a}_s^{\dagger}\delta\hat{a}_{\text{LO}} + \delta\hat{a}_{\text{LO}}^{\dagger}\delta\hat{a}_s)}_{\text{Second order}} \end{aligned} \quad (2.139)$$

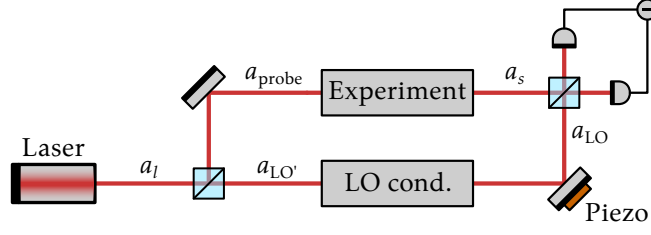


Figure 2.12: General scheme for balanced homodyne detection. Both the local oscillator and probe beams are sourced from the same laser.

The common approximations done to model quantum optics experiments starts by discarding second order fluctuations terms. Then, assuming the the LO has a power much larger than that of the signal, $|\alpha_{\text{LO}}| \gg |\alpha_s|$, we discard terms that depend exclusively on $|\alpha_s|$. The next simplification usually follows from considering the LO a classical coherent beam $\hat{a}_{\text{LO}} \simeq \alpha_{\text{LO}}$, this seems reasonable from the point of view of the steady-state/fluctuation split⁸. In this case, we have a DC component

$$i_{\text{DC}} = 2|\alpha_{\text{LO}}||\alpha_s| \cos(\theta_{\text{LO}} - \theta_s), \quad (2.140)$$

that we can use to lock the phase between the LO and the signal, and the fluctuation of the fictitious photocurrent difference operator:

$$\hat{i} = \sqrt{2}|\alpha_{\text{LO}}|\delta\hat{X}_s^\psi \quad (2.141)$$

$$\psi := \theta_{\text{LO}} - \theta_s. \quad (2.142)$$

This expression is valid for an ideal experiment, in practice there are technical limitations. To start with, the alignment between the LO and the signal beam is never perfect, manifesting in a reduced contrast of the interference fringes. The parameter that measures the contrast is the *visibility* $\text{VIS} = \frac{i_{\text{max}} - i_{\text{min}}}{i_{\text{max}} + i_{\text{min}}}$, which is generally lower than the visibility with perfect alignment $\text{VIS}_{\text{perfect}} = \frac{2\sqrt{i_{\text{LO}}i_s}}{i_{\text{LO}} + i_s}$. The visibility factor $\mathcal{V} = \frac{\text{VIS}}{\text{VIS}_{\text{perfect}}} \in [0, 1]$ is the fraction of the LO that the signal actually interferes with [47]. The second imperfection is the limited *quantum efficiency* η_d of the photodiodes used, which is the fraction of photons reaching the photodiode that are converted to electrons. As we did with direct detection, we can model the limited η_{QE} by considering a beam-splitter of field transmission η_{QE} in front of an ideal detector. We consider that both detectors have the same quantum efficiency. The final expression for the PSD of the homodyne signal is [48, 49]:

$$\bar{S}_{ii}(\omega) = 2\eta_{\text{QE}}|\alpha_{\text{LO}}|^2 \left[\frac{1 - \eta_{\text{det}}}{2} + \eta_{\text{det}} \bar{S}_{\delta\hat{X}_s^\psi \delta\hat{X}_s^\psi}(\omega) \right], \quad (2.143)$$

where similar to direct detection, the PSDs of classical signals must be symmetric. $\eta = \eta_{\text{QE}}\mathcal{V}^2$ combines the two inefficiencies.

We now have a model for BHD with a coherent LO, but it does not include any contribution of classical laser noise. Most experiments use the same laser to generate an LO and a probe

⁸However, the terms $|\alpha_{\text{LO}}|\delta\hat{X}_{\text{LO}}$ appearing in the photocurrent are of the same order of the terms sensitive to our signal $|\alpha_{\text{LO}}|\delta\hat{X}_s$, thus discarding the LO fluctuations while keeping the signal fluctuations is not justified. This debate is related to two different pictures about homodyne detection: when we block the signal field, the fluctuations observed are due to the vacuum fluctuations[45] or due to the actual shotnoise of the LO[46], which is the formulation that I used. In the lab, we just calibrate our spectrum by considering the first point of view.

beam that interacts with a system. The output of that system will be our signal, which rejoins the LO at the BHD, like shown in figure Figure 2.12. Therefore, we need to model the whole experiment to understand the classical correlations between the signal and local oscillator.

We can consider the quantum and classical fluctuations separately due to the linear approximation, in other words, we can write:

$$\hat{i}_{\pm} = \hat{i}_{\pm,q} + \tilde{i}_{\pm,c}, \quad (2.144)$$

where $\hat{i}_{\pm,q}$ includes all terms depending on quantum fluctuations and $\tilde{i}_{\pm,c}$ contains exclusively classical noise. Additionally, it is safe to assume that the classical and quantum noise are uncorrelated, in that case:

$$\bar{S}_{ii}^{\hat{i}}(\omega) = \bar{S}_{i_q i_q}^{\hat{i}}(\omega) + \bar{S}_{i_c i_c}(\omega). \quad (2.145)$$

This result is convenient for calculating the measurement record of our optomechanical system with a BHD. First, we have to split our probe beam into quantum fluctuations and classical phase noise. We only consider phase noise as it is the most persistent noise in commonly used lasers⁹. Our probe beam inherits the phase noise $\delta\phi(t)$ of our laser:

$$\hat{a}_{\text{probe}}(t) = \alpha_{\text{probe}} + i\alpha_{\text{probe}}\delta\phi(t). \quad (2.146)$$

In the convention used in the previous section, the probe enters through port 1 of the cavity. Thus the input/forcing vector $\hat{f}(\omega)$ is:

$$\hat{f}(\omega) = \hat{f}_q(\omega) + \tilde{f}_c(\omega) = \begin{pmatrix} \delta\hat{a}_{\text{in},1}(\omega) \\ \delta\hat{a}_{\text{in},1}^{\dagger}(\omega) \\ \delta\hat{a}_{\text{in},2}(\omega) \\ \delta\hat{a}_{\text{in},2}^{\dagger}(\omega) \\ \delta\hat{a}_{\text{in},\ell}(\omega) \\ \delta\hat{a}_{\text{in},\ell}^{\dagger}(\omega) \\ \delta\Delta(\omega) \\ \hat{P}_{\text{in}}(\omega) \end{pmatrix} + \begin{pmatrix} i\alpha_{\text{probe}}\delta\phi(\omega) \\ -i\alpha_{\text{probe}}^*\delta\phi(\omega) \\ 0 \\ 0 \\ 0 \\ 0 \\ 0 \\ 0 \end{pmatrix}. \quad (2.147)$$

We have split \hat{f} into a quantum and a classical contribution. The subscript c can also stand for “correlated”, because the key advantage of this separation is that \hat{f}_q is not correlated with the LO, while \tilde{f}_c is. Using Equation 2.116, we can find the output fluctuations as a function of \hat{f} . Instead of considering the output beam is the BHD signal, we will account for loss before the cavity output reaches the BHD. This is done by mixing the output field with vacuum at a beamsplitter of transmission η :

$$\delta\hat{X}_s(\omega) = \sqrt{\eta}\delta\hat{X}_{\text{out}}(\omega) + \sqrt{1-\eta}\delta\hat{X}_v, \quad (2.148)$$

where \hat{v} is a column vector of vacuum fluctuations.

It is now straight-forward to find the quantum part of the BHD signal $\bar{S}_{i_q i_q}^{\hat{i}}(\omega)$. First, we find the PSD matrix of the output quadratures:

$$\mathcal{S}_{\delta\hat{X}_{\text{out},q}^{\psi}}(\omega) = [\Lambda_{X\psi}(\omega)]^* \cdot \mathcal{S}_{\hat{f}_q}(\omega) \cdot [\Lambda_{X\psi}(\omega)]^{\text{T}} \quad (2.149)$$

⁹A lot of lasers, in particular fiber lasers, contain a higher degree of classical amplitude noise than phase noise. Amplitude noise can be reduced close to the shot noise using a feedback system (usually referred to as a noise eater), an example can be found in [50] or being used in a cavity optomechanics experiment [43]. Similar approaches can be used to remove phase noise [51], we will discuss phase noise in more detail in Section 6.3

now we use this expressions to find the BHD signal:

$$\delta\tilde{i}_c = \sqrt{2}\eta_{\text{QE}}\mathcal{V}\sqrt{\eta}|\alpha_{\text{LO}}|\left\{\left[\left[\mathbf{\Lambda}_{X\psi}(\omega) \cdot \begin{pmatrix} i\alpha_{\text{probe}} \\ -i\alpha_{\text{probe}}^* \\ 0 \\ \vdots \end{pmatrix}\right]_k + \sqrt{2}|\alpha_{\text{out},k}|\sin(\psi)e^{-i\omega\tau}\right\}\delta\phi(\omega), \quad (2.156)$$

and its PSD:

$$\bar{S}_{\tilde{i}_c\tilde{i}_c}(\omega) = 2\eta_{\text{QE}}\eta_{\text{det}}\eta|\alpha_{\text{LO}}|^2\left|\left[\left[\mathbf{\Lambda}_{X\psi}(\omega) \cdot \begin{pmatrix} i\alpha_{\text{probe}} \\ -i\alpha_{\text{probe}}^* \\ 0 \\ \vdots \end{pmatrix}\right]_k + \sqrt{2}|\alpha_{\text{out},k}|\sin(\psi)e^{-i\omega\tau}\right|^2\bar{S}_{\delta\phi\delta\phi}(\omega). \quad (2.157)$$

that finishes our model for the BHD signal of a cavity optomechanical signal. We can use $\bar{S}_{\hat{i}_i\hat{i}_i}(\omega) = \bar{S}_{\hat{i}_q\hat{i}_q}(\omega) + \bar{S}_{i_c i_c}(\omega)$ to fit our experiments.

Before wrapping up our discussion, I want to illustrate how the influence of phase noise in our measurement depends on the delay between signal and LO. To do so, let us remove the optomechanical system from the probe path. This can be done by setting $\mathbf{\Lambda}(\omega) = \mathbb{I}$ and $\alpha_s = \sqrt{\eta}\alpha_{\text{out}} = \sqrt{\eta}\alpha_{\text{probe}}$ and inserting into Equation 2.157:

$$\bar{S}_{\tilde{i}_c\tilde{i}_c}^{\text{Delay}}(\omega) = 4\eta_{\text{QE}}\eta_{\text{det}}\eta|\alpha_{\text{LO}}|^2|1 - e^{-i\omega\tau}|^2\bar{S}_{\delta\phi\delta\phi}(\omega), \quad (2.158)$$

For no delay $\tau = 0$, the phase noise contribution vanishes. This is obvious, if there is no delay in either path, both beams arrive at the detector with the same phase and whatever beam we choose as phase reference, the phase of the other is zero. With a delay, we can measure the phase noise of our laser (see Subsection 5.4.2 for more details and an actual measurement).

Chapter 3

A low-noise micro-cavity for quantum optomechanics

The main goal of this work has been to build a cavity optomechanics experiment that exhibits quantum behavior at room temperature. Throughout this chapter, we will explain how we designed and built a low-noise optical micro-cavity that tackles the main challenges found in the way towards room-temperature optomechanics.

3.1 Introduction

What does it exactly mean for the system to be in the quantum regime at room-temperature? We will use the following straight-forward criterion:

A system is in the quantum regime when quantum fluctuations play a bigger role than thermal fluctuations in determining the statistics of our system.

In such situations, our classical models of the system will start to fail. If we look at the different physical subsystems forming a cavity optomechanics system, we can translate the criterion into mathematical conditions. First, the light trapped in the optical cavity, its amplitude variance when thermalized is:

$$\langle \Delta \hat{X}^2 \rangle_{\text{th}} = N_{\text{th}} + \frac{1}{2}. \quad (3.1)$$

The one-half ultimately originating in the fact that amplitude and phase are non-commuting observables. An optical field in the near-infrared (around 200THz) has a thermal occupation $N_{\text{th}} \ll \frac{1}{2}$ when thermalized to $T \simeq 300\text{K}$, thus, its statistics are dominated by the quantum fluctuations. Prior to pumping the cavity with light, we can safely assume that its optical mode is in the ground-state, as well as the input channels. As long as we use quantum limited sources of light, we can keep our optical degrees of freedom in the quantum regime.

Contrary to light, the mechanical resonator imposes a challenge due to its low mechanical frequency. As we discussed in Subsection 2.2.1, the variance in the position of a thermalized mechanical resonator is given by:

$$\langle \hat{q}^2 \rangle = q_{\text{z.p.}}^2 + 2q_{\text{z.p.}}^2 n_{\text{th}}. \quad (3.2)$$

At first glance, it seems impossible to reach the quantum regime for a given frequency without modifying the environment temperature. The trick lies in that, through various cooling

schemes, one can lower the effective temperature of the resonator while keeping the environment at room-temperature. In other words, we can prepare the resonator in a Gaussian mixed state resembling that of a thermal state at temperature T_{eff} which is lower than T . If such state has an effective occupation of \bar{n} phonons, the measured variance on its position will mostly be caused by quantum fluctuations as long as:

$$\bar{n} \leq \frac{1}{2}. \quad (3.3)$$

We can also apply the criterion to the optomechanical interaction itself. In our previous discussion about optomechanical squeezing, we found that the interaction is quantum dominated as long as:

$$C_q = \frac{4g^2}{\kappa\Gamma_m n_{\text{th}}} \geq 1 + \frac{4\Delta^2}{\kappa^2} \quad (3.4)$$

The quantum cooperativity is a great figure of merit for the actual performance of an experiment run, while the single-photon cooperativity $C_0 = \frac{4g_0^2}{\kappa\Gamma_m}$ considers only the intrinsic parameters of our optomechanical apparatus.

Faced with the task of building a MIM system that can reach the quantum regime at room-temperature, we must be careful in adjusting the parameters that are under our control. In the following subsections, I discuss the fundamental arguments for choosing certain parameters as well as the technical caveats that must be considered in our design decisions.

3.1.1 The length of the cavity

If the cavity is built with mirrors of a certain finesse, the quantum cooperativity is independent of cavity length for a given input power \dot{n}_{in} . This can be seen from the following dependencies:

$$C_q \propto \frac{g_0^2 n_c}{\kappa} \quad g_0 \propto \frac{1}{L} \quad n_c \propto \frac{\dot{n}_{\text{in}}}{\kappa} \quad \kappa \propto \frac{1}{L} \implies C_q \propto \dot{n}_{\text{in}} \quad (3.5)$$

In theory, it seems that shorter or longer cavities have the same performance. In practice, shorter cavities are better when we consider technical noises. In particular, the effects of laser frequency noise are mitigated in shorter cavities. Looking back to the equations of the intracavity field (Equation 2.95 and Equation 2.96), we find the following dependency on detuning noise $\delta\Delta$:

$$S_{\hat{X}\hat{X}} \propto n_c S_{\Delta\Delta} \quad (3.6)$$

while the transduction of position to light scales with:

$$S_{\hat{X}\hat{X}} \propto g_0^2 n_c S_{\hat{Q}\hat{Q}}. \quad (3.7)$$

Ultimately, the ratio of mechanical signal to frequency noise signal detected in the output field will scale proportional to g_0^2 . Notice that shorter cavities do not mitigate mechanical mirror noise. Mirror motion will couple in the same manner as our resonator, although through a different set of g'_0 . The coupling rates of the mirror modes also scale inversely with the length, thus, the signal-to-mirror noise ratio is independent of cavity length.

3.1.2 The mirror reflectivity

The quantum cooperativity is inversely proportional to the cavity linewidth κ , which favors high-finesse cavities. However, one must not succumb to the temptation of using mirrors with

the highest reflectivity possible. First, it is favorable for the two mirrors of the cavity to have different reflectivities. Measurement should be performed on the light exiting the cavity through the less reflective (more transmissive) mirror. Second, the rate κ_k associated with the measurement port should be significantly larger than the loss rate κ_ℓ so that the cavity remains over-coupled. This is crucial in MIM systems. Modern distributed Bragg reflector coatings have low losses compared to their transmissivities, making it easier to be in an over-coupled or critically-coupled regime if no other losses mechanisms are present. But when a thin membrane is inserted in between, the main loss channel might become the sub-optimal parallelism between membrane and mirrors or optical absorption.

3.1.3 Tunability

In a MIM system, g_0 depends on the equilibrium position of the resonator respect to intracavity field nodes. We have two options in order to optimize g_0 : we either move the resonator or we adjust the field's nodes by changing the resonant wavelength. Although possible, having control of both position and tilt of the resonator while it sits inside the cavity is a big experimental challenge. One needs a 5-axis stage that is both compatible with ultra-high vacuum and has enough mechanical stability. An equivalent and easier option is to mount the mirrors on piezoelectric actuators (PZT). The PZTs are mounted such that the mirrors move along the cavity's axis. By moving both mirrors in the same direction and by the same amount, one can keep the cavity resonant with any given laser frequency while optimizing g_0 . These solutions allow the optimization of g_0 for any set wavelength. This is a requirement for certain types of experiments. For example, in hybrids experiments, for example, entangling states of an ultracold atomic gas to a cavity optomechanical system, the wavelength of the light is set by the atomic system and the optomechanical system must adjust.

If the experimental requirements allow for wide-tunability of the laser's wavelength, a completely rigid optomechanical system can be used. The different optical resonances will have different g_0 as the position of the field nodes and anti-nodes changes respect to the membrane. The laser can be tuned to a resonance that ensures high enough g_0 . In general, it is not guaranteed that any of the available optical resonances ensures the largest g_0 . How close to the system can get to the global maximum depends on the FSR of the cavity, a smaller FSR allows for more granular adjustment.

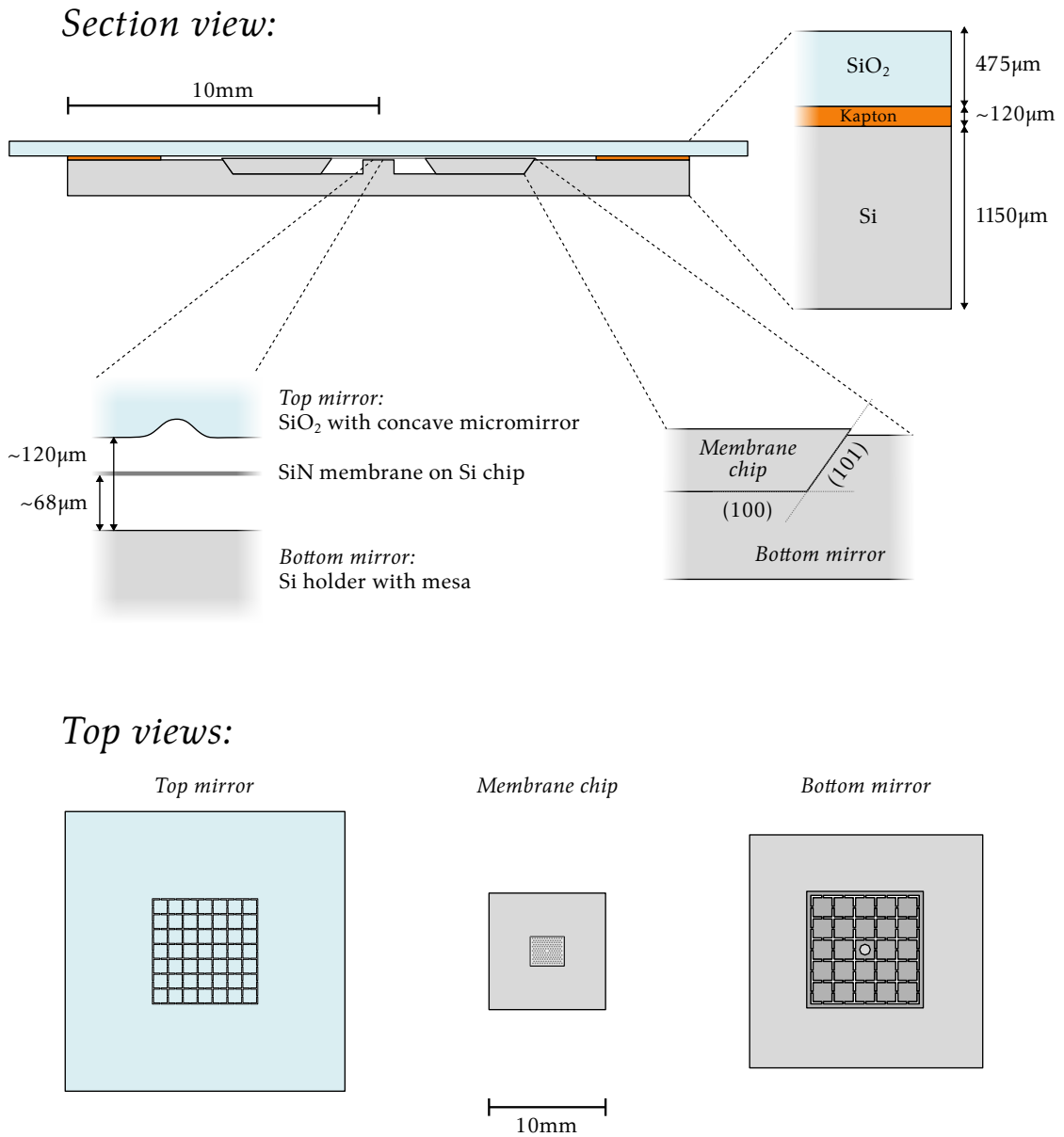


Figure 3.1: The membrane-in-the-middle microcavity optomechanical system. Drawings to scale of the four elements of our system: a bottom mirror silicon chip, a silicon chip with a suspended silicon-nitride membrane, Kapton tape used as a spacer and a top fused silica mirror where a concave mirror has been fabricated.

3.2 Overall description of the experiment

We have built a high-finesse micro-cavity based on structured substrates, its overall geometry can be seen in Figure 3.1. It contains no moving parts: the cavity is based on a stack of planar substrates with sufficient parallelism.

The base is a $20\text{ mm} \times 20\text{ mm}$ silicon chip with a thickness of $1150\text{ }\mu\text{m}$. The chip serves simultaneously as a holder for another chip containing a suspended silicon-nitride membrane, and as one of the mirrors of the optical cavity. We call this the *bottom mirror* because the membrane chip rests on it, held only by gravity. To ensure a good fit, the bottom mirror has been sculpted with a negative of the membrane chip. As both are fabricated with Potassium Hydroxide (KOH) etching¹, the walls are perfectly co-planar along the (111) crystalline plane. Both chips have been fabricated from double-sided polished wafers, ensuring that they rest on each other perfectly parallel. At the center of the bottom mirror, a *mesa* has been left by protecting a 1mm-diameter region from the KOH etch. The top surface of the mesa, which retains the original wafer thickness, sits approximately $68\text{ }\mu\text{m}$ away from the membrane. The surface of the mesa is still pristine as it has been left untouched by the etching process. After coating with low-loss distributed Bragg reflector² with a target transmission of 10ppm at 1550 nm , the mesa becomes one of the high-finesse mirrors of our cavity. The bottom surface is coated with an anti-reflective coating.

On the edges of the top side of the bottom mirror, polyimide tape (Kapton) is placed in order to be used as a spacer. One layer of Kapton tape provides $\approx 60\text{ }\mu\text{m}$ of thickness. We chose Kapton tape because it is widely available and compatible with Ultra High Vacuum (UHV). We have also considered using polyimide film (same as Kapton tape but with no adhesive) and aluminium foil[52], but we have found no problems with the presence of adhesive and appreciated its convenience when building the cavity. We have settled on using two layers of Kapton tape for a total thickness around $120\text{ }\mu\text{m}$.

On the Kapton tape spacer sits our *top mirror*. The top mirror is a square $24\text{ mm} \times 24\text{ mm}$ fused silica substrate with a thickness of $475\text{ }\mu\text{m}$. We chose fused silica so that we can machine a concave micromirror template using the well established CO_2 laser ablation technique[53]. The fabrication is explained and characterized in detail in Chapter 4. We ablate a $\approx 3\text{ }\mu\text{m}$ deep concave Gaussian-shaped dimple. Close to the center of the feature, its radius of curvature is around $300\text{ }\mu\text{m}$. Features created through laser ablation have ultra-low roughness due to the reflow of melted material and re-solidification under surface tension, it allows for ultra-high finesse cavities after coating with an ultra-low loss high reflective coating with a target transmission of 100ppm at 1550 nm .

Contrary to prior microcavity MIM systems [52, 54, 55], we fabricate the concave micro-mirror on a planar substrate instead of fabricating it on the tip of an optical fiber. We did so in order for both bottom and top mirrors to be patterned with phononic crystals. The idea is inspired by the work of Saarinen et al [52]. A pattern of cross-shaped holes can remove all mechanical modes from an interval of frequencies. In the *bandgap*, there is, in principle, no thermomechanical motion. In the following section, we will see how, without such phononic shield, it would be impossible to resolve the ground-state motion of our resonator. The bottom mirror was patterned using Deep Reactive Ion Etching (DRIE), which in contrast to KOH etch-

¹Potassium Hydroxide (KOH) etching, is a highly anisotropic etching technique that etches along the normal of the (111) crystallographic plane. In a (100) oriented wafer, it etches walls that form a 54.7 deg angle with the surface.

²At the time of this work, it was challenging to find companies able to coat non-standard substrates with ultra-low-loss high-reflective coatings, usually done with ion beam sputtering. All substrates used in this work were coated by FiveNine Optics in Boulder, CO, USA. (www.fivenineoptics.com). LASEROPTIK in Garbsen, Germany (www.laseroptik.com) were also willing to coat our substrates.

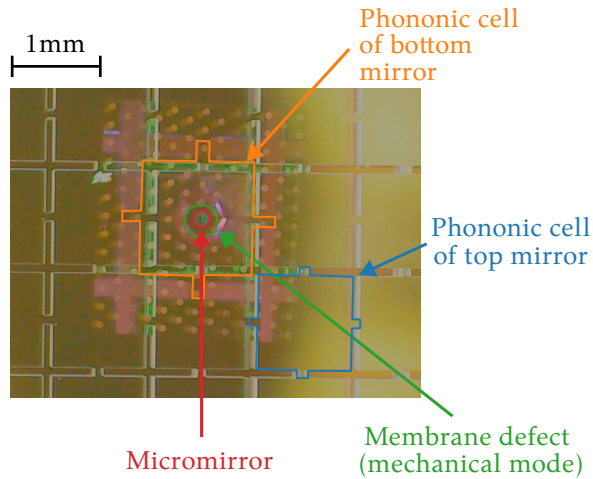


Figure 3.2: Assembled MIM system as seen through a microscope. The phononic structure of the bottom mirror (highlighted in orange) can be seen through the suspended SiN membrane. The pillars defining the phononic structure of the resonator can be seen thanks to their diffraction. The hexagonal defect on the membrane’s phononic crystal is highlighted in green. The top mirror is positioned so that the concave micromirror (highlighted in red) sits inside the membrane defect, thus ensuring good mechanical-optical overlap. The phononic structure of the top mirror can also be appreciated (highlighted in blue).

ing, it can etch vertical walls. The top mirror was etched at an external company³ using Laser Induced Deep Etching (LIDE). LIDE is a novel process that starts with a high-power pulsed laser ablating through-holes in a glass wafer. The second step is a wet etching technique that has a higher etch rate at the surface of the walls of the through-holes.

The system, which is build by stacking the different layers, is held by clamping the top mirror, spacer and bottom mirror against a holder using copper spring clips. There is no contact between the top mirror and the membrane chip. This simple structure allows us to achieve cavities as short as 126 μm when loaded with a membrane, which makes it one of the shortest MIM systems that can be found in the literature. To our knowledge, 43.8 μm [55], 90 μm [54] and 95 μm [52] are the three shortest MIM systems implemented, with ours being the fourth.

The finesse of the loaded cavity is above 60000 at wavelengths close to the coating optimum. This is the finesse expected from the coating specifications, demonstrating the success of our bottom mirror in ensuring parallelism between bottom mirror and membrane. At the same time, we have shown that semiconductor grade polished silicon is a capable substrate for high-finesse mirrors.

3.2.1 Assembly procedure

The assembly procedure has been improved iteratively through out the 10 months that the system has been in operation. Through trial-and-error, we have identified an assembly procedure that ensures short cavities with high-finesse. The procedure described below was identified just two months before the realization of this report and we thus believe there is room for improve-

³Vitron www.vitron.com

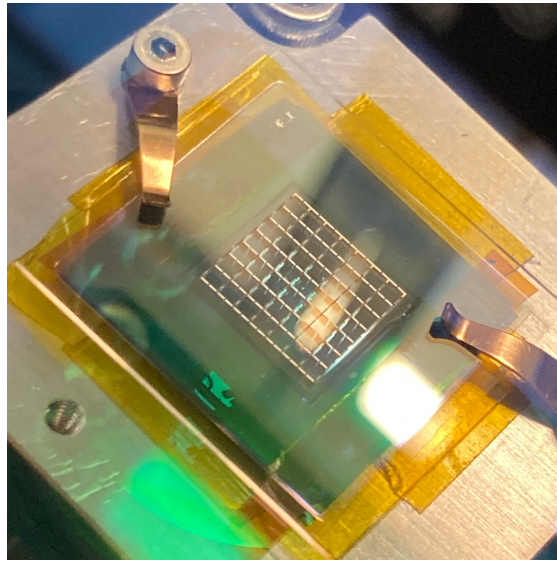


Figure 3.3: Photograph of the MIM system taken through the window of the vacuum chamber.

ment.

1. **Mounting the bottom mirror on the holder:** Two stripes of Kapton tape are adhered to the surface of our aluminium holder⁴ in order to create a smooth surface for the bottom mirror to rest on. The bottom mirror is placed on that surface, to secure it, two additional stripes of $\approx 60\mu\text{m}$ thick Kapton tape are placed along two parallel edges of the chip. The Kapton tape is cut longer than the chip itself, with the ends of the strips adhered to the holder. Thus, the tape acts as both a fixing mechanism for the bottom mirror and as a spacer for the top mirror⁵. The process is repeated so that at each edge there are two layers of Kapton tape with total thickness $\approx 120\mu\text{m}$. One layer of Kapton is too thin, the top mirror will crash against the membrane. When this happens, the membrane explodes and the residue left in the mirror makes them unusable. A key discovery was that using three layers of tape for a total thickness of $\approx 180\mu\text{m}$ severely affects the finesse. We believe this is due to the nature of our concave micro-mirrors. Longer cavities imply a larger beam waist at the curved mirror, the beam waist at the curved mirror for a $120\mu\text{m}$ long cavity is $9.1\mu\text{m}$, which increases to $11.2\mu\text{m}$ for a $180\mu\text{m}$ long cavity. Due to the Gaussian shape of our micromirror, a spherical-like profile is only ensured up to a certain distance from the center, sufficiently large suffer clipping losses [56]. We suspect that the threshold for clipping losses lies between the cavity mode sizes resulting from two and three layers.
2. **Placing the membrane on the bottom mirror:** The chips with our membrane resonators are stored in a Gel-Pak container⁶. Particles on the chip's surface around the membrane are removed by adhering and de-adhering a piece of Kapton tape prior to removal from the container. The elastomer that lines the container will capture any particles present at the bottom of the chip. Once the chip is picked up, it is usually free of dust particles and

⁴A technical drawing of the holder can be found in Figure E.2

⁵Double sided Kapton tape should not be used to secure the bottom mirror to the holder. After the system was in vacuum, we found it impossible to remove the bottom mirror from the holder without it fracturing.

⁶www.gelpak.com

is gently placed in the holder sculpted on the bottom mirror.

3. **Placing the top mirror:** This is the most critical step in the process due to the high risk of the membrane breaking. First attempts at building a 120 μm long cavity failed due to the membrane breaking once the top mirror was dropped in place. We ensured that it was not caused by contact between the top mirror and the membrane by measuring the distance between the membrane and the mesa mirror surface through interferometry. We believe the rupture of the membrane is due to the sudden movement of air above the membrane. We were able to place the top mirror in the two-layer spacer configuration by sliding it from one side. The top mirror is placed offset $> 10\text{ mm}$ from the center so that it does not cover the suspended membrane. It is then gently slid into position. It is critical that no large ($\geq 70\text{ }\mu\text{m}$) particles are present on the membrane chip surface because they will be dragged into the suspended SiN membrane during this process.
4. **Clamping and aligning:** The micro-mirror is roughly placed on top of the membrane's mechanical mode by eye, then two small copper spring clips are tightened. They are placed opposite of each other, pressing together the top mirror, spacer and bottom mirror. With the help of a microscope, the top mirror is pushed using the end of plastic-tipped tweezers so that the micromirror is centered on the membrane's phononic crystal defect that defines the mechanical mode. A microscope image of the system is shown in Figure 3.2. In a matter of minutes, we have ensured good overlap between the optical mode and the mechanical mode.
5. **Attachment to the vacuum chamber and final alignment:** The holder with the MIM system is attached using screws to a larger holder which is kept permanently in the vacuum chamber (more details in Appendix E). The chamber is closed and the air evacuated. A small USB microscope is used to observe the system again, usually, due to the vibrations caused by tightening the vacuum viewport, the membrane chip has slid away from the center, as there is some tolerance in the chip holder. At this point, the only way of re-aligning the mechanical mode back to the center of the top micromirror is by shaking the system. In an intuitive process of hitting different sides of the vacuum chamber with the handle of a screwdriver, the membrane is re-positioned. This process usually takes a few minutes.

A photograph of the assembled system is shown in Figure 3.3.

3.3 The mechanical resonator: Density modulated phononic membranes

The design and fabrication of high-quality mechanical resonators is not part of this work, but rather the effort of my colleague Dennis Høj. The resonator used in this work is a Density modulated Phononic Membrane (DPM) [20]. DPMs are the most recent iteration in suspended stoichiometric silicon-nitride (SiN) membrane resonators, which were used for the first time in the year 2008 [57]. Stoichiometric SiN, which is SiN grown on silicon, has a high tensile stress in the order of 1 GPa due to the lattice mismatch of SiN and silicon. The high stress enhances the phenomenon of *damping dilution*, in which the mechanical quality factor of a tensile stressed material is enhanced orders of magnitude higher than the intrinsic quality factor due to internal friction (bending losses) [58].

DPMs fall in the category of phononic crystal engineered resonators. In order to create an isolated mechanical mode, the stoichiometric SiN membrane suspended on a silicon frame is patterned with a pattern of features that gives rise to a phononic bandgap. Breaking the pattern

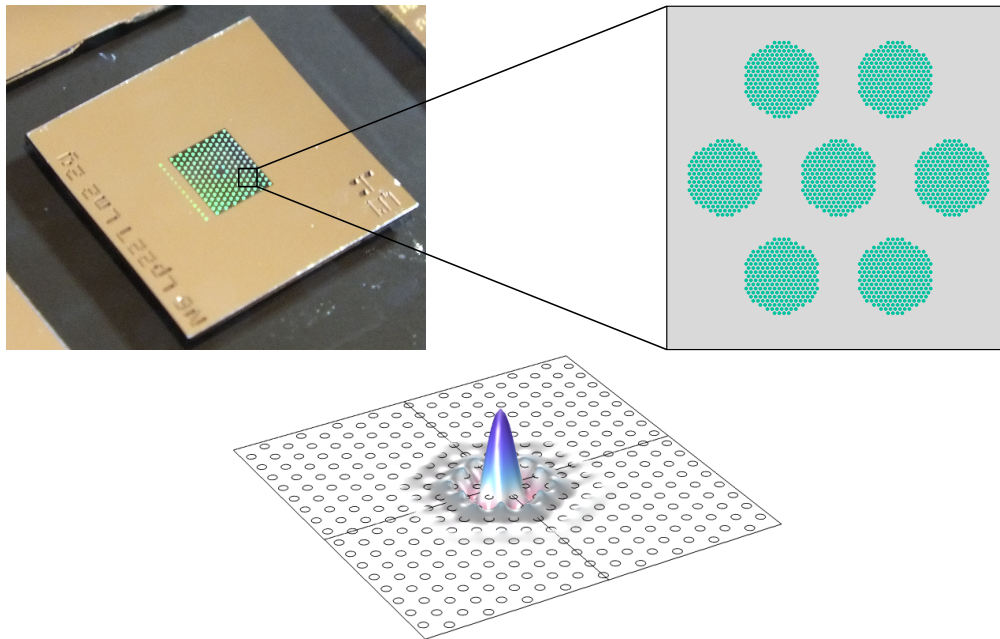


Figure 3.4: Density modulated phononic membrane. A suspended $2.9\text{ mm} \times 2.5\text{ mm} \times 20\text{ nm}$ membrane of stoichiometric silicon-nitride has been modified by adding circular regions filled with $\approx 1\text{ }\mu\text{m}$ tall nano-pillars. The regions, that have a diameter around $86\text{ }\mu\text{m}$, form an hexagonal lattice with a lattice constant around $220\text{ }\mu\text{m}$. The nano-pillars, which are $\approx 1\text{ }\mu\text{m}$ thick, form a smaller hexagonal lattice with constant $\approx 2\text{ }\mu\text{m}$. **Top left:** Photograph of the membrane chip. **Top right:** Drawing of the nano-pillar filled regions. **Bottom:** Finite-element simulation of the fundamental mechanical mode, courtesy of Yincheng Shi.

at the center of the crystal, a single mechanical mode that is highly isolated from the substrate is created [18]. Additionally, the crystal can be optimized to reduce the curvature of the central mode curvature at edges of the membrane. This design technique, known as *soft clamping*, is vital for reducing the intrinsic mechanical losses caused by curvature at membranes contour, trampoline-like designs focus on reducing this kind of losses [16, 17, 19].

The innovation of DPMs lies in the manner the phononic crystal is defined. The main way of inducing an acoustic bandgap has been through a pattern of holes, which in turn induce pattern of stress. As their name indicates, Density modulated Phononic Membranes are based on creating a pattern of effective density by adding mass. Replacing the holes in a traditional phononic membrane with tall pillars is a bad strategy due to the large boundary length between the membrane and the wall at the pillar's base. Instead, an effective pillar can be made through a large quantity of nano-pillars, each with negligible contribution to bending losses. A conventional picture and an illustrative drawing of a DPM is shown in Figure 3.4.

The central modes of DPMs can have frequencies in the range between 1.1 MHz and 1.5 MHz , surrounded by a bandgap $\approx 400\text{ kHz}$ wide. Their quality factors can reach up to 10^9 when operated in Ultra High Vacuum ($< 10^{-7}\text{ mbar}$), with $Q \times \Omega_m$ factors that allow for tens of coherent oscillations. The effective mass is around 2 ng , resulting in zero point fluctuations around 2 fm . These are the relevant parameters for our experiment, the reader can find more details about

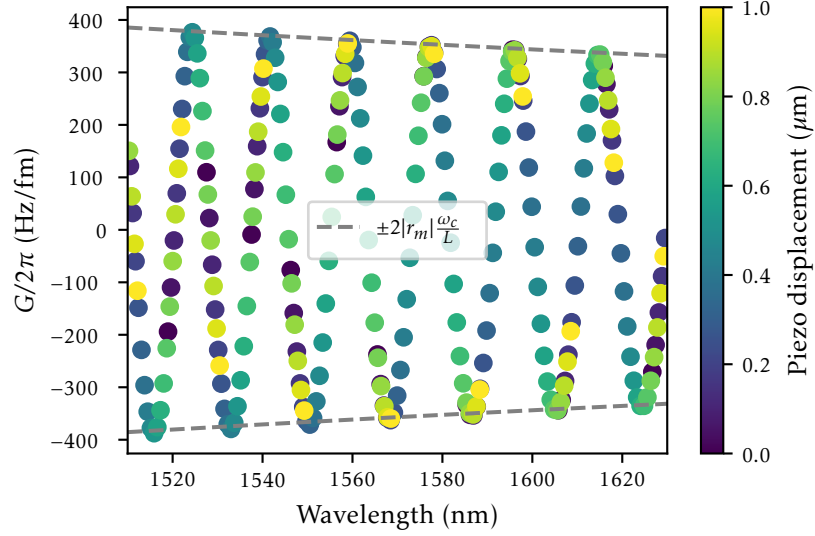


Figure 3.5: Optomechanical coupling G in a cavity with a movable mirror. Each dot represents a resonant wavelength, with its color proportional to the displacement of the mirror respect to the original cavity length $L = 126\mu\text{m}$. The dashed lines are the maximum G achievable for a 20nm thick silicon-nitride membrane.

the membrane and its fabrication in the paper by Høj et al [20].

3.4 Tuning the optomechanical coupling

We have decided to build a rigid system. Neither the mirrors nor the membrane can be moved in order to make the cavity resonant with the laser or to place the membrane in a position of high optomechanical coupling. We rely on finding a resonant wavelength with strong optomechanical coupling in the range of our laser. Our experiment's main laser is a widely-tunable diode laser (TOPTICA CTL 1550) with a tunability range from 1510nm to 1630nm. The numerical calculations of optomechanical coupling G and linewidth κ presented in Section 2.5 are done using the parameters of our experiment. They show that we have enough wavelength tunability to access strong G resonant modes.

Our initial experimental design included piezoelectric actuation of the top mirror, which would require 3 independent $1.5\text{mm} \times 1.5\text{mm} \times 1\text{mm}$ piezoelectric chips (Thorlabs PA3BC). We finally decided against this idea, but we will discuss it here in order to illustrate why the decision was made. One advantage of cavity length adjustment is that we can make the cavity resonant with any laser wavelength as long as the piezo displacement is greater than half the wavelength, as a consequence, we can tune the cavity to a wavelength that ensures that the membrane sits between a node and anti-node of the intracavity field, achieving maximum optomechanical coupling. In Figure 3.5, we have numerically obtained G at different modes at different cavity lengths to show that it is possible to optimize G . The simulation has been done in the same way as in Section 2.5.

Ultimately, the increase in G obtainable by adjusting both wavelength and length and only

adjusting the wavelength (which in the simulations shown in Figure 2.8 and Figure 3.5) is around a 30% and does not warrant the technical challenge of operating three piezoelectric chips in Ultra High Vacuum. Although we have not tested it, we can also predict that the passive alignment between the bottom and top mirror would be much poorer, relying on the tolerances of the three piezo chips used.

We also explored the idea of assembling the system in the rigid configuration, just as shown in Figure 3.1, but allow for cavity length changes by pressing on the top or bottom mirror as to contract the Kapton spacer. In order to achieve a tunability of one FSR, we would need $\approx 775\text{nm}$ of contraction of the $\approx 120\mu\text{m}$ thick spacer, a strain of $\varepsilon = 6.5 \times 10^{-3}$. Using the Young modulus of Kapton $E = 2.75\text{GPa}$ ⁷ we find that the stress needed for such deformation would be in the order of 20MPa, or 2000N on a 1cm^2 area, which is in the order of the blocking force of common piezoelectric actuators. The idea was not tested on the cavity due to time constraints, but a Michelson interferometer was used to show that a piezoelectric ring of 15mm outer diameter, 9mm inner diameter, 3.2mm thick and blocking force of 8450N (Thorlabs PA44M3K) could deform two layers of Kapton film (total thickness $150\mu\text{m}$) by more than $1\mu\text{m}$.

3.5 Low-noise mirrors

The mirrors in our cavity have been engineered with phononic crystals in order to remove thermomechanical motion around the membrane's frequency. The mechanical mode of the mirrors in a MIM system form a canonical optomechanical system, with optomechanical coupling factor G roughly $1/2|r_m|$ larger than the membrane modes. Despite that, the single-photon coupling rate g_0 is much smaller due to the small zero-point fluctuations of the mirror modes. In this section we show that, despite the fact that the thermomechanical motion of mirror modes is an order of magnitude weaker due to the disparity in g_0 , mirror motion can still mask the signal of our mode of interest when it is cooled to low phonon number occupations. We will then describe in detail how we designed phononic crystal patterns that effectively reduce thermomechanical motion of the mirrors.

3.5.1 Thermomechanical motion of regular mirrors

In order to illustrate the need for phononic patterning, we have simulated the thermomechanical motion of the top mirror in the absence of a phononic pattern. As described at the start of the chapter, the top mirror is made from a fused silica square substrate with dimensions $24\text{mm} \times 24\text{mm} \times 0.475\text{mm}$. We have found the thermomechanical motion spectrum through the following steps:

1. We have found the eigenfrequencies and quality factors of the mirror modes using COMSOL Multiphysics®. To model how the mirror is clamped in the experimental set-up, the boundary conditions are set so that two opposite sides of the substrate are fixed. We use the material properties of fused silica and assume a loss factor of 1×10^{-4} based on values found in the literature[59]. 1200 eigenfrequencies are found, up to approximately 1.6MHz.
2. The effective mass of each mode is obtained using the methodology described in [60], which consists in a volume integral of the density weighted with the mode's normalized shape.

⁷Manufacturer's datasheet

3. The PSD of thermomechanical motion in units of m^2/Hz is found summing the responses of each mode to the thermal force specified by the fluctuation-dissipation theorem.

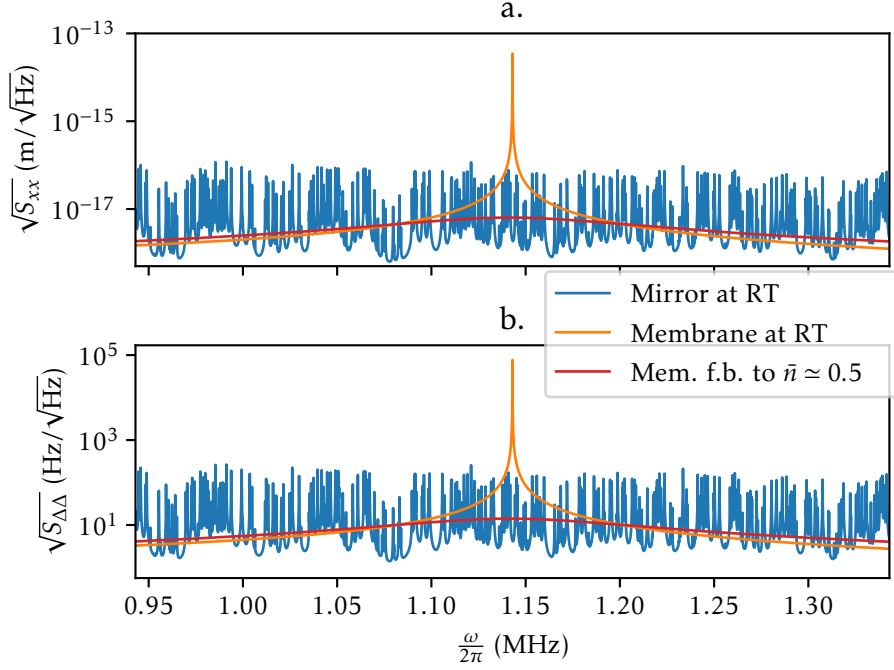


Figure 3.6: Thermomechanical motion of fused silica plate (blue) compared to that of the membrane's mode (orange) and the motion under strong feedback cooling (red). The top plot is the motion itself and the bottom plot its effect on the cavity frequency according to the optomechanical coupling of the end-mirrors and of the membrane in a MIM configuration.

The single-sided power spectral density of the mirror thermomechanical motion at room temperature is plotted in Figure 3.6a. For comparison, the spectrum of the central mode of a membrane resonator is also plotted ($\Omega_m = 2\pi \cdot 1.143\text{MHz}$, $Q = 10^8$, $m_{\text{eff}} = 2\text{ng}$), as well as the same mode subjected to measurement-based feedback cooling down to $\bar{n} \approx 0.5$ [61]. In the experiment, the position is inferred from its effect in cavity detuning. In Figure 3.6b, the PSD of the cavity detuning is shown. We take into account that the mirror and membrane motion are transduced into cavity detuning through different couplings $G_{\text{mirror}} \approx 9.35 \times 10^{18}\text{Hz m}^{-1}$ and $G_{\text{membrane}} = 2.21 \times 10^{18}\text{Hz m}^{-1}$ (obtained considering a $130\mu\text{m}$ long cavity and 20nm thick SiN membrane).

From this data, we see how the mirror motion, which is well below the thermomechanical motion of our resonator, can actually bury the signal when we approach its ground-state. By taking the average mirror motion around the resonator frequency, we approximate the minimal phonon occupation reachable through measurement-based feedback-cooling to be ≈ 2 .

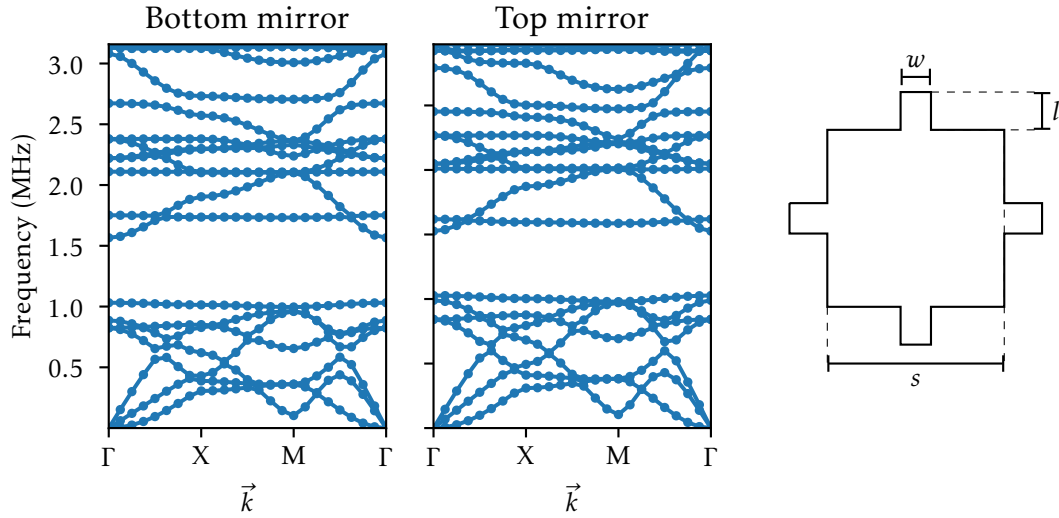


Figure 3.7: **Left:** Simulated band structure of the phononic shield in the bottom mirror and the top mirror. Both designs have been optimized to maximize the bandgap around 1.3MHz. **Right:** Unit cell of the pattern used on both mirrors.

3.5.2 Design of patterned mirror substrates

In the same manner that a phononic crystal pattern defines the bandgap in our mechanical resonator, we can engineer one in our mirror. As commented previously, we have chosen materials that can be etched across their total thickness, allowing for high contrast patterns. We have designed a pattern of squares connected by rectangle beams⁸ inspired by the work of Yu et al [62]. The pattern is defined by three parameters: the length of the square's side s ; the length of the beams connecting each square $2l$ and the width of the beams w . The acoustic bandgap resulting from this parameters can be numerically estimated and therefore optimized. We use COMSOL Multiphysics® simulations to optimize three designs around 1.1MHz, 1.3MHz and 1.5MHz for each substrate (475 μm of glass for the top mirror and 610 μm of silicon for the bottom). We simulate the unit cell with periodic Floquet boundary conditions, thus simulating an infinitely extending pattern. We optimize using the default algorithm found in *Python's SciPy* library (`scipy.optimize.minimize`) [63].

Table 3.1 summarizes the results of the optimization process. The simulated band structure of the optimal design for 1.3MHz central frequency is shown in Figure 3.7. The resulting bandgap in all configurations is around 500kHz wide, which is in the order of the bandgap of the mechanical resonator.

3.5.3 Cavity noise reduction

We have checked the performance of our phononic shields in two independent measurements. First, we have shaken the cavity using a piezoelectric actuator and measured the effect on the output field. Second, we have measured the spectrum of the reflected phase with a balanced

⁸or cross-shaped holes if you hold a glass-half-empty point of view

	Top mirror (475 μm SiO ₂)			Bottom mirror (610 μm Si)		
	1.1MHz	1.3MHz	1.5MHz	1.1MHz	1.3MHz	1.5MHz
s (μm)	1300	1170	1060	1756	1582	1546
w (μm)	100	101	107	100	210	138
l (μm)	55	53	53	58	105	58

Table 3.1: Optimized phononic crystal parameters for the different substrates at different frequencies.

homodyne detector. Unfortunately, due to the the monetary and time cost of fabricating and coating the mirrors, we do not have mirrors without phononic patterns. Ideally, we would have built to identical unloaded cavities and compared the spectrum of the output field and extract a noise reduction factor.

As stated, the first evidence of isolation has been the response of the cavity to mechanical vibrations. The response has been measured by locking our laser to the slope of a resonance of the empty cavity and recording the transmission signal. A small piezoelectric actuator is attached to the holder of the cavity using a copper clamp. A signal generator sends sinusoidal voltage signals to the actuator from 500kHz to 3MHz in steps of 1kHz, at each frequency, an oscilloscope records the transmission signal. We use the standard deviation of the time trace as a measure of cavity noise. Figure 3.8 shows a clear reduction of the cavity sensitivity to vibrations in the span between 1MHz and 1.5MHz, matching well with our predictions. The

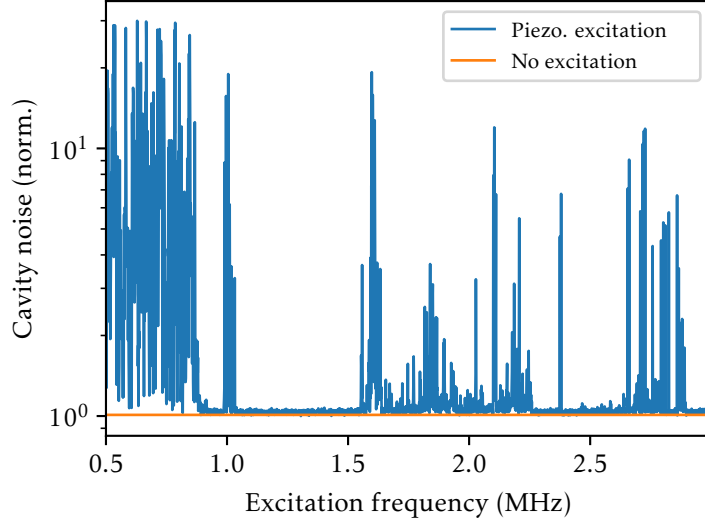


Figure 3.8: Response of the empty cavity transmission signal to mechanical excitation.

second evidence for the effectiveness of our design comes from homodyne detection of the cavity's reflection. The laser is locked to the side of the resonance. In this measurement we are also slightly sensitive to laser phase noise (see Section 6.3). In the spectrum shown in Figure 3.9, we clearly see a bandgap in the expected frequency region. We interpret the overall behavior of the signal as the forest of peaks caused by mechanical modes of the mirrors superimposed to

the phase noise.

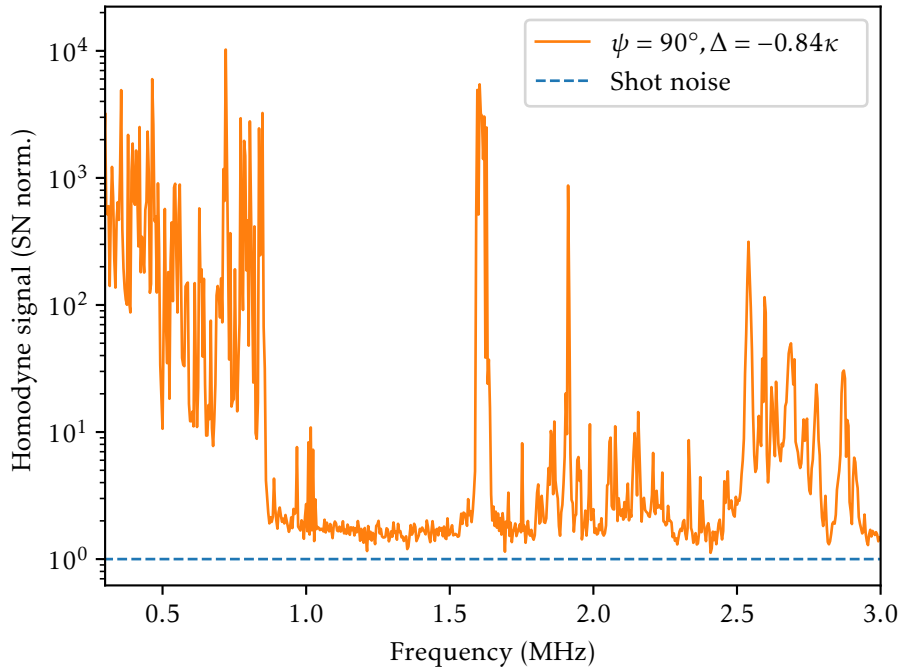


Figure 3.9: Power spectral density of the reflected phase signal of the cavity when the laser frequency is locked at the side of the resonance ($\Delta = -0.84\kappa$). The spectrum has been normalized to the shot-noise signal of the local oscillator.

3.6 The optical set-up

Although the optical set-up is adjusted depending on the experiment performed, Figure 3.10 shows a representative configuration based on collecting the reflected signal from the cavity. It has been used to perform most of the characterization that will be presented in the next chapter. The optical circuit starts at the laser, a diode laser (Toptica CTL 1550) with a tunability range from 1510nm to 1630nm. The laser emits in free-space, but is coupled to polarization maintaining (PM) fiber using an integrated coupling device provided by the manufacturer (Toptica Fiberdock). The first element after the laser is an electro-optical modulator (EOM) that is used for different calibrations, after that the beam is split into the probe beam and the local oscillator (LO). The EOM is moved between before and after the split depending on the calibration needed. If not in use, it is kept before the split as it acts as a linear polarizer.

The probe beam power is adjusted with an electronic voltage optical attenuator (EVOA), its control voltage set by a digital-to-analog converter (DAC, NI Instruments) controlled by the experiment computer (PC). A fiber circulator is used to direct the probe beam towards the cavity. After the beam is collimated, a half-waveplate is used to adjust the polarization (this is needed due to birefringence in the cavity, see Subsection 5.1.2). The beam is mode matched to the cavity mode using an aspheric lens (Thorlabs A280TM-C, $f = 18.5$ mm). The collimator,

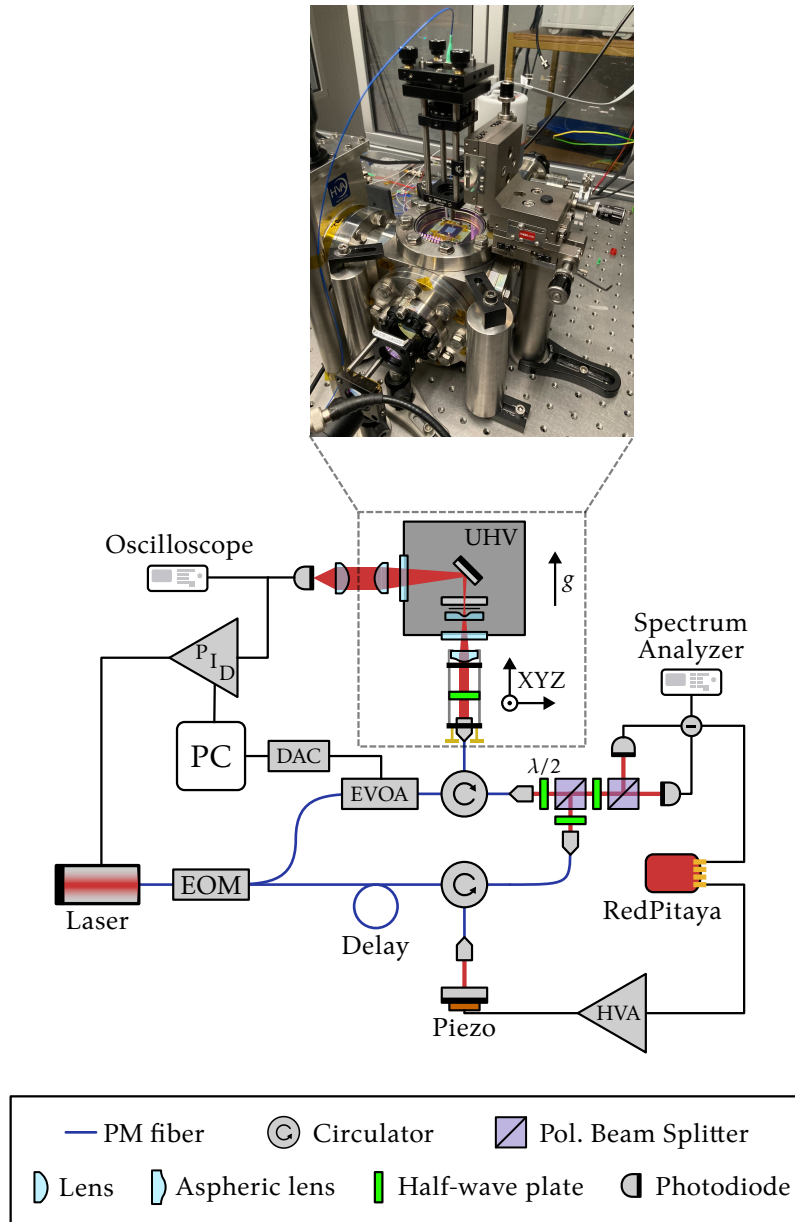


Figure 3.10: Schematic of the experimental set-up used to measure reflected light and a picture of the part of the set-up that couples light into the cavity. The purpose of each component is described in detail in the main text. EOM: Electro-Optical Modulator, EVOA: Electronic Variable Optical Attenuator, DAC: Digital to Analog Converter, PC: Experiment computer, PID: Proportional-Integral-Derivative controller, HVA: High Voltage Amplifier, UHV: Ultra-High Vacuum (vacuum chamber).

waveplate and lens are mounted in a cage, itself attached to a 3-axis translation stage. The collimator is mounted on a kinematic mount, providing the 2 remaining degrees of freedom to align the input beam to the cavity mode. The alignment procedure can be found in the section that follows.

The beam enters the UHV chamber housing the cavity through a fused silica window with an anti-reflective (AR) coating (more details about the vacuum set-up can be found in Appendix E). The transmission of the cavity is redirected 90 deg using a conventional mirror mounted on a rigid (non-adjustable) holder. The transmitted beam exits the cavity through another AR-coated window, it is then collimated using a $f = 175$ mm lens and then focused using a $f = 50$ mm lens into a 13.4mm^2 active area InGaAs amplified photodetector (Thorlabs PDA20CS2). The signal is used to keep the laser frequency resonant. Both an oscilloscope and Proportional-Integral-Derivative (PID) controller are available in the laser controller, which greatly simplifies data acquisition. Reflected light from the cavity re-enters the circulator. PM fiber circulators are polarizing elements, but due to the beam passing back and forth through the same half-wave plate, the polarization upon reentering the circulator is the same as when exiting and is redirected to a free-space homodyne detection set-up. The collection efficiency in this configuration is around $\eta \approx 0.5$

The LO beam has a similar optical circuit. The LO path also contains a circulator, which is used to reflect the LO off a movable mirror. The mirror is mounted on a translation stage retro-fitted with a piezoelectric chip stack (Thorlabs PC4QM), allowing for roughly $9\mu\text{m}$ of displacement. First iterations of the set-up used a 3D-printed fiber stretcher, which works by slightly changing the length of a coiled optical fiber using the force of a piezoelectric actuator. We abandoned this system after noticing that it induced enough stress in the fiber to significantly change the polarization of the light. Another advantage of the circulator set-up is that it makes it easier to match the length of the probe and LO path, which is vital in reducing the effects of laser phase noise. The length of the two paths is ultimately matched by adding a fiber patchcord of the same length as the fiber EVOA used in the probe beam, as well as placing the movable mirror at a similar distance from the circulator output to the distance between the probe circulator and the cavity.

The outputs of the probe and LO circulators are collimated into free-space using matching fiber collimators. The two beams are combined into the same path but with perpendicular polarizations using two half-wave plates and a polarizing beamsplitter (PBS). A third waveplate is adjusted in order for a second PBS to act as a 50:50 BS. The outputs of the second PBS are focused to the photodiodes of the balanced detector. We use a homemade balanced detector equipped with high-quantum efficiency ($\eta_{\text{QE}} \geq 0.95$) InGaAs photodiodes (Laser Components). The photodiodes are set in a differential configuration so that the trans-impedance amplifier converts the photocurrent difference into a voltage. The signal is split internally into a low-frequency signal and a high-frequency signal, each signal goes through an additional amplification stage. The circuit has two separate outputs, one for the low-frequency (DC) component and one for the high-frequency (AC) component. The AC signal is recorded in a spectrum analyzer and the DC signal is used to control the relative phase between the probe and LO this is done using a RedPitaya FPGA board with the PyRPL software [64]. The 0-2V output of the RedPitaya is first amplified 3.75V/V using a homemade amplifier⁹, then further amplified to the 0-150V range of the piezoactuator using a high voltage amplifier with gain 20V/V (PiezoDrive PDu150).

⁹A simple non-inverting amplifier using a Texas Instruments LM311 operational amplifier.

3.6.1 Aligning to the microcavity

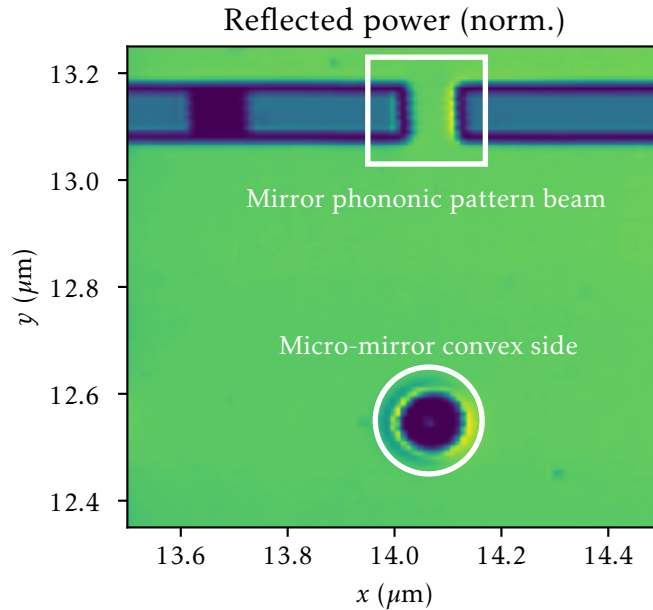


Figure 3.11: Map of the collected power reflecting off the surface of the top mirror. The image has been obtained by scanning the position of the coupling optics using two motorized translation stages.

The task of aligning a beam to a cavity that is only a few hundreds microns in size appeared daunting at first. We quickly found out that, thanks to the geometry of our system, the alignment is straight-forward and can be done in a matter of minutes. The optical set-up that was described in the previous set-up is essentially a confocal microscope when the reflected power is measured directly at the collected output of the circulator. We use the confocal filtering effect to our advantage in order to navigate through the features of the mirror. Basically, the tight curvature of the micromirror will strongly scatter a beam that has been initially focused to the surface of the top mirror. This can be seen in the image in Figure 3.11, which was obtained by mounting the cage with the mode-matching optics to two motorized stages. Equipped with this knowledge, we can align the system without motorized stages. In the following description, X and Y are the axis co-planar with the mirror surface (parallel to the optical table) and Z is the perpendicular. To help illustrate the procedure, the path of the beam's focal spot is drawn in Figure 3.12.

1. The focal point of the beam is placed outside the phononic structure domain. This can be done by eye, then the Z stage, as well as the kinematic mount of the collimator, is adjusted as to maximize light collection. The beam is now focused on the HR side of the top mirror.
2. While tracking the collected power, the X stage is moved towards the center of the mirror. There is an easily noticeable drop in collected power when the beam is in between two squares of the phononic pattern. Once 4 dips in power have occurred on our way to the center, we are in the central column (there are 7 crystal cells). If no dips occur, the starting position was along a the line of beams connecting the phononic cells. In that case, we do

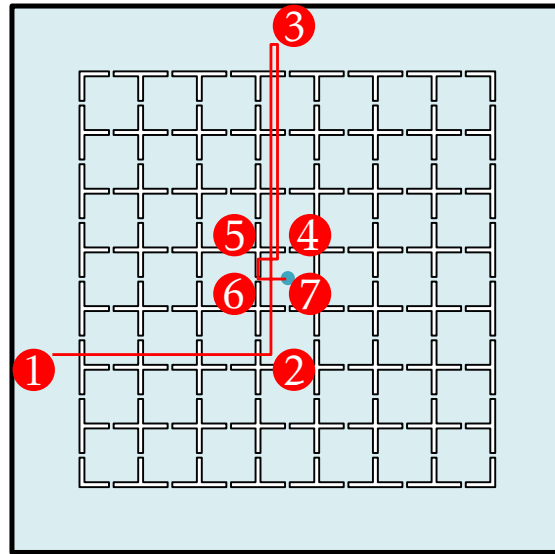


Figure 3.12: Path of the focal spot on the top mirror during the alignment procedure. Each number correspond to the final position at each step of the alignment process detailed in the main text.

a small displacement of Y and repeat.

3. The Y stage is moved so that the focal spot moves away from the center, regular dips in power will be observed as we cross the phononic pattern. Once no more dips occur, we are outside the pattern.
4. We now start moving back towards the center in the Y direction. Once 4 dips have occurred the focal spot is on the central cell.
5. The beam is moved in the X direction away from the center until we see a dip in reflected power, we are now in the space between two cells.
6. The beam is moved in the Y direction towards the center until we see an increase of collected power, we are now on the beam connecting the two cells. We can verify that we are in the beam if we keep moving in the same direction and observe a drop in power. The collected power is maximized by adjusting the Y position to ensure we are centered on the beam.
7. The X stage is moved towards the center until we notice the power decreasing. If the power decreases in a smoother fashion than the dips previously observed, we have placed the beam on the micromirror. The exact center of the micromirror is characterized by a reflection peak because it is parallel to the mirror surface (in Figure 3.11 the center looks faint due to the spatial resolution of the scan). We can adjust X and Y to maximize reflected power. We can ensure we are in the center of the micromirror by moving in either direction, the signal as a function of distance from the center should look like a “W”.
8. Finally, the Z axis is adjusted to maximize the collected power.

Once these steps have been completed, a wide scan of the laser wavelength will reveal transmission peaks and reflection dips corresponding to the optical resonances. The final alignment

can be done by maximizing the transmitted peak.

3.6.2 Alignment to the bottom mirror for transmission measurements

Because the bottom silicon mirror has a higher reflectivity coating than the top mirror, a set-up to measure in transmission should pump the cavity through the bottom mirror. We cannot use the same tricks as described above for two reasons. First, the bottom mirror is completely planar and we have no characteristic behavior when the laser is close to alignment. Second, we have the inconvenience of a large distance (roughly 17.5cm) between the cavity and the bottom viewport of the cavity, as well as a fixed mirror in between.

We have been successful in coupling light to the cavity from the bottom by first aligning the beam from the top as described previously. The laser is left continuously scanning across an optical resonance, so that there is a periodic transmission signal. The transmission detector and accompanying focusing lens is replaced by a large beam collimator (Thorlabs F810APC-1550) mounted on an 3-axis translation stage. Through patient scanning of the collimator's position, the transmission can be coupled into fiber. Now, sending light from the large beam collimator will pump the cavity. The mode-matching achieved in this situation is of a few percent, however, we believe there is much room for improvement as we only tried this method once.

Chapter 4

Micromirror fabrication through laser ablation

In this chapter, I present the concave micro-mirror template fabrication set-up used to create the curved surface on the top mirror. We use a feedback controlled procedure based on real-time collection of the light emitted in laser ablation. We simplify and improve on the set-up by Petrak et al [65]. The standard procedure for laser fabrication of micro-mirror templates uses a CO₂ laser pulsed with repetition rates in the range between 1kHz – 10kHz. Ablation happens when a train of laser pulses are focused on the sample over a time ranging between a few to hundreds of milliseconds. The train of pulses can be generated by direct stimulation of the laser medium [66] or by continuously driving the laser and afterwards selecting pulses using an acousto-optical modulator (AOM) [67]. The former approach results in a large spread (>10%) of the resulting mirror depth and radius of curvature due to unpredictability of laser gain medium response to the excitation. The latter method addresses the problem by maintaining the laser emitting at a fix repetition rate and duty cycle, but is still limited by laser power fluctuations.

Micromirrors of this kind are usually fabricated on the tip of optical fibers. In that case, the repeatability and yield of the process is not very important. If the mirror template is not satisfactory upon inspection, the fiber is cleaved again and the process repeated until the geometry matches the target. In our case, we want to fabricate mirrors at a precise location of an already processed substrate. We need perfect yield in order to not waste substrates. Fabricating multiple mirrors in the same substrate until reaching the desired geometry would make alignment practically impossible.

We show that high yield and low geometry spread fabrication can be accomplished with simple and off-the-shelf electronic components. Through in-situ optical characterization using a phase-scanning interferometer, we reduce the mirror asymmetry by reliably placing the sample at the ablating laser's focal spot. We explore the space of geometries achievable with our set-up and find that it can be used to reliably fabricate shallow structures with adjustable radius of curvature up to a millimeter and down to tens of micrometers.

4.1 Setup

A schematic view of our setup is shown in Figure 4.1. The setup consists of two parts, one part for laser ablation and another part for characterization. The sample, in our case, a square

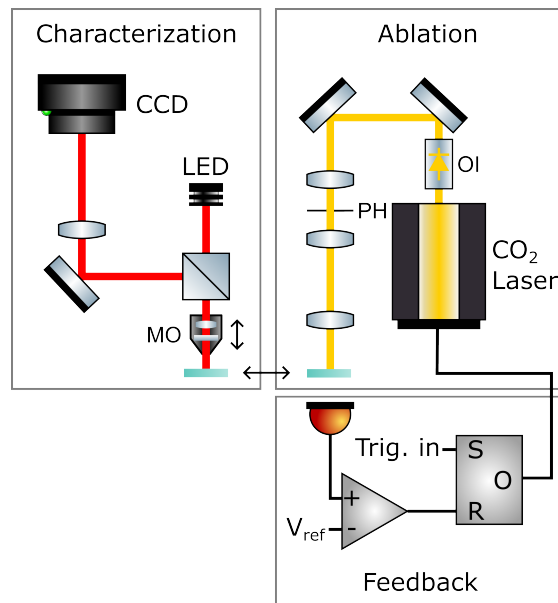


Figure 4.1: Schematic view of the mirror fabrication set-up. The sample is moved using a motorized linear stage from the characterization side, a scanning-phase interferometric microscope, to the ablation part, where the beam of a CO₂ laser is focused on the sample to create a concave indentation. MO: Mirau objective (movable along the optical axis using a piezoelectric stack), PH: pin hole, OI: optical isolator.

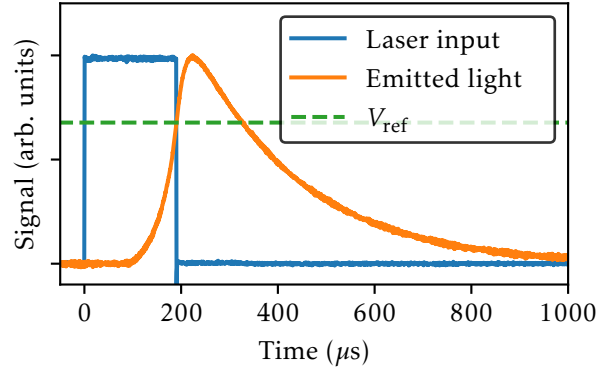


Figure 4.2: Signals recorded during the fabrication of a mirror template. The blue curve is the TTL modulation signal sent to the laser. The orange curve is the white light emission measured by the photodetector behind the target sample. The dashed green line represents the reference voltage used in the voltage comparator.

substrate made of SiO_2 (although a conventional optical fiber can also be ablated), is mounted on a motorized 3-axis translation stage (Physik Instrumente M112.1DG1) allowing for relative movement of the sample and alignment to the focus of the infrared laser beam. An additional motorized long travel range is used to move the 3-axis stage together with the sample from the ablation to the characterization part and vice-versa.

4.1.1 Laser ablation subsystem

In the ablation part, we use the focused beam of a Synrad v40 Firestar CO_2 laser to ablate the surface of the target sample. An optical isolation stage placed in front of the laser is used to remove possible back-reflections from re-entering the laser cavity and potentially causing instabilities. To obtain a near Gaussian beam profile, we use a mode-cleaning telescope consisting of a $300\mu\text{m}$ diameter gold coated pinhole placed in the focal plane between two $f = 50\text{mm}$ plano-convex lenses made of ZnSe. The mode-cleaning telescope is critical to obtaining a circularly symmetric mirror. Finally, the filtered beam is focused onto the sample using a ZnSe lens, where the focal length will partially determine the shape of the ablated areas on the substrate.

Feedback system

As a core element of our setup, we use a real-time feedback system to control the duration of the infrared laser pulse for ablation. As illustrated in 4.1, the feedback utilizes the emission of broadband white light from the sample occurring in the glass ablation process when irradiated with the infrared laser [65]. We monitor the emitted light with a large active area (13mm^2) biased Si photodiode (Thorlabs DET36A/M) which we mounted directly behind the glass substrate. Once the signal of the detector reaches a set value, the CO_2 laser stops and the ablation process finishes.

We implement this protocol with an electronic circuit consisting of two main components: a voltage comparator (TI LM311P) and a Set-Reset latch (TI 74LS279). The implementation we

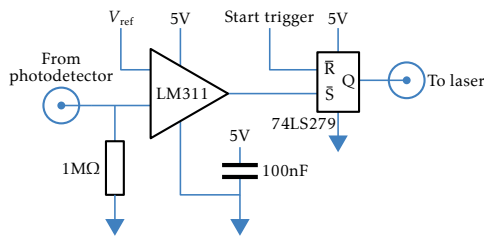


Figure 4.3: **Left:** Simplest yet functional circuit implementing the feedback controlled laser ablation protocol. The circuit implemented is more complex due to added safety features (see main text). **Right:** The physical circuit is encased in an aluminium box with BNC connectors and light indicators. A USB port at the front powers the device and allows for communication between the microcontroller and the computer.

use is a cost-effective alternative to the system implemented in previous work [65] which uses a Field Programmable Gate Array (FPGA) device. The simplification is possible due to our laser implementing its own “tickle” pulse generator, which are a $1\mu\text{s}$ short pulses used to keep the gain medium ionized. The circuit has additional safety features to ensure that the CO_2 laser is not left emitting in CW. After testing the circuit in a breadboard, a custom printed circuit board and aluminium enclosure were designed¹, which are available on GitHub². The feedback circuit board attaches itself to an off-the-shelf development board containing a STM32F303RE microcontroller unit (MCU). The MCU has a digital-to-analog converter, which we use to set V_{ref} . By means of serial communication, we use a computer to set the voltage and trigger the feedback protocol.

The fabrication protocol using feedback proceeds as follows. Ablation starts after a user-generated signal primes the latch into the high logic state, the output drives the laser into emission. The voltage comparator resets the latch to its low logic state once the photodetector signal surpasses a user defined reference voltage. The laser emission stops and the ablation process is concluded. Time traces of the involved signals are recorded by an oscilloscope, an example of which can be seen in Figure 4.2.

4.1.2 Characterization subsystem

The characterization part of the setup is based on a homemade scanning phase interferometry microscope. The key element of the interferometer is a Mirau microscope objective (Nikon CF IC EPI Plan DI 20×A) mounted on a linear translation stage (Thorlabs PT1/M) retrofitted with a piezoelectric chip stack (Thorlabs PC4QM). We use an LED emitting at 617nm (Thorlabs M617L4) to create a magnified interferometric image that we record with a monochrome CCD sensor (Thorlabs) using a $f = 500\text{mm}$ lens. The height profile of the sample can be reconstructed by capturing a series of images at different objective-to-sample distances, which we control using the piezoelectric actuator mounted in the objective base. The objective is scanned approximately $8\mu\text{m}$ along the optical axis.

¹Translating the circuit into a printed circuit board and designing the enclosure was done by the author’s brother. Thanks Guillem.

²<https://github.com/gallepuz/laser-feedback>

Height map reconstruction from scanning phase interference microscopy

The problem of reconstructing a height map from an interferometric image stems from the multi-valued nature of the inverse cosine/sine function. The image obtained in a interferometric microscope is given by:

$$I(x, y) = I_0(x, y) + C(x, y) \cdot \exp\left\{-4\left(\frac{z(x, y) - z_0}{L_{\text{coh}}}\right)^2\right\} \cos\left(4\pi \frac{z(x, y) - z_0}{\lambda}\right), \quad (4.1)$$

where $I_0(x, y)$ is the value of the image at zero contrast $C(x, y)$. $z(x, y)$ is the height of the surface and z_0 the position of the objective. L_{coh} is the coherence length of the light source. The ambiguity when inverting the \cos function may be resolved if we provide some additional information about the height map $z(x, y)$ that we are trying to recover. For example, if $z(x, y)$ is concave or convex at very x, y , the ambiguity is solved. If a good model for $z(x, y)$ is available, we can fit the expected interferometric image to our measured image. In practice, these two methods fail due to the non-uniform nature of the offset $I_0(x, y)$ and contrast $C(x, y)$. This dependence implies that the function connecting $I(x, y) \rightarrow z(x, y)$ is itself a function of x, y .

These problems can be addressed if we capture a sequence interferometric images at different sample to objective distances with the help of the piezoelectric actuator $z_0(v_k)$. The value of the pixel i, j at the voltage v_j is:

$$I(x_i, y_j, v_k) \simeq I_0(x_i, y_j) + C(x_i, y_j) \cdot \exp\left\{-4\left(\frac{z(x_i, y_j) - z_0(v_k)}{L_{\text{coh}}}\right)^2\right\} \cos\left(4\pi \frac{z(x_i, y_j)}{\lambda} + K \cdot v_k\right), \quad (4.2)$$

where I have considered that there is a linear relation between $z_0(v_k)$ and v_k that has been absorbed together with $\frac{4\pi}{\lambda}$ into a constant K . Assuming that the overall change in z_0 is small compared to L_{coh} , the pixel value as a function of v_k is given by a cosine. Without needing to calibrate $I_0(x_i, y_j)$ nor $C(x_i, y_j)$, we extract the value of the phase $4\pi \frac{z(x_i, y_j)}{\lambda}$ using the Fast Fourier Transform (FFT) over v_k .

The set of FFTs at each pixel gives us a phase map in the range 0 to 2π , thus it will present some discontinuities. We can correct by adding or subtracting multiples of 2π using a phase unwrapping algorithm. We use the 2D unwrapping algorithm presented in [68] in order to recover a smooth phase map. The actual height profile of the sample is easily recovered using the wavelength of our light source.

4.1.3 Fabrication procedure

Fabrication is controlled by a computer running a program with a Graphical User Interface (GUI) based on the Qudi software suite [69]. The program communicates with a micro-controller in charge of generating the logic signal that primes the feedback system and the reference voltage used by the comparator. The fabrication of a single feature proceeds as follows:

1. The sample starts in the characterization side. It is brought to the focal point of the interferometric microscope using an auto-focus procedure. Due to the short depth of field of the microscope, its focal point is used as a reference position. Using a live-view of the interferometric image, the user can also position the sample so as to ablate the feature in a precise locatio. In our case, the center of the mirror substrate, but it could be used, for example, to create a dimple on the core of an optical fiber.
2. The sample is moved to the ablation side using the long range stage. Furthermore, the sample is moved a calibrated distance in the three spatial directions so that the point at

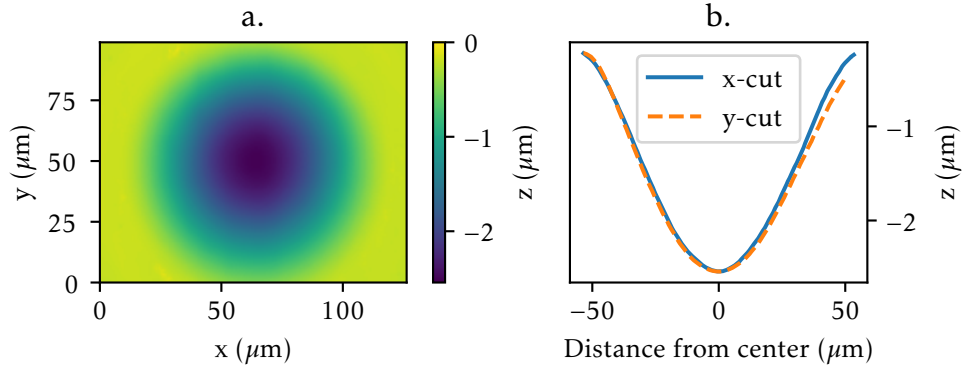


Figure 4.4: (a) Height map of a fabricated feature obtained through phase-scanning interferometry. (b) Height profiles along the horizontal and vertical lines that intercept the center of the feature.

the center of the interferometric image is now placed at the focal point of the CO₂ laser. The calibration was done by performing ablation at different offsets along the optical axis of the ablation laser and manually selecting the offset where the features created were closer to having circular symmetry.

3. The feedback-controlled ablation process is engaged by the micro-controller.
4. The sample is moved back to the characterization side to obtain a height map of the feature. Additionally, the program can estimate the depth and radius of curvature of the fabricated feature.

4.2 Fabrication results

In this section, we discuss the mirror geometries that have been achieved, as well as the performance of the feedback system. The mirror geometries presented in this sections have been fabricated focusing the CO₂ beam with a 100mm focal length lens. This particular focal length has been selected as it results in mirror templates with radii of curvature around 300 μm at a mirror depth of around 2 μm . We find that using a shorter focal length lens creates shallow mirrors with smaller radius of curvature, resulting in low-volume optical cavities which are more suitable for cavity QED experiments. Using a 25mm focal length lens, we are able to reliably fabricate mirrors with radius of curvature down to and about 30 μm .

The geometry of the mirror templates is measured using the phase-scanning interferometric microscope, which is able to reconstruct height profiles with a perpendicular spatial resolution of roughly 100 nm/pixel. The scaling factors have been calibrated by measuring the profiles of atomic force microscope calibration gratings. An example of such a height map is shown in Figure 4.4. The depth d of the feature can be measured directly from the height map. To allow for comparison, we characterize the curvature using the same parameters used in the work [67]. Two curvature radii R_a and R_b are defined to characterize the possible asymmetry of the feature. They represent the radius of curvature along the major and minor axis of the elliptic paraboloid used to approximate the lower part of the mirror. R_a and R_b are obtained by fitting the center

of the height map with the following expression:

$$z(x, y) \propto \frac{1}{2R_a} (x \cos \phi - y \sin \phi)^2 + \quad (4.3)$$

$$+ \frac{1}{2R_b} (x \sin \phi + y \cos \phi)^2, \quad (4.4)$$

where ϕ is the angle formed by the major axis of the ellipse and the horizontal of our image. In following discussions, we use the mean value R.O.C. = $\frac{1}{2}(R_a + R_b)$ as a measure of the radius of curvature. We measure a feature's asymmetry through the quantity $\frac{|R_a - R_b|}{R_a + R_b}$.

4.2.1 Repeatability and yield

The implemented feedback system is shown to reduce the variance of mirror shape on both configurations. Figure 4.5 shows the distribution of depth and radius of curvature of the mirrors with and without feedback. The relative variance, calculated as the standard deviation to mean value ratio, of the mirror depth is reduced from 10% to 3% , and the relative variance of the radius of curvature is reduced from 6% to 3%. The average feature asymmetry is around 3% for both cases. The improvement is due to the feedback system correcting for the unpredictable delay between the trigger pulse sent to the laser and the start of the ablation. This delay has a relative variance of 8%, which has been measured by defining the start time of the ablation as the time when the emitted white light is 10% of its peak value. Without the presence of feedback, this translates to variance of the active ablation time. The delay might be caused by the laser responding to the signal with different rise times depending on the state of the gain medium, which will depend on the temporal proximity to the tickle pulses generated by the laser internal circuitry (1 μ s in length at a 1 kHz repetition rate). Additionally, the delay in ablation might also be caused by residue on the surface of the target substrate. The feedback system is limited by power fluctuations of the laser, which according to the manufacturer are $\pm 3\%$.

Our set-up is completely automatized and can create and characterize mirrors in the same target substrate at an approximate rate of 1 mirror per minute. We have created and measured upwards of 1000 features to characterize our process and did not observe any failed fabrication in the presence of feedback.

4.2.2 Range of geometries

The value of V_{ref} can be tuned to obtain a target geometry. Figure 4.6 (a) and (b) show the wide range of mirror geometries that can be obtained by adjusting the value of V_{ref} . Figure 4.6 (c) shows the verification of the power law relating radius of curvature and depth found in previous work [53, 67]. A wider range of geometries can be accessed by adjusting the power of the CO2 laser (i.e. by means of a polarizer) or adjusting the size of the laser spot using different powered lenses.

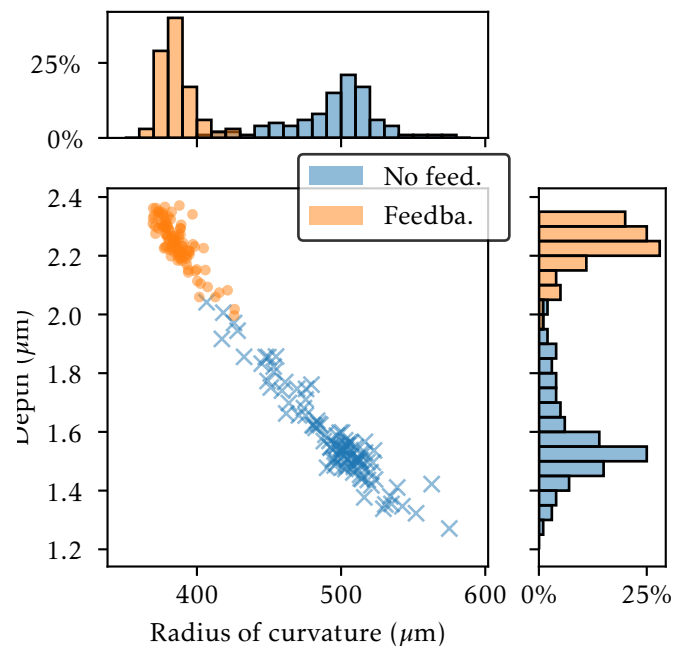


Figure 4.5: Comparison of the geometry distribution of 100 mirrors fabricated without engaging the feedback and in the presence of feedback. In the absence of feedback, the modulation signal to the laser is a square pulse with a constant duration of $184\mu\text{s}$. (a) Distribution of mirror depth. (b) Distribution of radius of curvature.

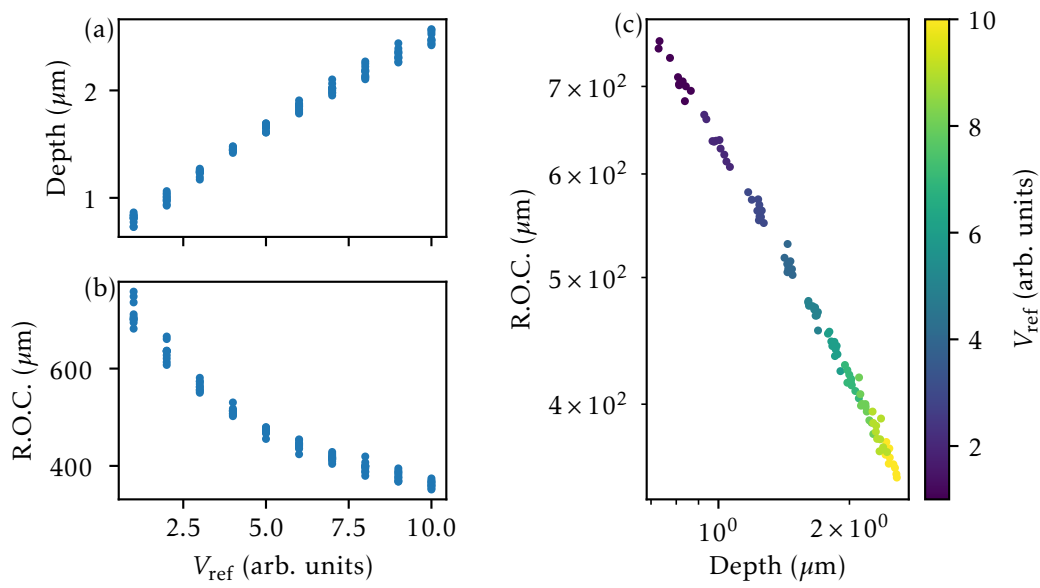


Figure 4.6: Reference voltage V_{ref} dependence of the mirrors' (a) depths and (b) radius of curvature. (c) Given an ablation laser spot size and optical power, the radius of curvature and depth are related by a power law. 10 features have been fabricated at each reference voltage. V_{ref} is expressed in the units of the digital-to-analog converter used.

Chapter 5

Characterization of the cavity optomechanics experiment

In this chapter we present the methods used to characterize the performance of our cavity optomechanics experiment.

5.1 Optical characteristics

5.1.1 Free spectral range, length and mirror curvature

The characterization of the optical properties of the MIM system starts by determining the free spectral range (FSR) of the cavity. The laser is scanned at a rate of 1nm s^{-1} in the range accessible by our main laser, from 1510nm to 1630nm , while recording the transmission signal. Such a scan can be seen in Figure 5.1, where the FSR has been extracted from the periodicity of the resonances. The size of the cavity inferred from the FSR is $126\mu\text{m}$, which is within the tolerances of the spacers used.

The resonant frequencies of higher order Hermite-Gaussian modes, which are the lower amplitude peaks left to each fundamental mode in Figure 5.1, give information about the curvature of the concave mirror. The difference in resonant frequency of higher order HG modes is due to their accumulated Gouy phase being different after one cavity round-trip. This extra phase depends on their mode number $m+n$ and their waist size w_0 , which results in the distance in frequency between the HG_{00} peak and a HG_{mn} peak being a function of the ratio of cavity length L to radii of curvature, R_1 and R_2 . The frequency shift is given by the following expression[34]:

$$\Delta\omega_{m,n} = \frac{\omega_{\text{FSR}}}{\pi}(m+n)\arccos\sqrt{\left(1 - \frac{L}{R_1}\right)\left(1 - \frac{L}{R_2}\right)}. \quad (5.1)$$

It is thus straightforward to obtain a value for R_1 , knowing that $R_2 = \infty$ (planar mirror) and assuming that the peak closest to our HG_{00} is first order HG mode ($m+n=1$). The resulting curvature is $R_1 = 267 \pm 9\mu\text{m}$, with the uncertainty given by different spacing at each resonance¹. With this information, we infer that the cavity mode has a waist size of $w_c \simeq 8\mu\text{m}$.

¹I used the same method when characterizing a focusing metamirror during a stay in Prof. Dalziel Wilson's group at the University of Arizona, the work can be found in [39].

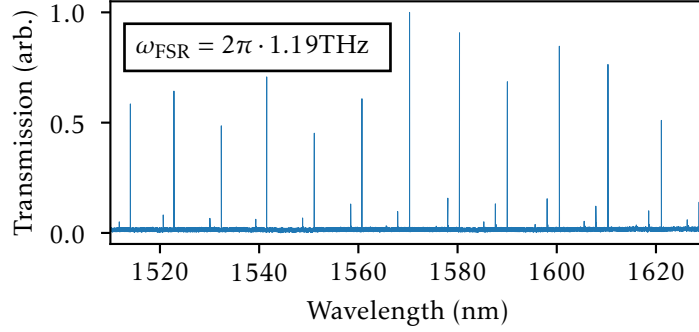


Figure 5.1: Cavity transmission recorded as the laser’s wavelengths is scanned 120nm around 1570nm. The laser pumping the cavity has been intentionally misaligned in order to measure the position of the resonances with higher-order spatial modes. The FSR of 1.19THz implies a cavity length of 126 μ m.

5.1.2 Optical linewidth and birefringence

Most cavity optomechanical phenomena depend strongly on the the cavity decay rate κ and thus it should be thoroughly characterized. Ideally, a straight forward way of determining κ is to measure the FWHM of the Lorentzian resonance peak in reflection or transmission, in practice, one must be careful when fitting the peak.

The first effect that we have observed modifying the shape of the resonance peak is birefringence. Our MIM system behaves like a cavity formed around a birefringent medium: there are two different FSRs for two principal polarization axes. When the input beam’s polarization is not aligned to one of the two principal polarizations, two peaks appear in the reflection/transmission spectra. The birefringence in our system was found by noticing how a lorentzian model did not fit well the transmitted resonance. Due to the shift between polarizations being smaller than κ , the two peaks are joint and appear as a non-lorentzian line shape. Luckily, we could characterize the birefringence because the shift it causes is amplified for higher HG modes, as it can be understood from Equation 5.1. In modes with orders $m + n = 1$ and $m + n = 2$, two peaks are observed due to the shift being larger than the linewidth. The shift was measured by creating 500MHz phase modulated sidebands on the input beam. The transmission resonance present six peaks, two for each polarization and four sidebands, the frequency axis can be calibrated through the spacing between carrier and sideband resonances. The split in a $m + n = 1$ resonance at 1520.8nm was measured to be 136MHz and in a $m + n = 2$ mode at 1518.7nm was 241MHz. The birefringence is also present in the empty cavity, indicating that it probably originates from asymmetry in the mirror’s curvature, this is supported by the slight asymmetry seen in the height profiles of the micro mirrors (Figure 4.4). An alternative explanation is birefringence arising in the HR coatings[70–72]. We remove the problem of birefringence by aligning the polarization of the input beam to one of the principal axes. This will work as long as we do not need to keep resonant two beams originating in the same laser but with perpendicular polarization.

Despite suppressing the effects of birefringence, the observed line shape was still poorly fitted by a Lorentzian. This is due to the limited scan speed of our laser and the high-cooperativity achieved even at low input powers. Phonon lasing taking place while scanning through the blue

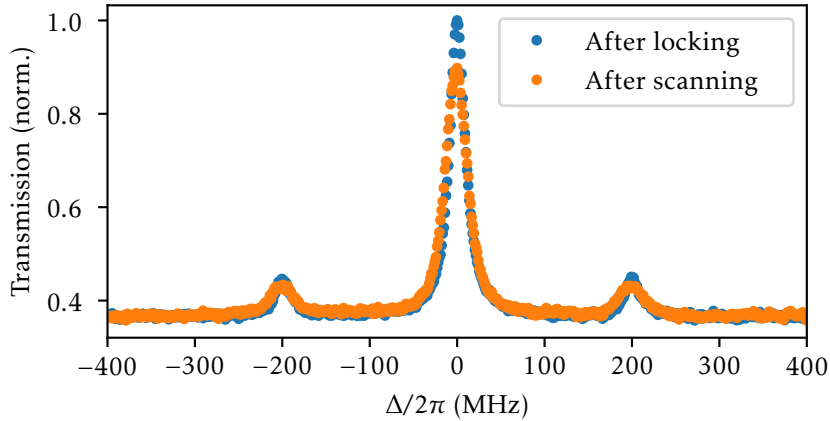


Figure 5.2: Transmission resonance obtained by scanning the laser frequency around $\lambda \approx 1551.1\text{nm}$. The frequency axis has been calibrated using phase sidebands at 200MHz. The blue trace is obtained shortly (around 100ms) after keeping the laser locked at $\Delta \approx -\kappa$. The orange trace is obtained after the laser has been scanning continuously for tens of seconds.

side of the resonance is strong enough to modify the line-shape. This effect manifests itself clearly when comparing the two following situations. In the first situation, the laser is continuously scanned across the resonance until we record one of the scans to measure the linewidth. In the second one, the laser is kept locked at the red side of the resonance until we record a single frequency scan. There is an appreciable difference in the line-shape, as it can be seen in Figure 5.2. In this particular resonance and input power, the difference in measured linewidth is of 7MHz, equivalent to a drop of more than 10000 in measured finesse.

We have measured κ at all the resonant wavelengths accessible by our laser. We have measured the linewidth with and without a membrane. This has been done with exactly the same cavity assembly thanks to the membrane rupturing (see Section 6.1). In Figure 5.3 we observe a general trend given by the reflectivity dependence of our mirror coatings. The linewidth of the loaded system is generally higher than the empty cavity linewidth. Super-imposed on the mirror reflectivity curve we see the behavior expected from our simulations of the MIM system done in Section 2.5. The MIM model also predicts a correlation between the the strength of the optomechanical coupling $|G|$ and the difference of κ respect to the empty cavity behavior. Thus, the jumps in κ observed for lower wavelengths indicate a larger $|G|$. Both the maximum finesse in the loaded cavity (≈ 62000) and empty (≈ 65000) are above the finesse expected from the nominal value of the coatings provided by the company that coated the substrates (≈ 5800), we believe this is caused by either an underestimation of the FSR or by an incorrect nominal reflectivity². This is not of great importance as the linewidth is the relevant parameter in the behavior of the system.

²The company could not guarantee the values of reflectivity for non-standard substrates

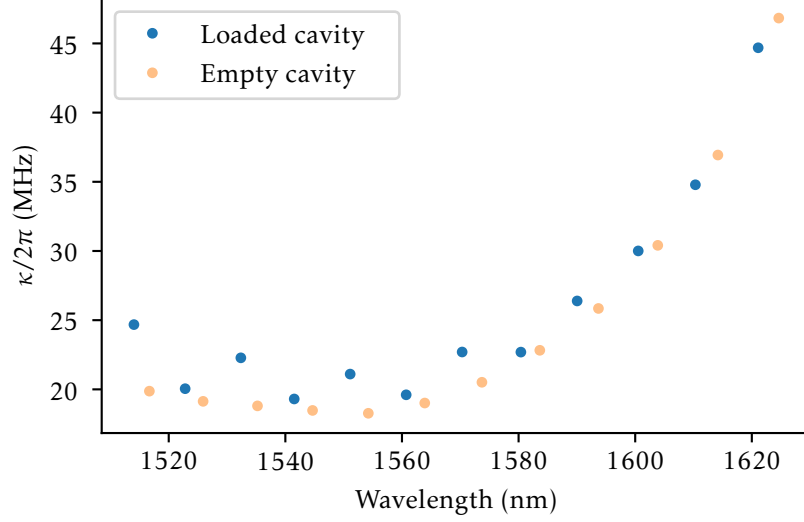


Figure 5.3: Linewidth of the resonant modes of the cavity that are accessible by our laser. In blue, measured with a membrane in the middle, in faint orange, the empty cavity linewidth. The cavity has not been reassembled in order to include/remove the membrane. Rather, the empty cavity linewidth was measured after the membrane ruptured inside the cavity. The empty cavity linewidth reaches its minimum around the design wavelength of the high-reflectivity coatings (1550nm), while the the loaded cavity does not due to the finesse enhancing/reducing effect of the membrane in the middle.

5.2 Mechanical quality factor

The damping rate of the mechanical oscillator can be determined by driving it with a modulated force close to its frequency. After turning the excitation off, the resonator will *ringdown*, its energy will decay exponentially until it comes back to its thermal equilibrium. In a cavity optomechanical system, the decay rate observed in a ringdown is given by the bare mechanical damping rate Γ_m modified by dynamical backaction. In the red-detuned regime, the decay rate is larger ($\Gamma_m^{\text{opt}} > 0 \Rightarrow \Gamma_{\text{eff}} > \Gamma_m$) and in the blue-detuned regime is smaller ($\Gamma_m^{\text{opt}} < 0 \Rightarrow \Gamma_{\text{eff}} < \Gamma_m$) and possibly negative in the case of phonon lasing ($|\Gamma_m^{\text{opt}}| > \Gamma_m$). Dynamical backaction only disappears when the cavity is pumped on resonance $\Gamma_m^{\text{opt}} = \Gamma_m$.

Characterization of the bare mechanical rate Γ_m is crucial because it will determine the cooperativity in our system. We therefore need to somehow remove the effect of dynamical backaction. Ideally, Γ_m can be found pumping the cavity at $\Delta = 0$ because it ensures no enhancing of the decay rate. In practice, the dynamical backaction in a high cooperativity system is extremely difficult to get rid off. The contribution caused by any small deviation from $\Delta = 0$ greatly overwhelms the bare damping rate due to how small it is ($\Gamma_m \approx 10\text{mHz}$).

There are different approaches to the problem. An option is to completely avoid the problem by measuring the resonator's Γ_m prior to being put in the optical cavity (through interferometry). The challenge is that the conditions in the experiment to determine Γ_m might be different

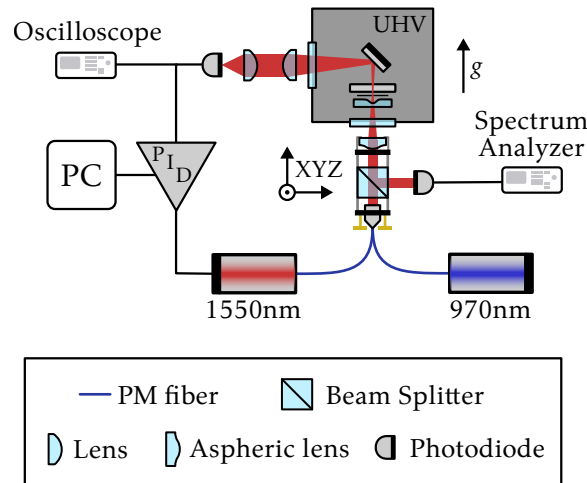


Figure 5.4: Set-up configuration used for ringdown measurements. The 1550nm laser (red) is aligned to the MIM system while the 970nm laser (blue) propagates along the same path. PID: Proportional-Integral-Derivative controller, PC: Experiment computer. UHV: Ultra-High Vacuum (vacuum chamber)

than in the cavity. It is possible to compensate for some of these conditions, such as pressure [52], but it is impossible to take into account any possible degradation of the resonator's quality factor when being moved from experiment to experiment. Another option is to reduce the effect of dynamical backaction by performing the ringdown at $\Delta \ll \kappa$, ideally at a low-cooperativity resonance mode. For example, in the work by Huang et al[27], a laser with wavelength far from the mirror coating optimum is used. By performing ringdowns at progressively lower intracavity photon number, one can extrapolate the bare mechanical damping rate.

None of these approaches are satisfactory in our experiment. Although the first option presented might be possible, the quality factor of the resonator used was determined through interferometry prior to being diced from its silicon wafer. It is not realistic to assume that the dicing process will leave the damping characteristics untouched. The second option is challenging due to the large G and broadband reflective coatings of our cavity, we can't access any cavity resonance mode that ensures a cooperativity low enough, with all the resonances accessible by our experiment laser having finesses above 27000.

The unique geometry of our experiment allows for a third option. A laser far from the HR coating optimum will transmit through the top fused silica mirror, a small fraction will reflect off the membrane while a considerable fraction will reflect off the bottom silicon mirror, as silicon has a high refractive index for the visible and near-infrared range. Due to the close distance of around $60\mu\text{m}$ between the bottom mirror and the membrane, we effectively have a readily aligned interferometer. First a 1310nm laser (electrical to optical converter) was used, the thermomechanical motion could be detected in transmission. The signal was unreliable, the SNR changing with time due to the etalon effect of the silicon substrate and the fluctuating wavelength of this particular laser. A lower noise laser at this wavelength would be the ideal solution as it propagates in a similar manner to the main wavelength. The second and successful attempt was using a wide-tunable diode laser (Toptica CTL 950) set at a wavelength between 970nm and 980nm.

The experiment was modified in the way shown in Figure 5.4. The main experiment laser,

tuned around 1550nm, is aligned to the cavity and its frequency can be locked to a cavity resonance using the transmission signal. Using a fiber splitter with design wavelength at 1550nm (Thorlabs PN1550R2A2), the beam of the 970nm laser is combined into the same path. A 90:10 beam splitter cube (designed for 1550nm, with a splitting ratio of roughly 70:30 at 970nm) is used to collect reflection from the cavity, which is measured with a large area InGaAs photodetector (Thorlabs PDA20CS2). Due to the high absorption of silicon at 970nm, a negligible amount of the non-resonant beam transmits through.

The ringdown measurement proceeds as follows:

1. The main laser is off. The non-resonant laser is on, with a power around 1mW reaching the MIM system. The reflection detector connected to the spectrum analyzer is used to record the thermomechanical motion. A zero frequency span measurement is centered at the mechanical frequency³.
2. The main laser is turned on and locked to the blue side of the resonance. The lock is stable for a few tens of seconds when using a small amount of resonant light (around 1μW). The mechanical resonator's energy grows due to phonon lasing, which can be observed through the signal measured in the SA.
3. After a few seconds, the oscillation is large enough for the optical resonance to split and the lock becomes unstable. At this point, the main laser is turned off.
4. With only the non-resonant laser present, no dynamical backaction is possible and the resonator losses energy according to its bare mechanical damping rate.

A time domain recording of the signal during the protocol can be seen in Figure 5.5a. A recording of just the ringdown section, such as the one shown in Figure 5.5b, allows us to measure Q and Γ_m . The exponential decay in logarithmic scale is a linear function of time, which we can fit using the following convenient equation[58]:

$$\Gamma_m = \frac{\log 10}{10} \frac{ds_{dB}}{dt}, \quad (5.2)$$

where s_{dB} is the signal in decibels as measured by the SA.

5.3 Strength of the optomechanical interaction

Different parameters defined along the previous chapters can be a figure of merit of the optomechanical interaction. The displacement to cavity frequency shift parameter G could be used, but it does not take into account the nature of the oscillator. For example, a short cavity with centimeter-sized off-the-shelf mirrors will have a large G , but due to the small zero point fluctuation of the mirrors, will not easily show quantum behavior. The single-photon optomechanical rate $g_0 = Gx_{z.p.}$, which is introduced in order to write the optomechanical Hamiltonian in terms of phonon creation and annihilation operators, is a better figure of merit, as it takes the "quantumness" of the resonator into account. Nevertheless, a cavity of very low finesse would still have a large g_0 and, crucially, so would a resonator with low quality factor.

As we have seen in Chapter 2, the light enhanced coupling rate g is the crucial parameter for predicting the dynamics of the optomechanical system in the linearized approximation. Additionally, as discussed at the start of Chapter 3, the quantum cooperativity C_q is the most

³In a zero-span measurement, the spectrum analyzer mixes the input signal with a singular frequency and applies a low-pass filter to the resulting signal. This results in a measurement of power at that particular frequency, which can be recorded as a function of time.

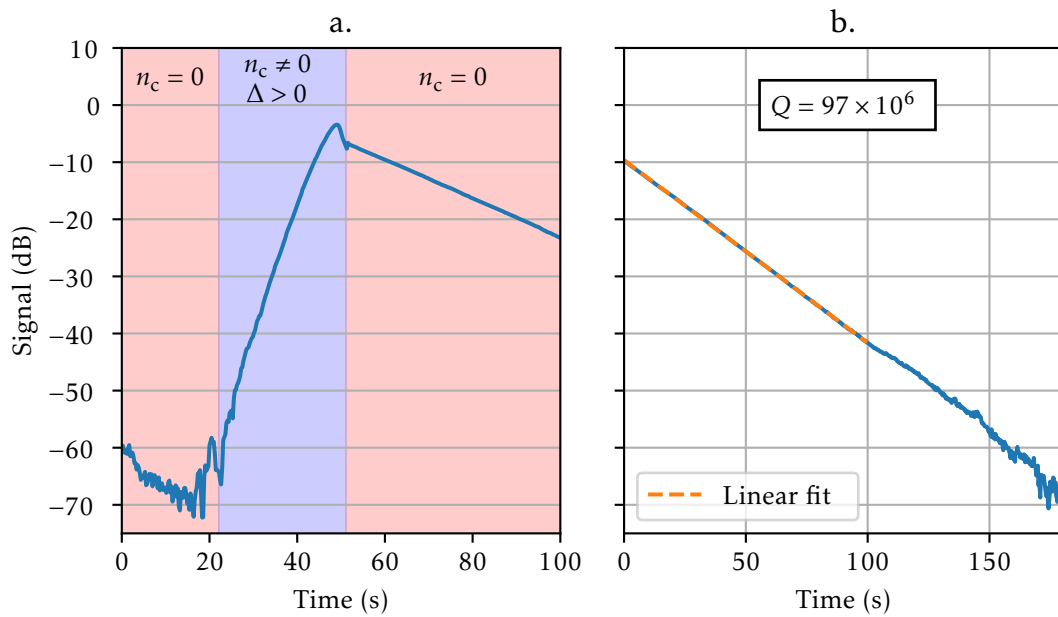


Figure 5.5: Ringdown measurement of the mechanical quality factor. **a.** Signal of the mechanical motion measured with the off-resonant wavelength. The ringdown protocol starts with the resonant laser off, once it is turned on around 20s into the measurement, the mechanical signal grows exponentially due to the resonant laser being blue-detuned. At around 50s, the laser lock becomes unstable and the laser is turned off. Without intracavity photons, the resonator loses energy at its bare damping rate. **b.** Ringdown measurement using the third section of the data shown, the quality factor is extracted from the linear fit.

relevant figure of merit for the presence of quantum effects. In this section, we will measure both using the optical spring effect. Even though g_0 is not the ideal figure of merit, it is still an important parameter to characterize, as we discussed in Subsection 3.1.1, the larger the g_0 , the more immune our measurement is to laser phase/frequency noise. Once C or g are known, the predicted phonon occupation of the resonator can be estimated. With this information, g_0 can be estimated through comparing the area under the mechanical peak with the area under the peak of a calibrated phase tone [73]. Unfortunately, due to time constraints, we have not been able to include such measurements in this work.

5.3.1 Measurement of cooperativity through the optical spring effect

The cooperativity C and the light-enhanced coupling rate g can be determined through the measurement of the optical spring effect, the change of mechanical frequency due to dynamical backaction that we described in Subsection 2.6.3. Using the quantum Langevin equations, we found that the shift mechanical frequency due to the optical spring effect in the sideband unresolved regime ($\Omega_m \ll \kappa$) takes the following form:

$$\delta\Omega_m \simeq g^2(\Delta) \frac{2\Delta}{\kappa^2/4 + \Delta^2}, \quad (5.3)$$

where I emphasize that, at constant input power, g is a function of Δ due to the intracavity photon number n_c depending on detuning. We can make the dependence explicit and find an expression as a function of the g achieved on resonance:

$$\delta\Omega_m(\Delta) = g^2(\Delta = 0) \frac{8\Delta}{\left(\kappa + \frac{4\Delta^2}{\kappa}\right)^2}. \quad (5.4)$$

We now have a straight-forward experimental procedure to obtain g , we lock our laser at different Δ and record the shift in the observed mechanical frequency. With knowledge of κ , we can fit the behavior using the above expression to obtain $g^2(\Delta = 0)$. $g^2(\Delta \neq 0)$ can be extrapolated using the Lorentzian dependence of n_c on κ . In practice, the optical spring effect is not the only phenomenon that changes the mechanical frequency as a function of intracavity power, making this method unreliable. We observe an additional change of mechanical frequency that we attribute to photothermal heating. This has been observed in similar MIM systems [28].

Fortunately, it is possible to devise a simple experimental procedure that keeps the intracavity power resonant while changing the detuning. By keeping the transmission lock signal at a constant value and increasing the input power, the locking system will detune the laser in order to stay on the target transmission. The procedure goes as follows:

1. A reference transmission peak is measured at a certain input power P_0 .
2. The laser is locked at a small detuning $\Delta \approx -0.1\kappa$ using a side-of-fringe lock.
3. The membrane is left to thermalize for sufficient time, the mechanical peak frequency can be tracked through the thermalization to ensure that it has reached its equilibrium.
4. The input power is increased step by step, measuring the cavity reflection through homodyne detection in order to determine the mechanical frequency shift. Through prior calibration of the electronic variable optical attenuator used, the ratio P_i/P_0 is known at each power P_i used. Using the transmission peak measured in step 1 and knowing P_i/P_0 , we can determine Δ at each step.

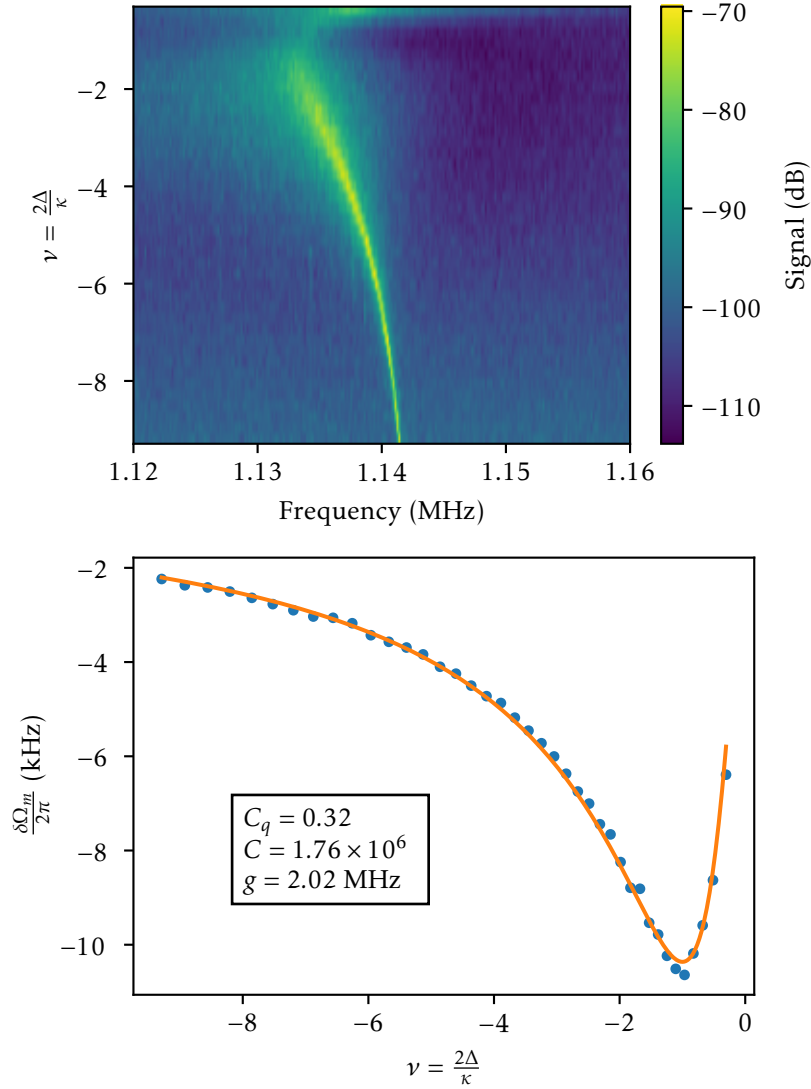


Figure 5.6: Measurement of the optical spring effect. **Top:** Homodyne signal spectra recorded in order to track the mechanical frequency shift at different detunings. Each row of the image is a spectrum at a different detuning but at constant intracavity power. **Bottom:** The shift in mechanical frequency identified from the spectra above. The data has been fit with the expression found in Equation 5.5, with the two free-parameters being Ω_m and the factor $\Gamma_m C$. The estimates for C and C_q are found considering a quality factor of $Q = 97 \times 10^6$ and g from the optical mode's linewidth $\kappa = 2\pi \cdot 20$ MHz.

The protocol can be followed using the relative detuning $\nu = \frac{2\Delta}{\kappa}$ and fitting the following expression of the frequency shift:

$$\delta\Omega_m = \Gamma_m C \frac{\nu}{1 + \nu^2}, \quad (5.5)$$

with our knowledge of Γ_m (obtained through ringdown), we obtain a value of the cooperativity C without knowledge of κ . The quantum cooperativity is simply obtained by its definition $C_q = C/n_{\text{th}}$ using $n_{\text{th}} \simeq \frac{k_B T}{\hbar\Omega_m}$. This is quite remarkable: the optical spring effect allows us to determine if our cavity optomechanical system is in the quantum regime with no calibration of cavity parameters.

An example of the optical spring effect at constant intracavity power is shown in Figure 5.6. Once the cooperativity has been determined for a given transmission level, we can estimate the transmission level necessary for reaching $C_q \gtrsim 1$ through the linear relation between transmitted power and intracavity photon number, and the linear relation between cooperativity and the latter. A value of g can be inferred from this measurement, the cavity linewidth and the quality factor.

At this cooperativity, the resonator is strongly cooled by dynamical backaction cooling. The phonon occupation can be estimated using the following expression [25]:

$$n_f = \frac{\Gamma_m^{\text{opt}} n_{\text{min}} + \Gamma_m n_{\text{th}}}{\Gamma_m + \Gamma_m^{\text{opt}}}, \quad (5.6)$$

where Γ_m^{opt} is the damping cause by back-action found in Equation 2.103 and n_{min} is the minimum phonon occupation achievable given our cavity's linewidth:

$$n_{\text{min}} = \frac{\kappa}{4\Omega_m} \simeq 4.4. \quad (5.7)$$

The maximum reduction of phonon occupation happens a $\Delta = -\kappa/2$. With the cooperativity found, that implies a final occupation of:

$$n_f \simeq 31.8, \quad (5.8)$$

equivalent to an effective temperature of 1.7 mK.

5.4 Laser noise

Ideally, the only fluctuations in coherent beams are due to the fundamental quantum fluctuations. In practice, lasers can have both amplitude and phase noise that are above those of a coherent beam due to classical processes. In this section, we characterize the noise of our laser. We check that it is quantum limited in amplitude around our frequency of interest while exhibiting broadband excess phase noise.

5.4.1 Laser amplitude noise

When we measure the power of a laser, the photodetected fluctuations might be above the quantum fluctuations. The beam of a laser might exhibit excess amplitude noise in some frequencies while being shot noise limited in others, usually, shot noise operation is possible for frequencies above a threshold. Fortunately, it is straightforward to check if a beam is shot noise limited using direct detection.

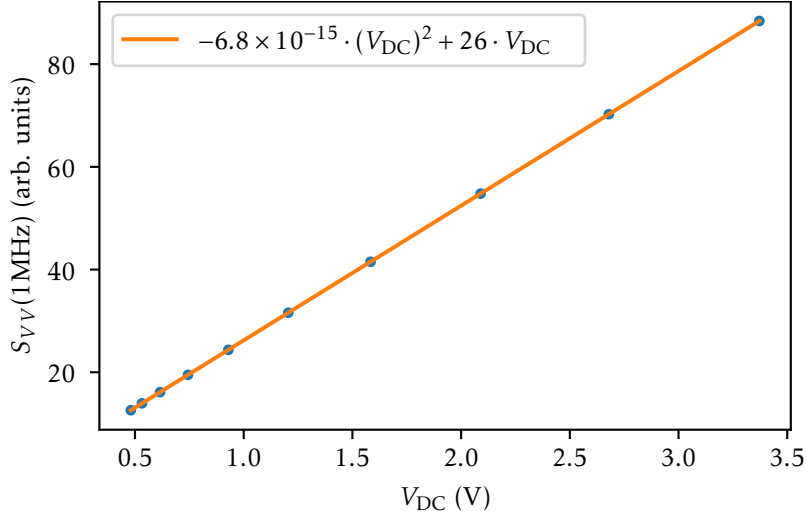


Figure 5.7: Signal fluctuations as a function of the mean value. In the horizontal axis, V_{DC} is the average voltage recorded, which is itself proportional to power. The vertical axis corresponds to the magnitude of the power spectral density of the voltage at 1MHz. A second-degree polynomial has been fit to the data, the negligible quadratic term indicates that the beam is shot noise limited in amplitude.

Consider a beam with classical amplitude noise $\delta\tilde{X}$, it will have the following amplitude quadrature PSD:

$$S_{\tilde{X}\tilde{X}}(\omega) = \frac{1}{2} + S_{\tilde{X}\tilde{X}}(\omega), \quad (5.9)$$

and it goes through an attenuator with adjustable transmission η before arriving at a photodetector. This is the exact model of direct detection discussed in Subsection 2.7.1, using Equation 2.136, we find that the PSD of the photocurrent is:

$$S_{ii}(\omega) = |\alpha|^2 \cdot \eta + 2|\alpha|^2 S_{\tilde{X}\tilde{X}}(\omega) \cdot \eta^2. \quad (5.10)$$

As we change the power of the beam by changing η , we will see a linear behavior if the beam is shot-noise limited and a quadratic behavior if not. We have used this protocol to confirm that our laser is shot-noise limited at frequencies around 1MHz. The results of varying the attenuation and measuring the fluctuations are shown in Figure 5.7. The data has been fit with a second-degree polynomial, the almost zero contribution of the quadratic term indicates that the laser is indeed shot noise limited around 1MHz.

5.4.2 Laser phase noise

Diode lasers are known to have phase noise well above the quantum noise [74], even at frequencies above 1GHz [75]. The phase noise of a laser can be measured through different methods. One may use the quadrature rotation in optical cavities to convert phase into amplitude, the amplitude can then be measured through direct detection [75]. Another way, known as delayed self-heterodyne interferometry, consists of a Mach-Zender interferometer where one arm is made longer as to introduce a delay T (for example, see [51]). Classical amplitude noise can

be canceled using balanced detection, which gives an advantage over the quadrature conversion technique. We have built such an interferometer, shown in Figure 5.8, in order to characterize the phase noise of our laser.

First, let us see how the spectrum of the signal relates to the spectrum of the phase noise. The phase fluctuation prior to entering the interferometer is:

$$\phi(t) = \phi_n(t) + \phi_m(t), \quad (5.11)$$

where ϕ_n is the laser phase noise and $\phi_m(t) = \beta \sin \omega_m t$ is a modulation added by a phase modulator located at the laser output. The modulation will allow us to calibrate the recorded spectrum. After the two paths, the delayed and non-delayed, are recombined at the first PBS, they interfere at each output port of the second PBS. This results in a difference photocurrent $i(t)$ of the balanced detector:

$$i(t) \propto \phi(t) - \phi(t - T), \quad (5.12)$$

when the DC relative phase between the two beams is set to 90 deg. The symmetrized PSD of the signal is:

$$\bar{S}_{ii}(\omega) \propto 4 \sin^2\left(\frac{\omega T}{2}\right) \bar{S}_{\phi\phi}(\omega) \quad (5.13)$$

we see that for a given T , $\bar{S}_i(\omega)$ will carry more or less information about $\bar{S}_{\phi}(\omega)$ depending on our analysis frequency ω . At frequencies $\omega = 2\pi/T$, the factor is zero and $\bar{S}_i(2\pi/T)$ is given by imprecision noise. We can define a transfer function $\mathcal{K}(\omega) \propto 4 \sin^2\left(\frac{\omega T}{2}\right)$ in order to write:

$$\bar{S}_{ii}(\omega) = \mathcal{K}(\omega) \bar{S}_{\phi_n\phi_n}(\omega) + \mathcal{K}(\omega) \bar{S}_{\phi_m\phi_m}(\omega) + \bar{S}_{\text{imp}}(\omega) \quad (5.14)$$

where $\bar{S}_{\text{imp}}(\omega)$ incorporates all other noises (electronic, shot-noise of the beams, etc). \mathcal{K} can be calibrated at ω_m by recording a spectrum with $\beta \neq 0$ and another spectrum $\bar{S}_i^{\beta=0}$ when the modulation is off:

$$\mathcal{K}(\omega_m) \simeq \frac{\int_{\omega_m-\delta\omega}^{\omega_m+\delta\omega} \bar{S}_i(\omega) d\omega - \int_{\omega_m-\delta\omega}^{\omega_m+\delta\omega} \bar{S}_i^{\beta=0}(\omega) d\omega}{\pi\beta^2}, \quad (5.15)$$

where $\delta\omega$ is chosen small enough so that the following approximation is valid:

$$\int_{\omega_m-\delta\omega}^{\omega_m+\delta\omega} \mathcal{K}(\omega) \bar{S}_{\phi_m}(\omega) d\omega \simeq \mathcal{K}(\omega_m) \int_{\omega_m-\delta\omega}^{\omega_m+\delta\omega} \bar{S}_{\phi_m}(\omega) d\omega = \mathcal{K}(\omega_m) \pi\beta^2. \quad (5.16)$$

Once $\mathcal{K}(\omega_m)$ is known, it can be extended through:

$$\mathcal{K}(\omega) = \mathcal{K}(\omega_m) \cdot \frac{\sin^2\left(\frac{\omega T}{2}\right)}{\sin^2\left(\frac{\omega_m T}{2}\right)}, \quad (5.17)$$

where T can be measured precisely from the dip in $S_i(\omega = 2\pi/T)$.

The PSD of the phase noise of our main experiment laser was determined through the procedure described above. The interferometer shown in Figure 5.8 was used to first record an uncalibrated spectrum, show in Figure 5.9a. The calibration tone modulation depth was determined following the procedure described in Appendix F. The calibrated PSD of the phase and frequency noise⁴ is shown in Figure 5.9b. Around the frequency of our mechanical resonator: $\bar{S}_{\phi}(\Omega_m) \simeq 3.6 \times 10^{-9} \text{ rad}^2/\text{Hz}$ and $\bar{S}_{\omega_l}(\Omega_m) \simeq 1.8 \times 10^5 \text{ Hz}^2/\text{Hz}$

⁴The instantaneous laser frequency fulfills $\omega_l(t) = \bar{\omega}_l + \dot{\phi}(t)$, thus, by properties of the Fourier transform: $\bar{S}_{\omega_l}(\omega) = \omega^2 \bar{S}_{\phi}(\omega)$

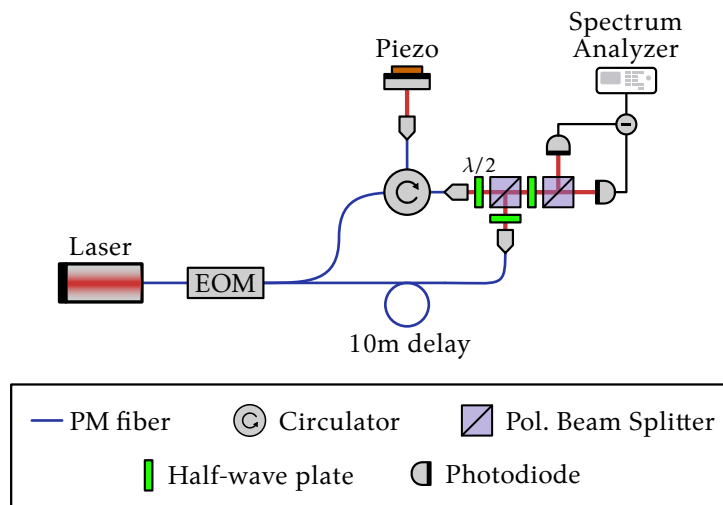


Figure 5.8: The phase noise of a laser can be measured by interference with a delayed fraction of itself. The laser output is split into two beams, one is delayed by 10m of fiber, the other not. The phase of one of the beams is adjusted with a mirror mounted on a piezo. The beams are recombined in a first polarizing beamsplitter (PBS). Interference happens at each of the outputs of the second PBS, which are recorded in the balanced detector. The electro-optical modulator (EOM) at the output of the laser is used to add a known phase modulation, its signal is used to calibrate the spectrum recorded by the spectrum analyzer and the fast analog-to-digital converter (ADC).

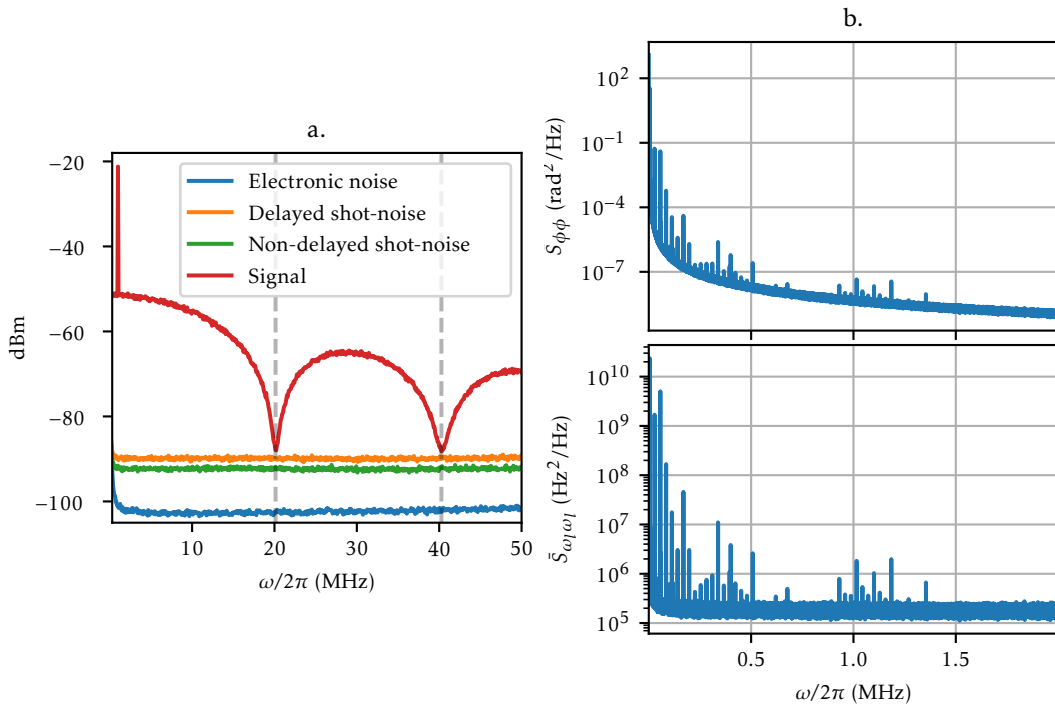


Figure 5.9: Laser phase noise measurements. **a.** Uncalibrated spectrum recorded with the spectrum analyzer. The signal (red trace) is well above the shot noise of each path (orange and green trace obtained by blocking each path), which in turn is well above the electronic noise (blue trace obtained by blocking both paths). The dashed gray lines indicate the dip locations given by the condition $\omega = 2\pi/T$, from which a delay $T = 49.6$ ns is inferred, matching with 10 meters of fiber with a refractive index of 1.5. The peak at 1 MHz is the calibration tone with modulation depth $\beta = 0.261$. **b.** PSDs obtained from 10, 2s-long time-traces recorded at a 50MSample/s. Top plot: calibrated PSD of the laser phase noise. Bottom plot: calibrated frequency noise of the laser.

Chapter 6

Experimental challenges in the high-cooperativity regime

We have built a system that, on paper, can easily reach a quantum cooperativity beyond unity. Indeed, if we look at the measured values of $\kappa \simeq 2\pi \cdot 20\text{MHz}$ and $\Gamma_m \simeq 2\pi \cdot 10\text{mHz}$, assuming a conservative $g_0 \simeq 2\pi \cdot 100\text{Hz}$ ¹, the input power required for $C_q = 1$ is around $100\mu\text{W}$ using the higher transmission port and around 1mW using the lower transmission port. The laser used in this experiment, as well as most lasers, can easily provide such powers. Unfortunately, there are a series of phenomena that challenge or prevent us from operating in a high-cooperativity regime. In this chapter, we discuss such obstacles.

6.1 Membrane rupture

The membrane has ruptured while operating the system at high input powers in two different occasions. A before and after picture of the system can be seen in Figure 6.1. In the first occasion, a high power probe above 5mW was accidentally scanned across a high-finesse optical resonance. In the second occasion, the membrane characterized in the previous chapter ruptured while trying to reach $C_q \simeq 1$ in a low-finesse mode at $\lambda \simeq 1620\text{nm}$. The first rupture was identified due to a big drop in the finesse, which we associate with fragments of silicon-nitride depositing on the mirror surfaces. The second, identified by the lack of mechanical signal, was not accompanied by a drop in finesse.

We suspect that the static optical force can break the membrane by increasing its tensile stress above its yield stress. When a material reaches its yield stress, it stops manifesting elastic behavior and acts as a plastic. This breaks the pre-stressed suspended silicon-nitride membrane. Stoichiometric silicon-nitride has a pre-stress of around 1GPa and a yield stress around 6GPa [76]. A finite element simulation done in COMSOL Multiphysics reveals that the stress of a square suspended SiN membrane can reach its yield stress when a point force of around $0.8\mu\text{N}$ is applied at its center. The static radiation force inside the cavity is given by $F_{\text{opt}} = \hbar G n_c$, using the measured parameters of our optomechanical system, the input power needed to create such a force is $\approx 2.9\text{mW}$ (when the cavity is pumped through the more transmissive mirror). This matches the experimental conditions when the membrane ruptured.

¹From simulations shown in Figure 2.8 while considering $x_{z,p} = 2\text{fm}$

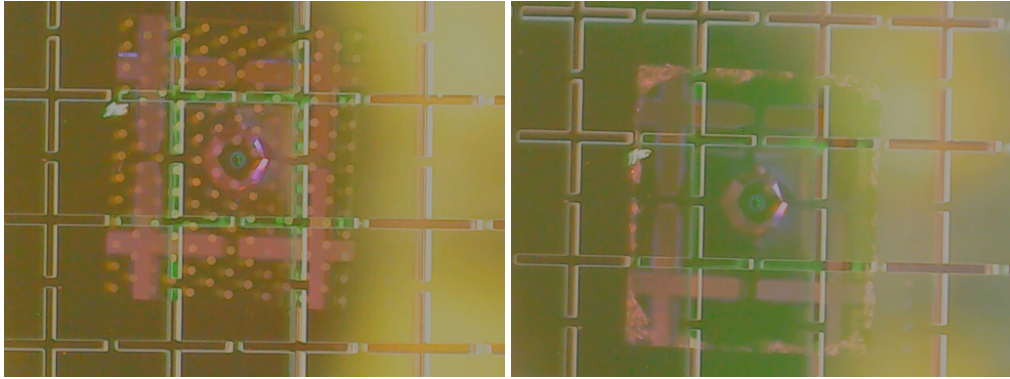


Figure 6.1: Top view of the system before (left) and after (right) a rupture of the membrane. Both images have been obtained using a portable microscope focused through the vacuum chamber window.

Another possible explanation for the rupture is that the membrane collided with one of the mirrors. This is implausible due to the significant membrane to mirror distance, but we will discuss briefly. To start, the static mechanical displacement caused by intracavity radiation pressure is orders of magnitude smaller than the $70\ \mu\text{m}$ distance to the closest mirror. All things considered, the idea is fundamentally flawed because, on its way towards one of the mirrors, it would reach regions of positive, negative and zero optomechanical coupling that would create forces towards one mirror, the other one, or no force at all. Another phenomenon with large membrane displacement is phonon lasing (also called self-oscillations), the anti-damping that manifests when the laser is blue-detuned. In the Chapter 5, we exploited this effect to measure the quality factor by inducing oscillations large enough to be measured with an off-resonant laser. If we look back at the ringdown measurements shown in Figure 5.5a, once the laser is blue-detuned, the signal (which is proportional to $\langle q^2 \rangle$) grows by approximately 60dB before the system becomes unstable. Assuming that the signal prior to phonon lasing is due to thermal motion ($\sqrt{\langle q_{\text{th}}^2 \rangle} \simeq 7\ \text{pm}$) we reach oscillations of $\sqrt{\langle q^2 \rangle} \simeq 7\ \text{nm}$, four orders of magnitude far from the membrane-to-mirror distance. Taking into account that self-oscillations do not grow unbounded, but rather they saturate due to their non-linear nature [25, 77], we deem unlikely that they are the cause of the rupture.

Summarizing, the powers needed to break the membrane are below the powers needed to reach $C_q \simeq 1$ and membrane rupture does not impede quantum regime operation. However, it remains an inconvenience.

6.2 Laser locking at high intracavity-power

The frequency of the laser is kept close to a cavity resonance by means of a Proportional-Integral-Derivative (PID) controller. When we analyze the reflected light of the cavity, we use an amplified photodiode to track the transmission signal. The PID controller, which in this case is implemented by the laser manufacturer, adjusts the laser frequency in order to keep the transmission at a target value. The scheme is usually referred as *side-of-fringe* locking because it only works at $\Delta \neq 0$, as it requires a non-zero derivative of the transmission peak at the target value. The other locking strategy, known as Pound-Drever-Hall (PDH), consists in generating

an error signal that crosses zero at $\Delta = 0$ through phase modulation. PDH works due to phase fluctuations rotating into amplitude fluctuation only when $\Delta \neq 0$. Thus, the demodulation of the transmission or reflection amplitude signal at the same frequency will be zero at $\Delta = 0$.

In our experiment, we work in $\Delta < 0$ in order to lower the phonon occupation through dynamical backaction cooling. We find that locking close to resonance is not reliable at high power due to strong phonon lasing when the frequency momentarily drifts into $\Delta > 0$. Thus, we use a side-of-fringe lock². The locking procedure proceeds as follows:

1. The target transmission is set as a the setpoint of the PID, which is for now deactivated (the three gains are set to zero).
2. The frequency of the laser is parked at a frequency below that of the optical resonance. This translates to adjusting the piezoelectric actuator (piezo from now on).
3. The piezo voltage is slowly increased (in our laser $\omega_l \propto V$) and the transmission signal is monitored. Because we always fulfill $\Delta < 0$, the only instability that may manifest according to our model is the optomechanical bistability.
4. Once the transmission is close to our target, the PID is slowly engaged by increasing its integral gain. We find that the integral gain is enough to keep the cavity resonant in most situations.

A target transmission that ensures $C_q > 1$ is chosen by extrapolating the result of the cooperativity measurement described in Subsection 5.3.1. Problems arise in step 3, when approaching the target signal we observe two types of instabilities. The type of instability depends on the optical mode that we are tuning to.

The first is a dynamical effect where, over the span of a few seconds, the transmission signal starts oscillating at frequencies > 100 kHz. After a few seconds the system becomes unstable. Measurement of the cavity output field reveals the overall mechanical signal growing in amplitude. Although we have not been able to thoroughly study this instability before the elaboration of this report, the symptoms are similar to the photothermal instability observed in the very similar experiment described in [27]. The effect looks similar to phonon lasing in the blue-side of the resonance because photothermal effects can create delayed forces that can damp or anti-damp mechanical modes, in a similar way to dynamical back-action [79].

We also observe a second distinct instability in modes that do not present the photothermal instability. At high powers, the lock starts ringing at a particular frequency, usually significantly below 100 kHz. It differs from the previous instability because it has a single characteristic frequency and its magnitude does not grow in time. The frequency does not depend on the controller gains, which indicates that it might not be a problem of our locking system. We discard optomechanical bistability because its threshold input power is below the input-powers needed to reach a $C_q \simeq 1$. By calculating the discriminant of the cubic equation that determines the intracavity photon number (Equation 2.92) we confirm that we operate the system outside the regions where bistability occurs, which are illustrated in Figure 2.9.³

²In [78], the author describes a modified PDH scheme with an error signal crossing zero at the magic detuning $\Delta = \pm\kappa/2\sqrt{3}$. This is achieved by demodulating the signal a second time after detection. We have not tried such a scheme in our experiment.

³The discriminant of a cubic equation $ax^3 + cx^2 + bx + d = 0$ is $\mathcal{D} = -27a^2d^2 + 18abcd - 4ac^3 - 4b^3d + b^2c^2$. If $\mathcal{D} > 0$, there are three real solutions to the equation, if $\mathcal{D} < 0$ there is one real solution and a pair of complex solutions. From Equation 2.92, we find $(a, b, c, d) = \left(\frac{4g_0^4}{\Omega_m^2}, \frac{4\Delta g_0^2}{\Omega_m}, \Delta^2 + \frac{\kappa^2}{4}, -\dot{n}_{\text{in}}\kappa_1 \right)$.

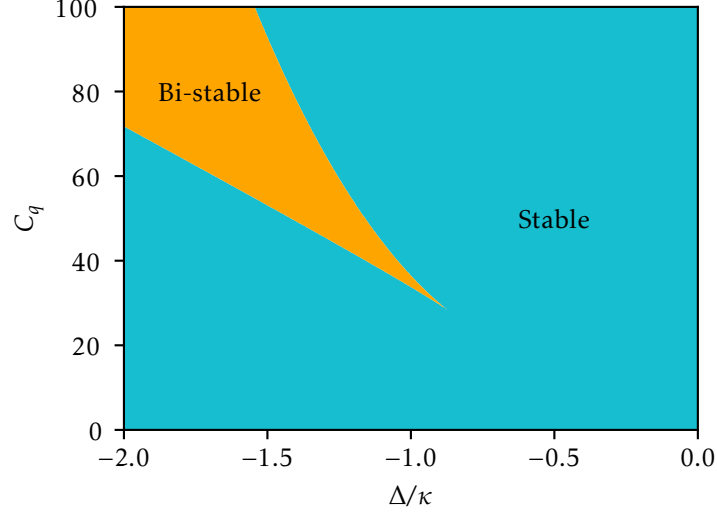


Figure 6.2: Regions of stability (cyan) and bi-stability (orange) in a cavity optomechanical system with parameters $\Omega_m = 2\pi \cdot 1.14\text{MHz}$, $\kappa = 2\pi \cdot 20\text{MHz}$, $\kappa_1 = 10\kappa/11$, $g_0 = 2\pi \cdot 1\text{kHz}$. The horizontal axis is the detuning respect to the bare cavity, in other words, the peak intracavity photon number is at $\Delta < 0$. The vertical axis is the the quantum cooperativity achieved at peak intracavity field.

6.3 Phase noise in optomechanical experiments

In Subsection 5.4.2 we characterized the phase noise of our laser, which is above the quantum limited phase noise given by the uncertainty condition of a coherent beam $\langle \Delta \hat{X}^2 \rangle \langle \Delta \hat{Y}^2 \rangle = \frac{1}{4}$. The effect of laser phase noise is double: it masks the mechanical motion upon detection and it heats the mechanical resonator.

6.3.1 Heating by phase noise

The fact that only intracavity amplitude exerts forces on the resonator does not stop incoming phase noise from affecting the dynamics. As long as $\Delta \neq 0$, incoming phase noise will be rotated into amplitude, creating a stochastic radiation pressure. This incoherent force will raise the phonon occupation, similar to raising the environment's temperature. We will now proceed to estimate the amount of phonons added by laser phase noise.

We will use a classical version of the non-linearized quantum Langevin equation of the cavity (Equation 2.84). We can simplify the derivation by working in the fast cavity limit. We consider $\kappa \gg \Omega_m$, which is an adequate approximation of our system as $\kappa/\Omega_m \simeq 20$. We impose the fast cavity regime by $\dot{a} \rightarrow 0$, which is equivalent to the cavity reacting instantaneously to changes of detuning. We find the dependence of the intracavity field on the relative detuning $\nu(t) = 2\Delta(t)/\kappa$:

$$a(t) = \frac{2\sqrt{\kappa_{\text{in}}}}{\kappa} a_{\text{in}} \frac{1}{1 - i\nu(t)}. \quad (6.1)$$

We will include phase noise through fluctuations in $\nu(t) = \bar{\nu} + \delta\nu(t)$. As we saw in Chapter 5,

phase noise and frequency noise are equivalent. The intracavity number found from the above expression is:

$$n_c(t) = \bar{n}_c \left(1 - \frac{2\bar{v}}{1 + \bar{v}^2} \delta v(t) + \dots \right). \quad (6.2)$$

The fluctuations on the intracavity number create a stochastic force given by:

$$\delta F(t) = -\frac{\hbar g_0}{x_{z.p.}} \delta n_c(t) = \frac{\hbar g}{x_{z.p.}} \frac{2\bar{v}}{1 + \bar{v}^2} \delta v(t), \quad (6.3)$$

where we have used the expression for the optical force inside a cavity Equation 2.125. Its PSD is:

$$S_{\delta F \delta F}(\omega) = 16 \frac{\hbar^2}{x_{z.p.}^2} \frac{g^2}{\kappa^2} \frac{\bar{v}^2}{(1 + \bar{v}^2)^2} S_{\omega_l \omega_l}(\omega), \quad (6.4)$$

where we have used $\delta v = 2\delta\omega_l/\kappa$ assuming all detuning is caused by laser fluctuations (empty cavity with noiseless mirrors). If we make an analogy with the thermal force by comparing the obtained PSD with the PSD of the thermal force (Equation 2.127), we can find the occupancy of the effective bath corresponding to frequency noise:

$$n_{\text{freq. noise}} \simeq \frac{16g^2}{\Gamma_m \kappa^2} \frac{\bar{v}^2}{(1 + \bar{v}^2)^2} S_{\omega_l \omega_l}(\Omega_m) = 4 \frac{C}{\kappa} \frac{\bar{v}^2}{(1 + \bar{v}^2)^2} S_{\omega_l \omega_l}(\Omega_m). \quad (6.5)$$

As expected, the increase of phonon occupation is proportional to the strength of optomechanical interaction through the cooperativity. It also makes intuitive sense that it is inversely proportional to the cavity linewidth. A narrower resonance has larger slope on $\Delta \neq 0$, facilitating the conversion of frequency fluctuations into intracavity power fluctuations. If we consider the laser's frequency noise measured in Chapter 5, when the system is operated at $\Delta^* = -\kappa/2\sqrt{3}$ and $C_q = 0.32$ (Figure 5.6), the thermal bath occupancy is increased by ≈ 1000 phonons. The effect of this heating is negligible when considering the strong dynamical backaction cooling at this cooperativity and detuning.

6.3.2 Phase noise in detection

Phase noise in interferometers can be dealt with by ensuring that the reference beam and the probe propagate the same length. We introduced this idea in Subsection 2.7.2, as well as exploiting it in order to be sensitive to phase noise (Subsection 5.4.2). Our experiment can be seen as an interferometer where one arm contains a cavity. When we measure the cavity's reflection using homodyne detection, it is straight-forward to match the path length of the LO to that of the probe. This will remove phase noise from homodyne detection, but only when the laser is fully off-resonance. Once the laser is tuned to the cavity, we observe balance homodyne (BHD) spectra like the one shown in Figure 6.3.

Once the laser is tuned to the cavity, any input signal, amplitude or phase, will be reflected or transmitted with a delay. Our interferometer arms are now effectively mismatched and the experiment becomes sensitive to phase noise. This is the cause of the increased noise floor of the BHD spectrum obtained when the laser is close to resonance. The obvious next step is to add a physical delay to the LO that matches the cavity induced delay. The LO delay should be in the order of $2\pi/\kappa \approx 50$ ns, it changes with the detuning, being maximum on resonance $\Delta = 0$ and decreasing with $|\Delta|$.

In Figure 6.4, we show the results of delaying the local oscillator in order to remove the influence of phase noise from our measurements. The measurements have been done in the

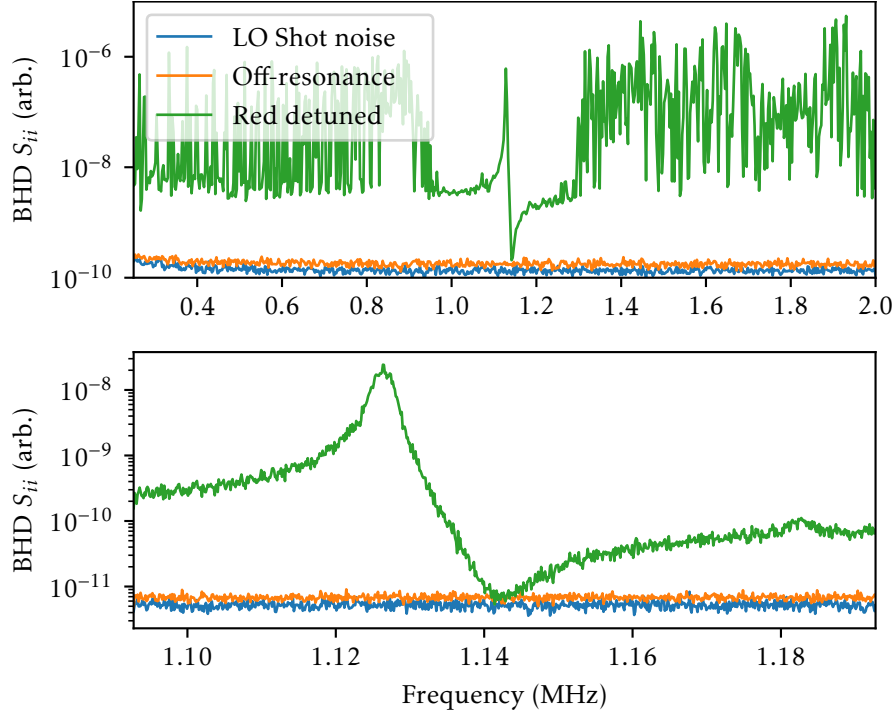


Figure 6.3: Balanced homodyne signal of the MIM cavity reflection recorded with an electronic spectrum analyzer. The bottom plot is the same measurement as the top plot but recorded over a narrower span of frequencies. The blue trace is the local oscillator (LO) shot noise, obtained by blocking the signal beam. The orange trace is obtained when the laser is far from the cavity resonance, because the path of the LO and signal have been matched, the measurement is not sensitive to laser phase noise. The green trace is obtained by tuning the laser to the red side of the resonance $\Delta \approx -0.5\kappa$, the phase of signal is locked at 90° from the LO as to measure the phase quadrature. The overall increase in background noise level when the laser is on resonance is caused by the change in effective propagation distance of the signal respect to the LO.

empty microcavity. First, we have measured the delay induced by the cavity on a 1.3 MHz phase modulation, which is shown in the top plot of Figure 6.4. In the bottom plots, we demonstrate how the signal-to-noise ratio is improved by matching the propagation time of the probe and LO while taking the cavity delay into account. This has been done by adding 2 meters of fiber, equivalent to 9.7 ns. The laser lock was adjusted to remove the largest amount of noise, which happened at the detuning $\Delta = -0.84\kappa$. To finally confirm that the reduction is thanks to the delay, we measure the delay at this detuning using a network analyzer, which is in good agreement with the delay expected at this detuning according to the top plot.

In this manner, we have increased the signal-to-noise ratio of the motion of the mirrors by almost two orders of magnitude. The obvious question is, can laser phase noise be removed completely? In balanced homodyne detection, it is not possible. This is due to the quadrature rotation phenomenon. Cavities not only delay phase noise, but also can remove it or convert it into amplitude noise. First, consider that we are using the BHD to measure the phase quadra-

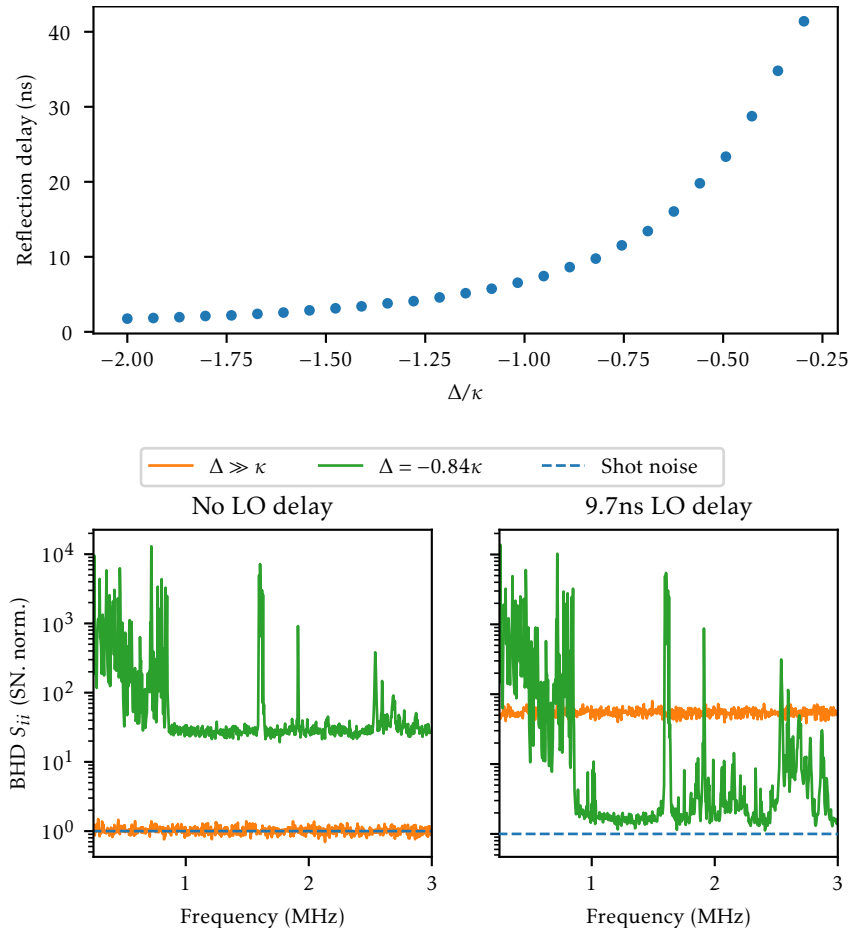


Figure 6.4: The delay of the empty cavity and its effects on phase measurement. **Top plot:** Delay induced on a 1.3MHz phase modulation upon reflection upon reflection from the cavity. The delay increases as the laser frequency get closer to resonance. The linewidth of the optical resonance is $\kappa = 2\pi \cdot 18.3\text{MHz}$. **Bottom plots:** Effect of adding a delay to the local oscillator (LO) on the presence of phase noise in the homodyne detector trace (BHD S_{ii}), which is shown normalized to shot noise. In the bottom left plot, the propagation length of the LO has been carefully matched to the total signal beam when reflecting off-resonance. The off-resonant reflection (orange trace) does not present fluctuations above shot noise (dashed blue trace). When the laser locked at a detuning $\Delta = -0.84\kappa$, the phase spectrum (green) noise background increases, due to the delay of around 9.7 ns induced by the cavity. In the bottom right plot, we have added 2 meters of fiber (refractive index of 1.45) to create a 9.7ns delay, the off-resonant noise (orange) increases by almost two order of magnitude, while the noise in the close to near-resonant trace (green) drops a similar amount, causing a dramatic increase of signal-to-noise ratio.

ture. Any reduction of phase noise in the cavity path will be equivalent to an increase in the LO beam. For example, take the laser noise at frequencies $\gg \kappa$. The noise will not be present in transmission because it is filtered by the limited bandwidth of the cavity. In the other hand, the LO will retain all the noise of the laser. When both beams interfere, we will measure laser phase noise no matter the delay between the paths. More generally, the scheme only works for measuring the phase quadrature, for noise that is not filtered and $\Delta \neq 0$, we have contaminated the amplitude quadrature with noise through the rotation.

We finish our discussion by mentioning that it might be possible to completely cancel phase noise using a single-detector homodyne scheme⁴. Starting with adjusting the propagation time of the LO to that of the signal through the cavity, the delay and power of the LO could be finely adjusted as to project phase noise into amplitude in a manner that cancels the amplitude noise caused by cavity rotation.

6.4 Thermal intermodulation noise

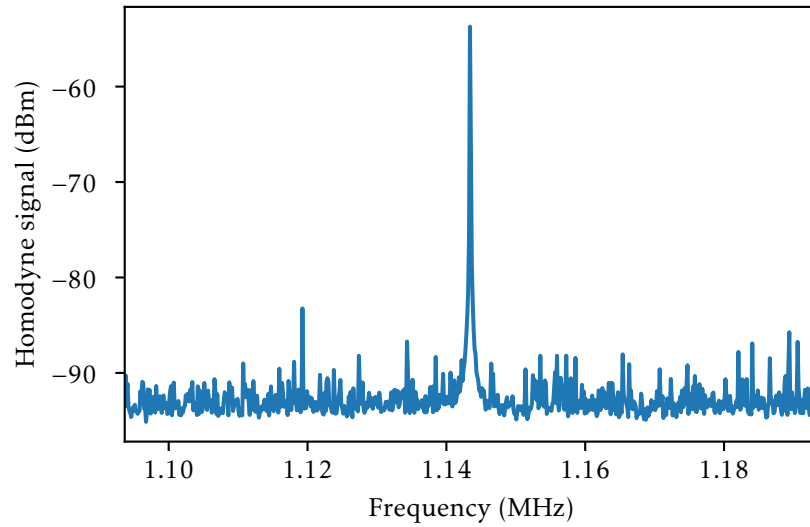


Figure 6.5: Homodyne measurement of the cavity reflection. The phase of the LO was locked in order to measure the phase quadrature. The cavity was interrogated with a low-power $C_q \ll 1$ beam detuned by -0.5κ . The central peak corresponds to the high-Q mechanical mode. All the other peaks are not the result of single mechanical modes, but rather the beat signals of thermomechanical motion of out-of-bandgap modes, what we refer to as thermal intermodulation noise.

Thermal Intermodulation Noise (TIN) is the noise arising from quadratic transduction of mechanical motion into cavity field fluctuations [80]. TIN is problematic because, as its name indicates, it mixes the thermomechanical signal of various modes. TIN appears as a set of peaks at $\Omega_i \pm \Omega_j$ for all i, j mechanical modes. Due to the large density of modes in phononic crystal

⁴The author found this idea in Guanhao Huang's doctoral thesis[27].

resonators, TIN ends up raising the overall noise floor of the signal.

To investigate when TIN appears, we will again work in the fast cavity regime. In this case, the cavity field quickly adjusts to the detuning caused by mechanical motion, which is given by the total membrane motion $\sum q_i(t)$ and the coupling factor G :

$$\Delta(t) = \omega_l - \omega_{c,0} - G \sum q_i(t). \quad (6.6)$$

As done in the previous section, we use classical version of the non-linearized quantum Langevin equation to find the intracavity photon number, but now keeping the second order terms:

$$n_c \propto 1 - \frac{2\nu}{1 + \nu^2} \delta\nu + \frac{3\nu^2 - 1}{(1 + \nu^2)^2} (\delta\nu)^2 \quad (6.7)$$

where we have again expanded the detuning into $\nu + \delta\nu$. The quadratic term will have consequences for both the dynamics of the oscillator as well as the output fields of the cavity. The force created by the quadratic fluctuations of the intracavity power is a sort of back-action. It has been studied thoroughly in the work by [43]. We notice that at a detuning $\nu = \pm 1/\sqrt{3}$, the quadratic term disappears, this is referred to as “magic detuning” [80]. Note that only the intracavity photon number is immune to quadratic fluctuations at the magic detuning, the phase of the field will still depend on $(\delta\nu)^2$. In contrast, on resonance $\delta\nu = 0$, the linear contribution vanishes and the quadratic contribution is at its maximum. In an optomechanical system with a singular mechanical mode, the quadratic back-action acts as an additional optical spring. However, in a multi-mechanical mode system, the quadratic term mixes the mechanical modes and gives rise to TIN.

We observe TIN in our spectra of the output fields measured through homodyne detection, one example is shown in Figure 6.5. We have not characterized TIN in depth because it is not the main limiting factor of our experiment. Once we remove classical phase noise, the current limiting factor, TIN will become the most significant obstacle. The adverse effects of TIN have been successfully suppressed in the work [27]. Efficient TIN suppression is achieved by working at the magic detuning and using a single-detector homodyne scheme [80]. The single-detector homodyne (described in Appendix D) can be made insensitive to quadratic phase fluctuations by adjusting the LO power.

Chapter 7

Conclusions and outlook

In this work, we have presented the theory of cavity quantum optomechanics, including a model for the detection of the cavity fields in the presence of laser phase noise. We have used the theory to show the possibility of optomechanical squeezing at room-temperature.

Based on insights from both the theory of cavity optomechanics and the reality of building quantum optics experiments, we have designed a compact, low-noise optical micro-cavity that houses an ultra-coherent mechanical resonator. We have engineered planar mirrors with optimized phononic patterns that reduce mirror motion at the frequencies of our resonator, which has been experimentally checked.

The micro-cavity has been enabled by an innovative, yet simple, feedback controlled laser ablation protocol. The fabrication process has been thoroughly described and characterized, demonstrating perfect yield and wide control of the fabricated feature's geometry.

The optical, mechanical and optomechanical properties of our membrane-in-the-middle system have been characterized. We have developed measurement protocols that address the problems of characterizing a highly interacting optomechanical system. We have shown how, thanks to the semi-rigid approach to the cavity, the optical loss rate induced by the membrane is small compared to the rate at which light exits through the measurement channel. We have seen how the system has the potential to be in the quantum dominated regime at low input powers.

We have shown how quantum regime operation is prevented by technical problems. We document how the membrane can break due to radiation pressure, which is inconvenient, but does not prevent reaching a quantum cooperativity above 1. We describe and discuss problems in locking the laser to the cavity. We study the challenges of laser phase noise, how it effectively heats the resonator and some approaches to reduce its effects on detection. We briefly touch on the subject of thermal intermodulation noise, which we predict to be the ultimate obstacle to the manifestation of quantum effects in our system.

7.1 Next steps

The main task of this work has been the engineering of the cavity, which has left a limited amount of time to explore the physics of the system.¹ A lot of possible solutions to the exper-

¹The first observation of the mechanical signal in the cavity was achieved around November 2023, with the membrane rupturing for the first time in February 2024. The proper cavity geometry ensuring low optical losses was first

imental challenges have been left on the table, as well as the experiments that can be realized after they are solved. Following are some of the approaches to solve the current challenges:

- A filter cavity. Classical noise can be removed by filtering the laser through a narrow linewidth cavity. Steps towards the implementation of such cavity have been taken in two directions: a free-space monolithic cavity in the lines of the one described in [27, 81] and fiber loop based cavity. The cavity should have a linewidth $< 100\text{kHz}$, which can be achieved using commercial super-mirrors and cavity lengths in the 10s of cm. We predict two challenges with this approach, we must filter a large amount of power for both the probe and local oscillator (upwards of 5mW) and we must keep the filter cavity resonant to the laser while the laser tracks the experiment's cavity frequency.
- A phase noise-eater. Phase noise can be removed through precise and fast feedback based on real time measurement in a set-up like the one showed in Figure 5.8 [51]. This is an easier solution compared to the filter cavity, but it requires a large delay in order to be efficient for measurement of 1MHz noise. Additionally, it is limited by fiber noise. One could circumvent this by creating a free-space delay line, some recent free-space folded delay designs [82] can allow for the 500ns required to sense 1MHz optimally.
- Removal of phase noise in post-processing. We have observed correlations between time-traces of the cavity signal and an independent time-trace of phase noise. This could be used to remove the effect of phase noise on the measured time trace, but not the heating associated with it.
- Different laser source. The laser used was chosen due to its wide tunability, needed due to the large free-spectral range of our micro-cavity. Due to the fact that the bottom mirror is made of silicon, we must use a wavelength $\gtrsim 1100\text{nm}$, lower wavelengths are strongly absorbed by silicon. One could imagine using a wide-tunable but noise-less at our frequency range, like a Titanium-Sapphire laser, and use an optical parametric oscillator to increase the wavelength from around 775nm to around 1550nm .
- Problems with locking. A feedback cooling system to lower the excitation of membrane modes below the bandgap could be beneficial for improving lock stability, as reported in [78].
- Transmission measurement set-up. We have presented the set-up that has been more practical for characterizing the system, which collects the reflection of the cavity back to fiber. This comes at a cost of a collection efficiency $\eta \lesssim 0.5$. This completely removes squeezing in the output beam through mixing with vacuum. The optimal set-up would measure the transmission of the cavity directly in the homodyne detector, this implies pumping the system from the more reflective mirror (the silicon mirror).
- Lower reflectivity of mirrors. To optimize the cavity for mechanical motion sensing, it could be preferable to lower the finesse in a way that does not introduce losses. This could be done with a laser farther away from the mirrors design wavelengths, or by reducing the reflectivity of the mirrors through etching of a few layers of the coating[83].

Once these solutions hopefully solve the remaining technical problems of the set-up, we can observe phenomena that manifests in the unresolved sideband regime. The following experiments could be realized, roughly ordered from more approachable to less:

- Conditional state preparation of the mechanics close to the ground state[78, 84–86]. Instead of physically cooling the mechanical oscillator using a feedback force, if our measurement precision is below the zero-point motion while “averaging” for a duration smaller

assembled at the start of July 2024, after a patient exploration of spacer sizes and mounting geometries. The membrane broke again during third week of August 2024.

than the thermal dissipation rate, we can prepare a thermal state with occupation below unity conditioned to our measurement record.

- Feedback cooling close to the ground state. Optimally estimating the position of the mechanical mode and using a second source of light to damp the oscillator [26, 61]. Before reaching the ground state, it could allow the measurement of motional sideband asymmetry [28]
- Coherent feedback cooling. Coherent feedback cooling is an all optical, measurement-less method of cooling protocol. By projecting the phase quadrature of the out beam, which contains position information, to the amplitude quadrature, we can generate an optical force proportional to position. By delaying the beam and feeding it back to the cavity, a damping force is generated that can cool the system to the ground-state [87].
- Optomechanical squeezing is present as long as $C_q \gtrsim 1$, the challenge is reducing the losses a long the path the cavity output field suffers before reaching the detector [78, 88].

Appendix A

The Markovian quantum Langevin equation

I will very briefly sketch the derivation of the Markovian quantum Langevin equation in order to highlight the assumptions and approximations used.

The mechanical resonator and its environment are modeled through the following Hamiltonian:

$$\hat{H} = \underbrace{\frac{1}{2m}\hat{p}^2}_{\hat{H}_{\text{sys}}} + \frac{1}{2}k\hat{q}^2 + \underbrace{\sum_j \frac{1}{2m_j}\hat{p}_j^2 + \frac{1}{2}k_j(\hat{q}_j - \hat{q})^2}_{\hat{H}_{\text{env}} + \hat{H}_{\text{sys-env}}}. \quad (\text{A.1})$$

A possibly infinite number of masses m_j are connected through springs of constant k_j to our oscillator of interest. The evolution of an operator $\hat{O}(t)$ in the Heisenberg picture can be found using the Heisenberg equation:

$$\dot{\hat{O}}(t) = \frac{1}{i\hbar}[\hat{O}(t), \hat{H}(t)] = \quad (\text{A.2})$$

$$= \frac{1}{i\hbar}[\hat{O}, \hat{H}_{\text{sys}}] - \frac{1}{2i\hbar} \sum_j k_j \{[\hat{O}, \hat{q}], \hat{q}_j - \hat{q}\}, \quad (\text{A.3})$$

where $\{\hat{A}, \hat{B}\} = \hat{A}\hat{B} + \hat{B}\hat{A}$ is the anti-commutator. We would like to remove any dependence on bath properties and operators, namely k_j and \hat{q}_j . To achieve that, we start by finding the differential equations governing \hat{q} and \hat{q}_j using the previous Heisenberg equation. Second, a formal solution for \hat{q}_j is written so that we can arrive at an integral-differential equation containing exclusively \hat{q} terms. The resulting expression is found by ignoring transients caused by the environment's initial conditions as well as considering a continuum of environment modes ($k_j \rightarrow k(\Omega)$, $\sum_j \dots \rightarrow \int \rho(\Omega) \dots d\Omega$):

$$m\ddot{\hat{q}} + m \int_{-\infty}^t \Gamma(t-t')\dot{\hat{q}}(t') dt' + (k + k_{\text{env}})\hat{q} = \hat{F}(t). \quad (\text{A.4})$$

$$\Gamma(\Omega) = \mathcal{F}[\gamma(t)](\Omega) = \frac{k(\Omega)\rho(\Omega)}{4m} \quad (\text{A.5})$$

$$k_{\text{env}} = \int_0^\infty \rho(\Omega) k(\Omega) d\Omega \quad (\text{A.6})$$

$$\hat{F}(t) = \sum_j k_j \hat{q}_j^h(t) \quad \text{where} \quad \ddot{q}_j^h = -k_j \hat{q}_j^h \quad (\text{A.7})$$

If the environment oscillators are thermalized at temperature T , \hat{F} fulfills the quantum fluctuation-dissipation theorem:

$$S_{\hat{F}\hat{F}}(\omega) = 2m\Gamma(\omega)\hbar\omega(\bar{n}(\omega) + 1) \quad (\text{A.8})$$

$$S_{\hat{F}\hat{F}}(-\omega) = 2m\Gamma(\omega)\hbar\omega\bar{n}(\omega), \quad (\text{A.9})$$

where $\bar{n}(\omega)$ is the previously introduced Bose-Einstein distribution:

$$\bar{n}(\omega) = \frac{1}{e^{\frac{\hbar\omega}{k_B T}} - 1}. \quad (\text{A.10})$$

From now on, we will absorb k_{env} into k . We can update the Heisenberg equation with Equation A.4:

$$\dot{\hat{O}}(t) = \frac{1}{i\hbar}[\hat{O}, \hat{H}_{\text{sys}}] - \frac{1}{i\hbar}[\hat{O}, \hat{q}]\hat{F}(t) - \frac{m}{2i\hbar} \left\{ [\hat{O}, \hat{q}], \int_{-\infty}^t \Gamma(t-t') \hat{q}(t') dt' \right\}. \quad (\text{A.11})$$

To get rid of the k_j and \hat{q}_j dependencies we must perform our first approximation, the Markov approximation. The Markov approximation considers $\Gamma(t) = \Gamma_m \delta(t)$, which is equivalent to assuming that the environment is a memory-less bath. Equation A.4 becomes the familiar damped harmonic oscillator:

$$m\ddot{\hat{q}}(t) + m\Gamma_m \dot{\hat{q}}(t) + k\hat{q}(t) = \hat{F}(t), \quad (\text{A.12})$$

and the Langevin equation for a general operator becomes:

$$\dot{\hat{O}}(t) = \frac{1}{i\hbar}[\hat{O}, \hat{H}_{\text{sys}}] - \frac{1}{i\hbar}[\hat{O}, \hat{q}]\hat{F}(t) - \frac{m\Gamma_m}{2i\hbar} \{ [\hat{O}, \hat{q}], \hat{q}(t) \}. \quad (\text{A.13})$$

It is convenient to express the Langevin equation in terms of the dimension-less quadrature operators. A momentum input operator can be written as:

$$\hat{P}_{\text{in}}(t) = \frac{i}{\sqrt{2}} (\hat{b}_{\text{in}}^\dagger + \hat{b}_{\text{in}}) = \frac{x_{\text{z.p.}}}{\hbar\sqrt{\Gamma_m}} \hat{F}(t). \quad (\text{A.14})$$

$\hat{P}_{\text{in}}(t)$ has units of $\sqrt{\text{Hz}}$ because it is an input operator and describes an input rate of momentum. Now we can write the Langevin equation as:

$$\dot{\hat{O}}(t) = \frac{1}{i\hbar}[\hat{O}, \hat{H}_{\text{sys}}] + i\sqrt{2\Gamma_m} [\hat{O}, \hat{Q}] \hat{P}_{\text{in}}(t) + \frac{\Gamma_m}{2i\Omega_m} \{ [\hat{O}, \hat{Q}], \hat{Q}(t) \}. \quad (\text{A.15})$$

Appendix B

Separation of fields into average and fluctuation terms

Through out this work we have written the annihilation operator \hat{a} of a given field as a sum of its mean value $\alpha = |\alpha|e^{i\theta} \in \mathbb{C}$ and a fluctuation term $\delta\hat{a}$:

$$\hat{a} = \alpha + \delta\hat{a}. \quad (\text{B.1})$$

We attribute all quantum behavior to the fluctuation term. We can also apply the same concept to the amplitude and phase quadratures of the field, but some care must be taken when obtaining the fluctuations of those quadratures $\delta\hat{X}$ and $\delta\hat{Y}$ from the fluctuations $\delta\hat{a}$ and $\delta\hat{a}^\dagger$. We associate amplitude fluctuations with those that change the intensity of the field. This is the only way, as the mean field α is the only reference available. In an experiment, when we measure using a homodyne detector, we associate measuring $\delta\hat{X}$ when the local oscillator is interfering constructively (or destructively for $-\delta\hat{X}$). The phase quadrature fluctuations $\delta\hat{Y}$ are "perpendicular" to $\delta\hat{X}$. We measure them by interfering with a local oscillator at a node of the interference pattern. In order to be consistent with how we measure δX and δY , we must use the following relations [89]:

$$\delta\hat{X} = \frac{1}{\sqrt{2}}(e^{i\theta}\delta\hat{a}^\dagger + e^{-i\theta}\delta\hat{a}), \quad (\text{B.2a})$$

$$\delta\hat{Y} = \frac{i}{\sqrt{2}}(e^{i\theta}\delta\hat{a}^\dagger - e^{-i\theta}\delta\hat{a}), \quad (\text{B.2b})$$

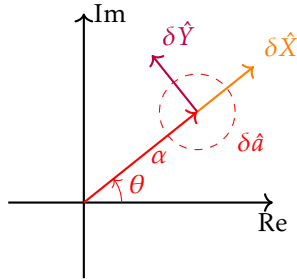


Figure B.1: Representation of the field fluctuations in phase-space

and the ladder operators can be written as:

$$\delta\hat{a} = \frac{e^{i\theta}}{\sqrt{2}}(\delta\hat{X} + i\delta\hat{Y}), \quad (\text{B.3})$$

$$\delta\hat{a}^\dagger = \frac{e^{-i\theta}}{\sqrt{2}}(\delta\hat{X} - i\delta\hat{Y}). \quad (\text{B.4})$$

An arbitrary quadrature $\delta\hat{X}^\varphi = \delta\hat{X} \cos \varphi + \delta\hat{Y} \sin \varphi$ can also be written as:

$$\delta\hat{X}^\varphi = \frac{1}{\sqrt{2}}[e^{i(\theta+\varphi)}\delta\hat{a}^\dagger + e^{-i(\theta+\varphi)}\delta\hat{a}]. \quad (\text{B.5})$$

Appendix C

Power Spectral Density

C.1 Definition and conventions

I take the following definition of the cross-power spectral density (cross-PSD) of Heisenberg picture operators $\hat{A}(t)$ and $\hat{B}(t)$ [33]:

$$S_{\hat{A}\hat{B}}(\omega) = \lim_{\tau \rightarrow \infty} \frac{1}{\tau} \left\langle [\hat{A}_\tau(\omega)]^\dagger \hat{B}_\tau(\omega) \right\rangle = \int_{-\infty}^{\infty} e^{i\omega\tau} \left\langle [\hat{A}(t+\tau)]^\dagger \hat{B}(t) \right\rangle_{t=0} d\tau = \int_{-\infty}^{\infty} \left\langle [\hat{A}(-\omega)]^\dagger \hat{B}(\omega') \right\rangle \frac{d\omega'}{2\pi} \quad (\text{C.1})$$

Where I use the following definition for the windowed Fourier transform:

$$\hat{A}_\tau(\omega) = \mathcal{F}_\tau\{\hat{A}(t)\}(\omega) = \int_{-\tau/2}^{\tau/2} e^{i\omega t} \hat{A}(t) dt. \quad (\text{C.2})$$

I take the usual Fourier transform definition:

$$\hat{A}(\omega) = \mathcal{F}\{\hat{A}(t)\}(\omega) = \int_{-\infty}^{\infty} e^{i\omega t} \hat{A}(t) dt. \quad (\text{C.3})$$

Implying $\mathcal{F}\left\{\frac{d^n \hat{A}(t)}{dt^n}\right\}(\omega) = (-i\omega)^n \mathcal{F}\{\hat{A}(t)\}(\omega)$. I use the following notation for the Fourier transform of the Hermitian conjugate of an operator:

$$\hat{A}^\dagger(\omega) = \mathcal{F}\left\{[\hat{A}(t)]^\dagger\right\}(\omega). \quad (\text{C.4})$$

Notice that given the definition of the Fourier transform, the following condition applies to any operator:

$$[\hat{A}(\omega)]^\dagger = \hat{A}^\dagger(-\omega), \quad (\text{C.5})$$

which allows one to write Equation C.1 as:

$$S_{\hat{A}\hat{B}}(\omega) = \int_{-\infty}^{\infty} \left\langle \hat{A}^\dagger(\omega) \hat{B}(\omega') \right\rangle \frac{d\omega'}{2\pi} \quad (\text{C.6})$$

Hermitian operators in particular fulfill:

$$[\hat{X}(\omega)]^\dagger = \hat{X}(-\omega) \quad \text{where} \quad \hat{X}^\dagger = \hat{X}. \quad (\text{C.7})$$

For convenience:

$$S_{\hat{O}}(\omega) := S_{\hat{O}\hat{O}}(\omega) \quad (\text{C.8})$$

. The symmetrized PSD is defined as follows:

$$\bar{S}_{\hat{A}\hat{B}}(\omega) := \frac{S_{\hat{A}\hat{B}}(\omega) + S_{\hat{A}\hat{B}}(-\omega)}{2} \quad (\text{C.9})$$

C.2 Useful results

Here is a list of some results that might seem trivial to the reader but do not appear so obvious to the author:

- The second moment of an operator \hat{O} can be found from its cross-PSD or symmetrized cross-PSD:

$$\langle \hat{O}^2 \rangle = \frac{1}{2\pi} \int_{-\infty}^{\infty} S_{\hat{O}\hat{O}}(\omega) d\omega = \frac{1}{\pi} \int_0^{\infty} \bar{S}_{\hat{O}\hat{O}}(\omega) d\omega \quad (\text{C.10})$$

To arrive at this expression, I used Equation C.1 and the fact that the Dirac delta function is given by $\delta(a-b) = \frac{1}{2\pi} \int_{-\infty}^{\infty} e^{ix(a-b)} dx$.

- As a consequence of the previous result, if $\hat{X} = \hat{X}^\dagger$ is a Hermitian operator, then the second moment is given from its PSD or symmetrized PSD:

$$\langle \hat{X}^2 \rangle = \frac{1}{2\pi} \int_{-\infty}^{\infty} S_{\hat{X}\hat{X}}(\omega) d\omega = \frac{1}{\pi} \int_0^{\infty} \bar{S}_{\hat{X}\hat{X}}(\omega) d\omega \quad \text{where } \hat{X}^\dagger = \hat{X}. \quad (\text{C.11})$$

- From the definition in Equation C.1 I find:

$$S_{\hat{A}\hat{B}} = S_{\hat{B}\hat{A}}^* \quad (\text{C.12})$$

- The PSD of an operator \hat{O} that in Fourier space is given by: $\hat{O}(\omega) = \chi_{\hat{A}}(\omega)\hat{A}(\omega) + \chi_{\hat{B}}(\omega)\hat{B}(\omega)$, with $\chi_{\hat{A}}(\omega), \chi_{\hat{B}}(\omega) \in \mathbb{C}$, can be found from the definition in Equation C.1:

$$S_{\hat{O}\hat{O}}(\omega) = |\chi_{\hat{A}}(\omega)|^2 S_{\hat{A}\hat{A}}(\omega) + |\chi_{\hat{B}}(\omega)|^2 S_{\hat{B}\hat{B}}(\omega) + 2 \operatorname{Re}\{\chi_{\hat{A}}^*(\omega)\chi_{\hat{B}}(\omega)S_{\hat{A}\hat{B}}\}, \quad (\text{C.13})$$

where I used Equation C.12.

- If $\hat{O}(\omega) = \chi(\omega)\hat{A}(\omega)$, with $\chi(\omega) \in \mathbb{C}$, then:

$$[\hat{O}(\omega)]^\dagger = [\chi(\omega)\hat{A}(\omega)]^\dagger = \chi^*(\omega)\hat{A}^\dagger(-\omega) \quad (\text{C.14})$$

and:

$$\hat{O}^\dagger(\omega) = \chi^*(-\omega)\hat{A}^\dagger(\omega). \quad (\text{C.15})$$

Notice that Equation C.5 still holds.

Appendix D

Single Detector Homodyne

Single-detector homodyne (SHD) is the simplest phase-referenced detection. It is seldom used due to the advantages of balanced homodyne detection, which will be presented in the next section. However, SHD has found a niche in cavity optomechanics because it can be made insensitive to quadratic frequency noise [80]. SHD has very recently allowed the observation of optomechanical squeezing at room temperature [27], as well as mechanical sideband asymmetry [28].

SHD consists in mixing our signal field, the one we want to detect, with a local oscillator (LO) through a highly asymmetrical beamsplitter, that is, larger reflectivity than transmittivity or vice-versa. The resulting field is measured in a photodetector. The highly asymmetrical beamsplitter is needed to ensure minimal losses in our signal beam, which can easily kill any squeezing in the fluctuations. This makes it so that a large amount of light is needed in the other port in order to have a large enough LO. Let us consider that we use a beamsplitter with ratio ϵ so that the beam reaching the photodiode is:

$$\hat{a} = \sqrt{\epsilon}\hat{a}_s + i\sqrt{1-\epsilon}\hat{a}_{\text{LO}}, \quad (\text{D.1})$$

and the photocurrent is:

$$\begin{aligned}
\hat{i} &= |\hat{a}|^2 \\
&= \underbrace{\epsilon|\alpha_s|^2 + (1-\epsilon)|\alpha_{\text{LO}}|^2 + 2\sqrt{\epsilon(1-\epsilon)}|\alpha_s||\alpha_{\text{LO}}|\sin(\theta_{\text{LO}} - \theta_s)}_{i_{\text{DC}}} + \\
&\quad + \underbrace{\sqrt{2\epsilon}|\alpha_s|\delta\hat{X}_s + \sqrt{2(1-\epsilon)}|\alpha_{\text{LO}}|\delta\hat{X}_{\text{LO}}}_{\text{Direct detection/amplitude fluctuations}} + \\
&\quad + \underbrace{\sqrt{2\epsilon(1-\epsilon)}|\alpha_{\text{LO}}|(\delta\hat{X}_s \sin(\theta_{\text{LO}} - \theta_s) + \delta\hat{Y}_s \cos(\theta_{\text{LO}} - \theta_s))}_{\text{LO projects signal quadratures}} + \\
&\quad + \underbrace{\sqrt{2\epsilon(1-\epsilon)}|\alpha_s|(\delta\hat{X}_{\text{LO}} \sin(\theta_s - \theta_{\text{LO}}) + \delta\hat{Y}_{\text{LO}} \cos(\theta_s - \theta_{\text{LO}}))}_{\text{Signal projects LO quadratures}} + \\
&\quad + \underbrace{\epsilon|\delta\hat{a}_s|^2 + (1-\epsilon)|\delta\hat{a}_{\text{LO}}|^2 + i\sqrt{\epsilon(1-\epsilon)}(\delta\hat{a}_s^\dagger \delta\hat{a}_{\text{LO}} - \delta\hat{a}_{\text{LO}}^\dagger \delta\hat{a}_s)}_{\text{Second order}}
\end{aligned} \tag{D.2}$$

SHD measures the signal quadrature at an angle that is not equal to the phase between the signal and LO because it has elements of both direct and phase referenced detection. We can find what quadrature SHD is measuring by re-writing the expression above in the following manner:

$$\delta\hat{i} = \hat{i} - i_{\text{DC}} = \sqrt{2}|\beta|\delta\hat{X}_s^{\theta_{\text{SHD}}} + \sqrt{2}|\beta'|\delta\hat{X}_{\text{LO}}^{\theta'_{\text{SHD}}}, \tag{D.3}$$

which is valid in the linearized approximation. The angles are given by the following expressions:

$$\tan \theta_{\text{SHD}} = \frac{\sqrt{\epsilon(1-\epsilon)}|\alpha_{\text{LO}}|\cos(\theta_s - \theta_{\text{LO}})}{\epsilon|\alpha_s| + \sqrt{\epsilon(1-\epsilon)}|\alpha_{\text{LO}}|\sin(\theta_s - \theta_{\text{LO}})} \tag{D.4}$$

$$\tan \theta'_{\text{SHD}} = \frac{-\sqrt{\epsilon(1-\epsilon)}|\alpha_s|\cos(\theta_{\text{LO}} - \theta_s)}{(1-\epsilon)|\alpha_{\text{LO}}| - \sqrt{\epsilon(1-\epsilon)}|\alpha_s|\sin(\theta_{\text{LO}} - \theta_s)}, \tag{D.5}$$

$$\tag{D.6}$$

and the amplitudes given by:

$$\beta = \sqrt{\epsilon^2|\alpha_s|^2 + \epsilon(1-\epsilon)|\alpha_{\text{LO}}|^2 + 2\sqrt{\epsilon^3(1-\epsilon)}|\alpha_s||\alpha_{\text{LO}}|\sin(\theta_s - \theta_{\text{LO}})} \tag{D.7}$$

$$\beta' = \sqrt{(1-\epsilon)^2|\alpha_{\text{LO}}|^2 + \epsilon(1-\epsilon)|\alpha_s|^2 + 2\sqrt{\epsilon(1-\epsilon)^3}|\alpha_s||\alpha_{\text{LO}}|\sin(\theta_{\text{LO}} - \theta_s)}. \tag{D.8}$$

This formulation makes it clear that the quadrature angle measured in SHD is not given by the phase between signal and LO. However, in the limit $(1-\epsilon)|\alpha_{\text{LO}}| \gg \epsilon|\alpha_s|$: $\theta_{\text{SHD}} \rightarrow \frac{\pi}{2} + \theta_{\text{LO}} - \theta_s$, $\theta'_{\text{SHD}} \rightarrow 0$ and $|\beta|, |\beta'| \rightarrow |\alpha_{\text{LO}}|$. Thus, we recover the usual homodyne limit, where the photocurrent fluctuations are given by the shot-noise of the LO and we of a quadrature of the signal given by the relative phase between the two. We will not do such approximation, as the phase noise of the laser is usually well above the quantum fluctuations.

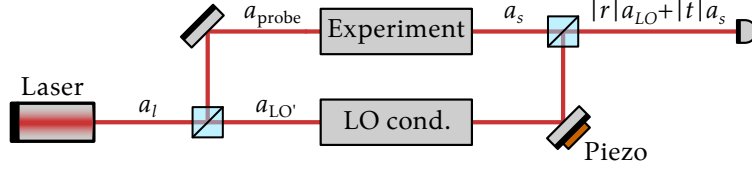


Figure D.1: General scheme for single-detector homodyne detection. Both the local oscillator and probe beams are sourced from the same laser.

We are now going to investigate how laser phase noise can affect our SHD measurement. In a majority of experiments, including us, phase referenced detection is implemented experimentally by splitting one laser into two beams, the probe and the LO, like shown in Figure D.1. The probe feeds an experiment that outputs the signal. If the laser has classical noise, there will be classical correlations between LO and signal. The fact that the signal of SHD is linear on quadrature fluctuations means that we can arbitrarily split the fluctuations into different contributions and study the effect. We can then ignore quantum fluctuations and study the effect of classical phase noise originating in the laser. First, we consider our laser as a coherent beam with additional phase fluctuations $\delta\phi$:

$$\hat{a}_l = \alpha_l e^{i\delta\phi} + \delta\hat{a}_l^{\text{vac}} \simeq \alpha_l + i\alpha_l\delta\phi + \delta\hat{a}_l^{\text{vac}}, \quad (\text{D.9})$$

where $\delta\hat{a}_l^{\text{vac}}$ are the fluctuation associated with a coherent beam (which are the same for vacuum). The laser is split into a fraction ξ that becomes the probe, and another $1 - \xi$ which acts as a precursor to the LO.

$$\hat{a}_{\text{probe}} = \xi\alpha_l + i\xi\alpha_l\delta\phi + \hat{\cdot} = \alpha_{\text{probe}} + i\alpha_{\text{probe}}\delta\phi + \hat{\cdot}. \quad (\text{D.10})$$

$$\hat{a}_{\text{LO}} = (1 - \xi)\alpha_l + i(1 - \xi)\alpha_l\delta\phi + \hat{\cdot} = \alpha_{\text{LO}} + i\alpha_{\text{LO}}\delta\phi + \hat{\cdot}. \quad (\text{D.11})$$

For illustration purposes, let us first consider that both the experiment and the LO path are free-space and have the same length, except for a small adjustable element to adjust the phase of the LO so that $\hat{a}_{\text{LO}} = e^{i\theta}\hat{a}_{\text{LO}}$ and $\hat{a}_s = \hat{a}_{\text{probe}}$. In order to use Equation D.3, we find the quadratures of both beams:

$$\delta\hat{X}_s = \hat{\cdot} \quad \delta\hat{Y}_s = \sqrt{2}|\alpha_s|\delta\phi + \hat{\cdot}. \quad (\text{D.12})$$

$$\delta\hat{X}_{\text{LO}} = \hat{\cdot} \quad \delta\hat{Y}_{\text{LO}} = \sqrt{2}|\alpha_{\text{LO}}|\delta\phi + \hat{\cdot}. \quad (\text{D.13})$$

When we input these expressions into Equation D.3, we will find that contributions proportional to $\delta\phi$ vanish. Mathematically, this happens because $|\alpha_s|\beta \sin\theta_{\text{SHD}} = -|\alpha_{\text{LO}}|\beta' \sin\theta'_{\text{SHD}}$.

Appendix E

The vacuum set-up

E.1 Overall description and operation

The vacuum set-up used in this work was implemented from scratch. Through a lot of trial and error, due to my null starting experience with vacuum, I converged into the set-up shown in Figure E.1 and described in this appendix.

The chamber that houses the experiment is a 6-way cube with DN63CF flanges (LewVac FL-CUBE63CF)¹. Two vacuum pumps are used a roughing pump (Edwards T-Station 85), used to evacuate the majority of the air, and an ion pump (GammaVacuum TiTan 25S, 20L/s)², used to maintain the chamber at pressure of around 5×10^{-8} mbar. The access of each pump to the cavity is controlled by two valves. All the vacuum system uses CF flanges, except a KF flange where the roughing pump is connected. The KF flange is chosen due to its quick release and re-usability of its rubber gaskets. The KF flange, which is not rated for UHV, is isolated from the system by a CF valve through an adapter flange. The roughing pump chains a membrane pump that brings the pressure of the chamber from atmospheric pressure down to 0.5 mbar with a turbo pump that further reduces it to 10^{-7} mbar. The mechanical nature of the turbo pump induces vibrations on the system and cannot be left on while doing experiments. Instead, we use the ion pump (G) to further reduce and keep the vacuum. We need two pumps because ion pumps can only operate at already low pressures (around and below to 10^{-5} mbar), this is due to the working principle of ion pumps. Because they work by ionizing the air and depositing the ions in a cathode, at high air pressures an arc is formed, shorting the anode and cathode.

The procedure of air evacuation usually starts with the ion pump valve closed, with the ion pump keeping a vacuum in the space between itself and the valve. The ion pump is kept running continuously because exposure to the atmosphere lowers its performance. In this configuration, the steps to pump the system down are:

1. The roughing pump is connected to the vacuum system through a KF flange.
2. The roughing pump valve is opened.

¹Two elements with CF flanges (ConFlat) are joint by screwing them together with a copper gasket in-between. The flange (i.e the hole that connects the components) has a knife edge in the rim that "bites" into the gasket, making a seal that can hold a vacuum of 10^{-13} mbar (in a best-case scenario).

²We started with a smaller ion pump (GammaVacuum TiTan 5S, 5L/s) that stopped working properly after a few months of use. No baking of the system helped. Due to the small increase in price for an ion pump with increased pumping rate, I would recommend to go for the largest ion pump that is able to fit in a set-up

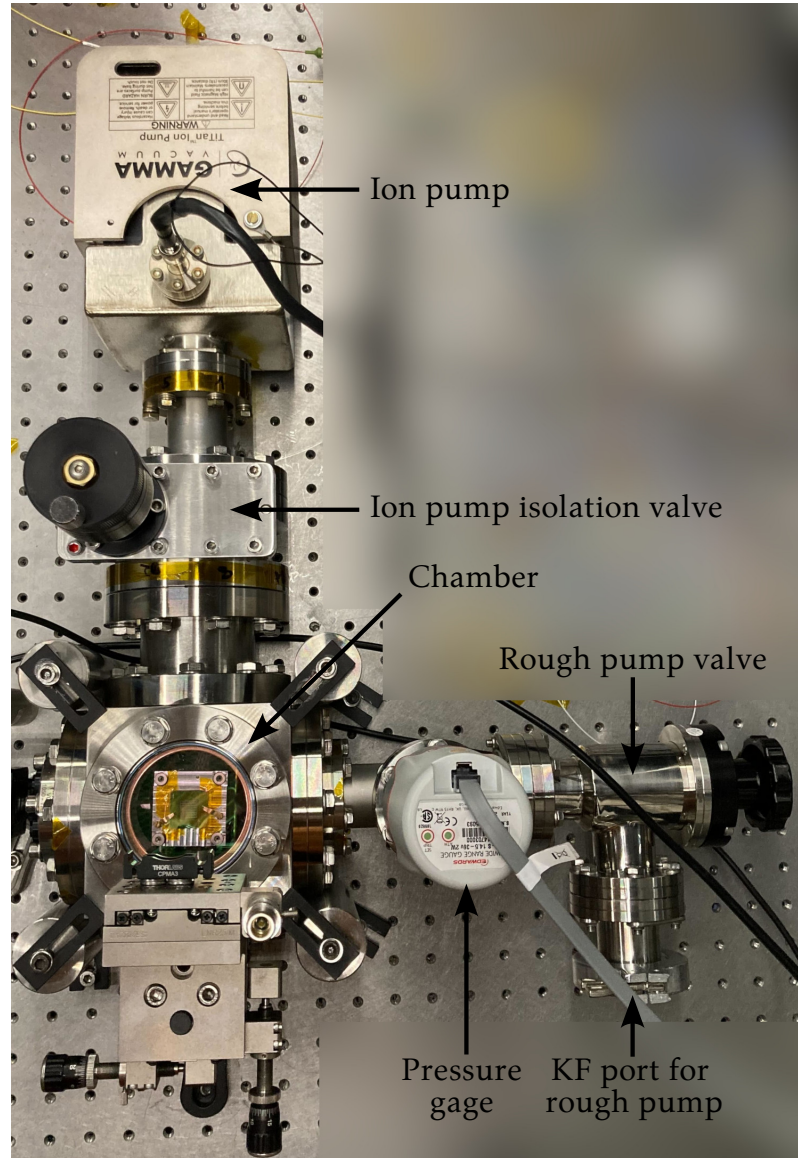


Figure E.1: Top view of the vacuum chamber.

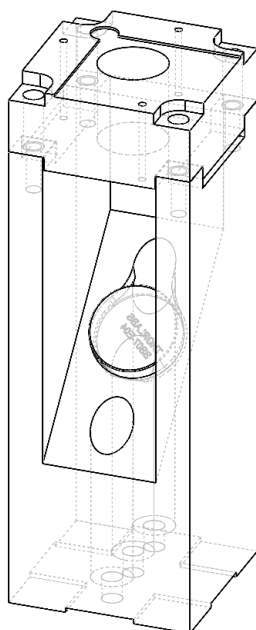


Figure E.2: Schematic rendering of the cavity holder. The holder is composed of two components, the main holder, and the carrier, both made of aluminium at our department's workshop. The main holder is screwed to the bottom flange of the vacuum chamber, while carrier attaches to the main holder. This set-up allows us to assemble the cavity on the carrier without keeping the vacuum chamber exposed to the atmosphere. A 19mm diameter dielectric mirror is placed in the notch of the main holder, this is the tilted mirror that allows collection of transmitted light when the system is pumped from above (see Figure 3.10).

3. The roughing pump is turned on, the pressure is monitored with a pressure gage, after a couple of hours, the system reaches pressures in the lows 10^{-7} mbar.
4. At this point, the ion pump valve is opened.
5. As soon as possible, the roughing pump valve is closed.
6. The roughing pump is disconnected from the system by releasing the KF flange.
7. Over the next hours, the system reaches pressure just below 10^{-7} mbar. After a couple of days, the system's pressure plateaus to 5×10^{-8} mbar.

E.2 The cavity holder

A schematic view of the holder used in the vacuum chamber is shown in Figure E.2. Before placing the holder in the vacuum chamber, it was cleaned by blowing it with pressured nitrogen and an acetone ultra-sonic bath.

Appendix F

Modulation depth calibration

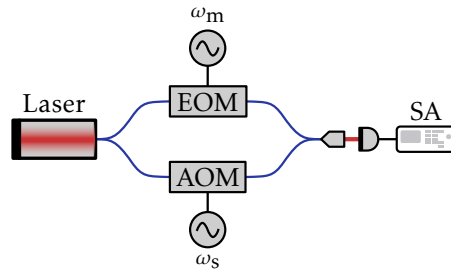


Figure F.1: The depth of a phase modulation created by a phase modulator, EOM in the figure, can be measured by interference with a beam with shifted carrier frequency. The shift is achieved through the acousto-optical modulator (AOM). The ratio of the height of the peaks at ω_s and $\omega_s \pm \omega_m$ in the spectrum recorded by the spectrum analyzer (SA) can be used to determine the modulation depth in radians.

Phase modulators add a voltage controlled phase to a beam. In the RF band (above tens of kilohertz), this is usually done with an Electro-Optical Modulator (EOM). EOMs exploit the electro-optical effect, the change of refractive index caused by applying voltage to a material. EOMs work from DC to GHz with the transduction factor between voltage and phase changing with frequency. The transduction factor is usually expressed by manufacturers as V_π , the voltage needed to induce a π rad phase. A voltage signal of frequency ω_m with amplitude V_a :

$$v(t) = V_a(\omega_m) \cdot \sin \omega_m t \quad (\text{F.1})$$

is applied to the EOM, which generates a phase modulation:

$$\phi(t) = \beta(\omega_m) \cdot \sin \omega_m t, \quad (\text{F.2})$$

where:

$$\beta(\omega_m) = \pi \frac{V_a(\omega_m)}{V_\pi(\omega_m)}. \quad (\text{F.3})$$

is the modulation depth.

The modulation depth can be determined through various methods. If available, an optical cavity with a linewidth well below the modulation frequency can be used to measure the relative power between the carrier and the sidebands at $\pm\omega_m$ created by the modulation. If one wants to determine β in the 1MHz range, we would need a roughly 10cm long cavity with finesse over 10^4 , which is feasible experimentally but was not available at the time of this work. Instead, we followed a method similar to the one presented in [90]. Instead of a cavity, we need an acousto-optical modulator (AOM), which shifts the carrier frequency by usually tens of MHz. By interfering a phase modulated beam with a frequency shifted beam in the way shown in Figure F.1, the modulation depth can be extracted.

Let us go over the procedure, the laser beam is split into two paths, in one path, the phase modulator adds a sinusoidal phase to the beam such that the field after the modulator is:

$$E_p(t) \propto e^{-i\omega_1 t + i\beta \sin \omega t}. \quad (\text{F.4})$$

in the other path, an acousto-optical modulator shifts the carrier frequency by a certain amount ω_s :

$$E_s(t) \propto e^{-i(\omega_1 + \omega_s)t}. \quad (\text{F.5})$$

The paths are joined again at a beam-splitter, the ratio is such that the power received from each arm is P_p and P_s . The joint beam is measured at a photodetector, recording the power given by:

$$P_D(t) = |E_p(t) + E_s(t)|^2 = P_p^2 + P_s^2 + 2\sqrt{P_p P_s} \sum_{n=-\infty}^{\infty} J_n(\beta) \cos(\omega_s + n\omega_m)t, \quad (\text{F.6})$$

where we have used the Jacobi-Anger expansion [91, 92], which splits the modulation into an infinite sum of side-bands weighted by $J_n(\beta)$, which is the Bessel function of the first kind of order n . The output of the detector is sent to a spectrum analyzer, which measure the power spectral density (PSD) of $P_D(t)$. The spectrum will exhibit peaks at the side-bands $\omega_s + n\omega_m$ with peak-heights $S_{P_D P_D}(\omega_s + n\omega_m) = 4P_p P_s |J_n(\beta)|^2$. Assuming that the photodetector has the same frequency response at ω_s and $\omega_s \pm \omega_m$, we can extract β from the ratio of the peaks:

$$\frac{S_{P_D P_D}(\omega_s \pm \omega_m)}{S_{P_D P_D}(\omega_s)} = \frac{|J_1(\beta)|^2}{|J_0(\beta)|^2}. \quad (\text{F.7})$$

This procedure was followed in order to measure V_π at 1MHz of a Lithium Niobate fiber-coupled EOM (iXblue MPZ-LN-10). The 1550nm beam coming from our laser was split using a fiber splitter. At one output, the beam goes through the EOM, which was driven with sine-waves of various amplitudes (using a Keysight 33512b signal generator). In the other path, an AOM shifts the laser frequency by 40MHz (a G&H Fiber-Q AOM fed by a Windfreak Technologies SynthNV signal generator). After recombining in a second fiber splitter, the signal was measured with a fast photodiode (Thorlabs PDA05CF2, band-width 150MHz) and the PSD recorded in a spectrum analyzer (Siglent SSA3201X). V_π is extracted from a linear fit between modulation depth and amplitude (shown in Figure F.2). obtaining the following value:

$$V_\pi(1\text{MHz}) = 5.22 \pm 0.018\text{V} \quad (\text{F.8})$$

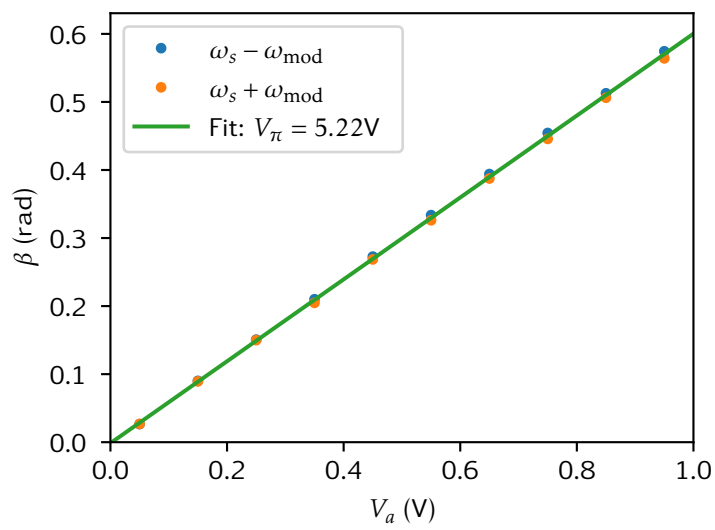


Figure F.2: In order to determine its V_π , the phase modulator is driven with sine-waves of different amplitudes V_a while recording the modulation depth β . A linear fit allows us to determine V_π by extrapolating the amplitude needed to obtain $\beta = \pi$.

Bibliography

- [1] R. P. Feynman. “Mathematical Formulation of the Quantum Theory of Electromagnetic Interaction”. In: *Physical Review* 80.3 (Nov. 1950). Publisher: American Physical Society, pp. 440–457. doi: 10.1103/PhysRev.80.440.
- [2] H. Fritzsch, M. Gell-Mann, and H. Leutwyler. “Advantages of the color octet gluon picture”. In: *Physics Letters B* 47.4 (Nov. 1973), pp. 365–368. ISSN: 0370-2693. doi: 10.1016/0370-2693(73)90625-4.
- [3] Sheldon L. Glashow. “Partial-symmetries of weak interactions”. In: *Nuclear Physics* 22.4 (Feb. 1961), pp. 579–588. ISSN: 0029-5582. doi: 10.1016/0029-5582(61)90469-2.
- [4] Steven Weinberg. “A Model of Leptons”. In: *Physical Review Letters* 19.21 (Nov. 1967). Publisher: American Physical Society, pp. 1264–1266. doi: 10.1103/PhysRevLett.19.1264.
- [5] J. M. Butterworth. “The Standard Model: how far can it go and how can we tell?” In: *Philosophical Transactions of the Royal Society A: Mathematical, Physical and Engineering Sciences* 374.2075 (Aug. 2016). Publisher: Royal Society, p. 20150260. doi: 10.1098/rsta.2015.0260.
- [6] Walther Gerlach and Otto Stern. “Der experimentelle Nachweis der Richtungsquantelung im Magnetfeld”. de. In: *Zeitschrift für Physik* 9.1 (Dec. 1922), pp. 349–352. ISSN: 0044-3328. doi: 10.1007/BF01326983.
- [7] Martin Bauer. *The Stern-Gerlach Experiment, Translation of: “Der experimentelle Nachweis der Richtungsquantelung im Magnetfeld”*. arXiv:2301.11343 [physics, physics:quant-ph]. Jan. 2023. doi: 10.48550/arXiv.2301.11343.
- [8] J. S. Bell. “On the Einstein Podolsky Rosen paradox”. In: *Physics Physique Fizika* 1.3 (Nov. 1964). Publisher: American Physical Society, pp. 195–200. doi: 10.1103/PhysicsPhysiqueFizika.1.195.
- [9] B. Hensen et al. “Loophole-free Bell inequality violation using electron spins separated by 1.3 kilometres”. en. In: *Nature* 526.7575 (Oct. 2015). Publisher: Nature Publishing Group, pp. 682–686. ISSN: 1476-4687. doi: 10.1038/nature15759.
- [10] A. D. O’Connell et al. “Quantum ground state and single-phonon control of a mechanical resonator”. en. In: *Nature* 464.7289 (Apr. 2010). Publisher: Nature Publishing Group, pp. 697–703. ISSN: 1476-4687. doi: 10.1038/nature08967.
- [11] Jasper Chan et al. “Laser cooling of a nanomechanical oscillator into its quantum ground state”. en. In: *Nature* 478.7367 (Oct. 2011). Publisher: Nature Publishing Group, pp. 89–92. ISSN: 1476-4687. doi: 10.1038/nature10461.

- [12] Herbert B. Callen and Theodore A. Welton. “Irreversibility and Generalized Noise”. In: *Physical Review* 83.1 (July 1951). Publisher: American Physical Society, pp. 34–40. doi: 10.1103/PhysRev.83.34.
- [13] Uroš Delić et al. “Cooling of a levitated nanoparticle to the motional quantum ground state”. In: *Science* 367.6480 (Feb. 2020). Publisher: American Association for the Advancement of Science, pp. 892–895. doi: 10.1126/science.aba3993.
- [14] Scott S. Verbridge et al. “High quality factor resonance at room temperature with nanostings under high tensile stress”. In: *Journal of Applied Physics* 99.12 (June 2006), p. 124304. issn: 0021-8979. doi: 10.1063/1.2204829.
- [15] Yeghishe Tsaturyan et al. “Demonstration of suppressed phonon tunneling losses in phononic bandgap shielded membrane resonators for high-Q optomechanics”. EN. In: *Optics Express* 22.6 (Mar. 2014). Publisher: Optica Publishing Group, pp. 6810–6821. issn: 1094-4087. doi: 10.1364/OE.22.006810.
- [16] Christoph Reinhardt et al. “Ultralow-Noise SiN Trampoline Resonators for Sensing and Optomechanics”. In: *Physical Review X* 6.2 (Apr. 2016). Publisher: American Physical Society, p. 021001. doi: 10.1103/PhysRevX.6.021001.
- [17] R. A. Norte, J. P. Moura, and S. Gröblacher. “Mechanical Resonators for Quantum Optomechanics Experiments at Room Temperature”. In: *Physical Review Letters* 116.14 (Apr. 2016). Publisher: American Physical Society, p. 147202. doi: 10.1103/PhysRevLett.116.147202.
- [18] Y. Tsaturyan et al. “Ultracoherent nanomechanical resonators via soft clamping and dissipation dilution”. en. In: *Nature Nanotechnology* 12.8 (Aug. 2017). Publisher: Nature Publishing Group, pp. 776–783. issn: 1748-3395. doi: 10.1038/nnano.2017.101.
- [19] Dennis Høj et al. “Ultra-coherent nanomechanical resonators based on inverse design”. en. In: *Nature Communications* 12.1 (Oct. 2021). Publisher: Nature Publishing Group, p. 5766. issn: 2041-1723. doi: 10.1038/s41467-021-26102-4.
- [20] Dennis Høj, Ulrich Busk Hoff, and Ulrik Lund Andersen. “Ultracoherent Nanomechanical Resonators Based on Density Phononic Crystal Engineering”. In: *Physical Review X* 14.1 (Mar. 2024). Publisher: American Physical Society, p. 011039. doi: 10.1103/PhysRevX.14.011039.
- [21] Andrea Cupertino et al. “Centimeter-scale nanomechanical resonators with low dissipation”. en. In: *Nature Communications* 15.1 (May 2024). Publisher: Nature Publishing Group, p. 4255. issn: 2041-1723. doi: 10.1038/s41467-024-48183-7.
- [22] A. A. Michelson and E. W. Morley. “On the relative motion of the Earth and the luminiferous ether”. en. In: *American Journal of Science* s3-34.203 (Nov. 1887). Publisher: American Journal of Science, pp. 333–345. doi: 10.2475/ajs.s3-34.203.333.
- [23] LIGO Scientific Collaboration and Virgo Collaboration et al. “Observation of Gravitational Waves from a Binary Black Hole Merger”. In: *Physical Review Letters* 116.6 (Feb. 2016). Publisher: American Physical Society, p. 061102. doi: 10.1103/PhysRevLett.116.061102.
- [24] A. A. Clerk et al. “Introduction to quantum noise, measurement, and amplification”. In: *Reviews of Modern Physics* 82.2 (Apr. 2010). Number: 2 Publisher: American Physical Society, pp. 1155–1208. doi: 10.1103/RevModPhys.82.1155.
- [25] Markus Aspelmeyer, Tobias J. Kippenberg, and Florian Marquardt. “Cavity optomechanics”. In: *Reviews of Modern Physics* 86.4 (Dec. 2014). Publisher: American Physical Society, pp. 1391–1452. doi: 10.1103/RevModPhys.86.1391.

- [26] Massimiliano Rossi et al. “Measurement-based quantum control of mechanical motion”. en. In: *Nature* 563.7729 (Nov. 2018). Number: 7729 Publisher: Nature Publishing Group, pp. 53–58. ISSN: 1476-4687. DOI: 10.1038/s41586-018-0643-8.
- [27] Guanhao Huang. “Room-Temperature Quantum Optomechanics and Free-Electron Quantum Optics”. eng. PhD thesis. Lausanne: EPFL, 2024. DOI: 10.5075/epfl-thesis-10206.
- [28] Yi Xia et al. *Motional sideband asymmetry of a solid-state mechanical resonator at room temperature*. arXiv:2408.06498 [quant-ph]. Aug. 2024. DOI: 10.48550/arXiv.2408.06498.
- [29] Masud Mansuripur. “Radiation pressure and the linear momentum of the electromagnetic field”. EN. In: *Optics Express* 12.22 (Nov. 2004). Number: 22 Publisher: Optica Publishing Group, pp. 5375–5401. ISSN: 1094-4087. DOI: 10.1364/OPEX.12.005375.
- [30] Stephen M. Barnett and Rodney Loudon. “The enigma of optical momentum in a medium”. In: *Philosophical Transactions of the Royal Society A: Mathematical, Physical and Engineering Sciences* 368.1914 (Mar. 2010). Publisher: Royal Society, pp. 927–939. DOI: 10.1098/rsta.2009.0207.
- [31] Jun John Sakurai and Jim Napolitano. *Modern quantum mechanics*. eng. 3rd ed. Cambridge: Cambridge University Press, 2021. ISBN: 978-1-108-47322-4.
- [32] Harvey Gould and Jan Tobochnik. *Statistical and thermal physics with computer applications*. eng. 2nd ed. Princeton: Princeton university press, 2021. ISBN: 978-0-691-20189-4.
- [33] Warwick P. Bowen and G. J. Milburn. *Quantum optomechanics*. OCLC: ocn934674781. Boca Raton, FL: CRC Press, Taylor & Francis Group, 2016. ISBN: 978-1-4822-5915-5 978-1-4822-5916-2.
- [34] H. Kogelnik and T. Li. “Laser Beams and Resonators”. EN. In: *Applied Optics* 5.10 (Oct. 1966). Publisher: Optica Publishing Group, pp. 1550–1567. ISSN: 2155-3165. DOI: 10.1364/AO.5.001550.
- [35] C. C Gerry and Peter Knight. *Introductory quantum optics*. English. OCLC: 1105538922. Cambridge, UK; New York: Cambridge University Press, 2005. ISBN: 978-0-511-22695-3 978-0-511-22865-0 978-0-511-22949-7 978-0-511-64837-3 978-0-511-79123-9.
- [36] D.F. Walls and Gerard J. Milburn. “Input–Output Formulation of Optical Cavities”. en. In: *Quantum Optics*. Ed. by D.F. Walls and Gerard J. Milburn. Berlin, Heidelberg: Springer, 2008, pp. 127–141. ISBN: 978-3-540-28574-8. DOI: 10.1007/978-3-540-28574-8_7.
- [37] Feng Zhou et al. “Cavity Optomechanical Bistability with an Ultrahigh Reflectivity Photonic Crystal Membrane”. en. In: *Laser & Photonics Reviews* 17.10 (2023), p. 2300008. ISSN: 1863-8899. DOI: 10.1002/lpor.202300008.
- [38] Georg Enzian et al. “Phononically shielded photonic-crystal mirror membranes for cavity quantum optomechanics”. EN. In: *Optics Express* 31.8 (Apr. 2023). Number: 8 Publisher: Optica Publishing Group, pp. 13040–13052. ISSN: 1094-4087. DOI: 10.1364/OE.484369.
- [39] A. R. Agrawal et al. “Focusing membrane metamirrors for integrated cavity optomechanics”. EN. In: *Optica* 11.9 (Sept. 2024). Publisher: Optica Publishing Group, pp. 1235–1241. ISSN: 2334-2536. DOI: 10.1364/OPTICA.522509.
- [40] J. D. Thompson et al. “Strong dispersive coupling of a high-finesse cavity to a micromechanical membrane”. en. In: *Nature* 452.7183 (Mar. 2008). Publisher: Nature Publishing Group, pp. 72–75. ISSN: 1476-4687. DOI: 10.1038/nature06715.
- [41] A. M. Jayich et al. “Dispersive optomechanics: a membrane inside a cavity”. en. In: *New Journal of Physics* 10.9 (Sept. 2008). Publisher: IOP Publishing, p. 095008. ISSN: 1367-2630. DOI: 10.1088/1367-2630/10/9/095008.

- [42] Dalziel Joseph Wilson. “Cavity Optomechanics with High Stress Silicon Nitride Films”. en. phd. California Institute of Technology, June 2012. doi: 10.7907/VB3C-1G76.
- [43] Christian M. Pluchar, Aman R. Agrawal, and Dalziel J. Wilson. “Thermal intermodulation backaction in a high-cooperativity optomechanical system”. EN. In: *Optica* 10.11 (Nov. 2023). Publisher: Optica Publishing Group, pp. 1543–1550. issn: 2334-2536. doi: 10.1364/OPTICA.500123.
- [44] Aaron Meurer et al. “SymPy: symbolic computing in Python”. en. In: *PeerJ Computer Science* 3 (Jan. 2017). Publisher: PeerJ Inc., e103. issn: 2376-5992. doi: 10.7717/peerj-cs.103.
- [45] H. Yuen and J. Shapiro. “Optical communication with two-photon coherent states–Part III: Quantum measurements realizable with photoemissive detectors”. In: *IEEE Transactions on Information Theory* 26.1 (Jan. 1980). Conference Name: IEEE Transactions on Information Theory, pp. 78–92. issn: 1557-9654. doi: 10.1109/TIT.1980.1056132.
- [46] H. J. Carmichael. “Spectrum of squeezing and photocurrent shot noise: a normally ordered treatment”. EN. In: *JOSA B* 4.10 (Oct. 1987). Publisher: Optica Publishing Group, pp. 1588–1603. issn: 1520-8540. doi: 10.1364/JOSAB.4.001588.
- [47] Hans-Albert Bachor and Timothy C. Ralph. *A guide to experiments in quantum optics*. eng. Third edition. Weinheim: Wiley-VCH, 2019. isbn: 978-3-527-69580-5 978-3-527-41193-1.
- [48] Massimiliano Rossi. “Quantum Measurement and Control of a Mechanical Resonator”. PhD thesis. University of Copenhagen, 2020.
- [49] Jens Arnbak Holbøll Nielsen. *Generation and Application of Squeezed States of Light in Quantum Sensing*. Department of Physics, Technical University of Denmark, 2021.
- [50] Vincent Dumont et al. “High-power quantum-limited 35 MHz photodiode and classical laser noise suppression”. In: *Review of Scientific Instruments* 94.12 (Dec. 2023), p. 123101. issn: 0034-6748. doi: 10.1063/5.0170826.
- [51] Michał Parniak et al. “High-frequency broadband laser phase noise cancellation using a delay line”. EN. In: *Optics Express* 29.5 (Mar. 2021). Publisher: Optica Publishing Group, pp. 6935–6946. issn: 1094-4087. doi: 10.1364/OE.415942.
- [52] Sampo A. Saarinen et al. “Laser cooling a membrane-in-the-middle system close to the quantum ground state from room temperature”. EN. In: *Optica* 10.3 (Mar. 2023). Publisher: Optica Publishing Group, pp. 364–372. issn: 2334-2536. doi: 10.1364/OPTICA.468590.
- [53] D. Hunger et al. “A fiber Fabry–Perot cavity with high finesse”. en. In: *New Journal of Physics* 12.6 (June 2010). Publisher: IOP Publishing, p. 065038. issn: 1367-2630. doi: 10.1088/1367-2630/12/6/065038.
- [54] N. E. Flowers-Jacobs et al. “Fiber-cavity-based optomechanical device”. In: *Applied Physics Letters* 101.22 (Nov. 2012). Publisher: American Institute of Physics, p. 221109. issn: 0003-6951. doi: 10.1063/1.4768779.
- [55] Felix Rochau et al. “Dynamical Backaction in an Ultrahigh-Finesse Fiber-Based Microcavity”. In: *Physical Review Applied* 16.1 (July 2021). Publisher: American Physical Society, p. 014013. doi: 10.1103/PhysRevApplied.16.014013.
- [56] H. Pfeifer et al. “Achievements and perspectives of optical fiber Fabry–Perot cavities”. en. In: *Applied Physics B* 128.2 (Jan. 2022), p. 29. issn: 1432-0649. doi: 10.1007/s00340-022-07752-8.

- [57] J. D. Thompson et al. “Strong dispersive coupling of a high-finesse cavity to a micromechanical membrane”. en. In: *Nature* 452.7183 (Mar. 2008). Publisher: Nature Publishing Group, pp. 72–75. issn: 1476-4687. doi: 10.1038/nature06715.
- [58] Dennis Høj. *Development of ultra-high quality mechanical oscillators*. Department of Physics, Technical University of Denmark, 2021.
- [59] Silvan Schmid, Luis Guillermo Villanueva, and Michael Lee Roukes. *Fundamentals of Nanomechanical Resonators*. en. Cham: Springer International Publishing, 2016. isbn: 978-3-319-28689-1 978-3-319-28691-4. doi: 10.1007/978-3-319-28691-4.
- [60] B. D. Hauer et al. “A general procedure for thermomechanical calibration of nano/micromechanical resonators”. In: *Annals of Physics* 339 (Dec. 2013), pp. 181–207. issn: 0003-4916. doi: 10.1016/j.aop.2013.08.003.
- [61] D. J. Wilson et al. “Measurement-based control of a mechanical oscillator at its thermal decoherence rate”. en. In: *Nature* 524.7565 (Aug. 2015). Number: 7565 Publisher: Nature Publishing Group, pp. 325–329. issn: 1476-4687. doi: 10.1038/nature14672.
- [62] P.-L. Yu et al. “A phononic bandgap shield for high-Q membrane microresonators”. en. In: *Applied Physics Letters* 104.2 (Jan. 2014). Number: 2 Publisher: American Institute of PhysicsAIP, p. 023510. issn: 0003-6951. doi: 10.1063/1.4862031.
- [63] Pauli Virtanen et al. “SciPy 1.0: fundamental algorithms for scientific computing in Python”. en. In: *Nature Methods* 17.3 (Mar. 2020). Publisher: Nature Publishing Group, pp. 261–272. issn: 1548-7105. doi: 10.1038/s41592-019-0686-2.
- [64] Leonhard Neuhaus et al. *FPGA-based feedback control of quantum optics experiments with the open source software package PyRPL*. arXiv:2310.00086 [physics, physics:quant-ph]. Sept. 2023. doi: 10.48550/arXiv.2310.00086.
- [65] Benjamin Petrak et al. “Feedback-controlled laser fabrication of micromirror substrates”. In: *Review of Scientific Instruments* 82.12 (Dec. 2011). Number: 12 Publisher: American Institute of Physics, p. 123112. issn: 0034-6748. doi: 10.1063/1.3671291.
- [66] D. Hunger et al. “Laser micro-fabrication of concave, low-roughness features in silica”. In: *AIP Advances* 2.1 (Jan. 2012), p. 012119. issn: 2158-3226. doi: 10.1063/1.3679721.
- [67] Thibaud Ruelle, Martino Poggio, and Floris Braakman. “Optimized single-shot laser ablation of concave mirror templates on optical fibers”. EN. In: *Applied Optics* 58.14 (May 2019). Number: 14 Publisher: Optica Publishing Group, pp. 3784–3789. issn: 2155-3165. doi: 10.1364/AO.58.003784.
- [68] Miguel Arevallilo Herráez et al. “Fast two-dimensional phase-unwrapping algorithm based on sorting by reliability following a noncontinuous path”. EN. In: *Applied Optics* 41.35 (Dec. 2002). Publisher: Optica Publishing Group, pp. 7437–7444. issn: 2155-3165. doi: 10.1364/AO.41.007437.
- [69] Jan M. Binder et al. “Qudi: A modular python suite for experiment control and data processing”. English. In: *SoftwareX* 6 (Jan. 2017). Publisher: Elsevier, pp. 85–90. issn: 2352-7110. doi: 10.1016/j.softx.2017.02.001.
- [70] W. Winkler et al. “Birefringence-induced losses in interferometers”. In: *Optics Communications* 112.5 (Dec. 1994), pp. 245–252. issn: 0030-4018. doi: 10.1016/0030-4018(94)90626-2.
- [71] David Jacob et al. “Supermirror phase anisotropy measurement”. EN. In: *Optics Letters* 20.7 (Apr. 1995). Publisher: Optica Publishing Group, pp. 671–673. issn: 1539-4794. doi: 10.1364/OL.20.000671.

- [72] Jordan B. Camp et al. “Measurement of birefringence of low-loss, high-reflectance coating of m-axis sapphire”. EN. In: *Applied Optics* 40.22 (Aug. 2001). Publisher: Optica Publishing Group, pp. 3753–3758. ISSN: 2155-3165. DOI: 10.1364/AO.40.003753.
- [73] M. L. Gorodetsky et al. “Determination of the vacuum optomechanical coupling rate using frequency noise calibration”. EN. In: *Optics Express* 18.22 (Oct. 2010). Publisher: Optica Publishing Group, pp. 23236–23246. ISSN: 1094-4087. DOI: 10.1364/OE.18.023236.
- [74] T.-C. Zhang et al. “Quantum noise of free-running and externally-stabilized laser diodes”. en. In: *Quantum and Semiclassical Optics: Journal of the European Optical Society Part B* 7.4 (Aug. 1995), p. 601. ISSN: 1355-5111. DOI: 10.1088/1355-5111/7/4/015.
- [75] T. J. Kippenberg, A. Schliesser, and M. L. Gorodetsky. “Phase noise measurement of external cavity diode lasers and implications for optomechanical sideband cooling of GHz mechanical modes”. en. In: *New Journal of Physics* 15.1 (Jan. 2013). Publisher: IOP Publishing, p. 015019. ISSN: 1367-2630. DOI: 10.1088/1367-2630/15/1/015019.
- [76] A. Kaushik, H. Kahn, and A.H. Heuer. “Wafer-level mechanical characterization of silicon nitride MEMS”. In: *Journal of Microelectromechanical Systems* 14.2 (Apr. 2005). Conference Name: Journal of Microelectromechanical Systems, pp. 359–367. ISSN: 1941-0158. DOI: 10.1109/JMEMS.2004.839315.
- [77] Florian Marquardt, J. G. E. Harris, and S. M. Girvin. “Dynamical Multistability Induced by Radiation Pressure in High-Finesse Micromechanical Optical Cavities”. In: *Physical Review Letters* 96.10 (Mar. 2006). Publisher: American Physical Society, p. 103901. DOI: 10.1103/PhysRevLett.96.103901.
- [78] Guanhao Huang et al. “Room-temperature quantum optomechanics using an ultralow noise cavity”. en. In: *Nature* 626.7999 (Feb. 2024). Publisher: Nature Publishing Group, pp. 512–516. ISSN: 1476-4687. DOI: 10.1038/s41586-023-06997-3.
- [79] Constanze Metzger et al. “Self-Induced Oscillations in an Optomechanical System Driven by Bolometric Backaction”. In: *Physical Review Letters* 101.13 (Sept. 2008). Publisher: American Physical Society, p. 133903. DOI: 10.1103/PhysRevLett.101.133903.
- [80] Sergey A. Fedorov et al. “Thermal intermodulation noise in cavity-based measurements”. EN. In: *Optica* 7.11 (Nov. 2020). Publisher: Optica Publishing Group, pp. 1609–1616. ISSN: 2334-2536. DOI: 10.1364/OPTICA.402449.
- [81] Katharina Möhle. “Piezoelectrically tunable optical cavities for the gravitational wave detector LISA”. eng. Accepted: 2017-06-18T12:21:10Z. doctoralThesis. Humboldt-Universität zu Berlin, Mathematisch-Naturwissenschaftliche Fakultät I, May 2013. DOI: 10.18452/16745.
- [82] Nathan T. Arnold et al. “Free-space photonic quantum memory”. In: *Quantum Computing, Communication, and Simulation III*. Vol. 12446. SPIE, Mar. 2023, pp. 25–30. DOI: 10.1117/12.2649350.
- [83] Simon Bernard et al. “Monitored wet-etch removal of individual dielectric layers from high-finesse Bragg mirrors”. EN. In: *Optics Express* 28.23 (Nov. 2020). Publisher: Optica Publishing Group, pp. 33823–33829. ISSN: 1094-4087. DOI: 10.1364/OE.400986.
- [84] Jinglei Zhang and Klaus Mølmer. “Prediction and retrodiction with continuously monitored Gaussian states”. In: *Physical Review A* 96.6 (Dec. 2017). Publisher: American Physical Society, p. 062131. DOI: 10.1103/PhysRevA.96.062131.
- [85] Massimiliano Rossi et al. “Observing and Verifying the Quantum Trajectory of a Mechanical Resonator”. In: *Physical Review Letters* 123.16 (Oct. 2019). Publisher: American Physical Society, p. 163601. DOI: 10.1103/PhysRevLett.123.163601.

- [86] Chao Meng et al. “Measurement-based preparation of multimode mechanical states”. In: *Science Advances* 8.21 (May 2022). Publisher: American Association for the Advancement of Science, eabm7585. doi: 10.1126/sciadv.abm7585.
- [87] Maryse Ernzer et al. “Optical Coherent Feedback Control of a Mechanical Oscillator”. In: *Physical Review X* 13.2 (May 2023). Publisher: American Physical Society, p. 021023. doi: 10.1103/PhysRevX.13.021023.
- [88] Amir H. Safavi-Naeini et al. “Squeezed light from a silicon micromechanical resonator”. en. In: *Nature* 500.7461 (Aug. 2013). Publisher: Nature Publishing Group, pp. 185–189. issn: 1476-4687. doi: 10.1038/nature12307.
- [89] Alessandro S. Villar. “The conversion of phase to amplitude fluctuations of a light beam by an optical cavity”. In: *American Journal of Physics* 76.10 (Oct. 2008), pp. 922–929. issn: 0002-9505. doi: 10.1119/1.2937903.
- [90] Shangjian Zhang et al. “Self-calibrating measurement of high-speed electro-optic phase modulators based on two-tone modulation”. EN. In: *Optics Letters* 39.12 (June 2014). Publisher: Optica Publishing Group, pp. 3504–3507. issn: 1539-4794. doi: 10.1364/OL.39.003504.
- [91] Murray R. Spiegel, Seymour Lipschutz, and John Liu. *Fórmulas y tablas de matemática aplicada*. spa. 4^a ed. OCLC: 892528616. Madrid: McGraw-Hill, Interamericana de España, 2014. isbn: 978-607-15-1145-4.
- [92] Eric W. Weisstein. *Jacobi-Anger Expansion*. en. Text. Publisher: Wolfram Research, Inc.

... we do these things not because they are easy,
but because *we thought* they were going to be easy.
ANONYMOUS